BULGARIAN CHEMICAL COMMUNICATIONS

Optimization of europium transport through a supported liquid membrane containing Cyanex 272 using response surface methodology

P. Zaheri[*], F. Zahakifar, M. Gh. Maragheh

Nuclear Fuel Cycle Research School, Nuclear Science and Technology Research Institute, AEOI, P.O. Box: 11365-8486, Tehran-Iran

In this study, the transport of europium (Eu^{3+}) was investigated using bis (2,4,4-trimethylpentyl) phosphinic acid (Cyanex 272) extractant in a supported liquid membrane (SLM) system. The effect of various parameters such as feed phase pH, extractant concentration, and stripping phase concentration was investigated with response surface methodology (RSM). At the optimum conditions, membrane permeability of 2.35×10^{-5} m s^{-1} was obtained. The results demonstrated that the transfer kinetics follow a first-order model. Examination of SLM stability showed that the membrane used was stable for six runs, and permeability did not change significantly. The permeability and stability of the membrane decreased with the increment of the membrane pore size. Examination of the separation of dysprosium (Dy^{3+}) and Eu^{3+} with the Taguchi method showed that feed pH has the most significant effect on the separation factor.

Keywords: Europium; Supported liquid membrane; Permeability; Response surface methodology; Cyanex 272, Separation.

INTRODUCTION

In the last few decades, the applications of rare earth elements have increased, and the demand for them has widely grown. There are numerous applications of these elements in the nuclear, metallurgical, chemical, catalytic, electrical, and magnetic industries. Europium, Eu^{3+}, is a rare earth element that is used to create blue and red light in TVs and computer monitors due to its unique optical properties. Other applications include wireless internet systems, optical fibers, X-ray imaging, fluorescent lamps, and LEDs [1, 2].

Various methods have been used to purify and separate rare earth elements, such as fractional crystallization [3], ion exchange [4], and solvent extraction [5-7]. In recent years, liquid membrane (LM) separation technology has been used as an alternative to conventional solvent extraction methods. This technology has been considered by many researchers due to lower investment and operating costs, lower energy consumption, economical use of expensive extractants, and high selectivity [8, 9].

Mass transfer in the liquid membrane is affected by the shape and structure of the liquid membrane. The liquid membrane is divided into phase dispersion (emulsion liquid membrane) and non-phase dispersion (bulk liquid membrane and supported liquid membrane) methods [10]. A supported liquid membrane is a result of impregnating a porous solid base with a liquid membrane that contains diluent and extractant. The consumption of extractant in the method of supported liquid membranes is lower than that of emulsion membranes and bulk liquid membranes. Among the various types of supported liquid membranes, the use of flat-sheet supported liquid membrane is one of the simplest ways to evaluate the performance of the liquid membrane method [11].

On one side of the membrane, the reaction between the solute ions and the extractant molecules leads to the formation of a solute-extractant complex. This reaction is reversed on the other side of the membrane, and the solute ions enter the stripping phase. The extractant molecules stay inside the membrane to repeat this cycle [12].

So far, many researchers have used the liquid membrane method to extract rare earth elements. However, this process has not yet reached the industrial stage and still needs to optimize the parameters to improve the efficiency and stability of the system.

Gaikwad scrutinized synergetic transport of europium through a contained supported liquid membrane using trioctylamine and tributyl phosphate as carriers [13]. In another work, the transport of Eu^{3+} through an SLM was investigated using octyl(phenyl)-N,N-diisobutylcarbamoyl-methylphosphine oxide (CMPO) as an extractant. The maximum extraction of Eu^{3+} was achieved by the combination of 0.2 mol L^{-1} CMPO with 5% iso-decanol/n-dodecane at feed acid concentration of

* To whom all correspondence should be sent:
E-mail: pzaheri@aeoi.org.ir

3–4 mol L^{-1} HNO$_3$ [14]. Lee *et al.* studied the influence of effective parameters on the permeation of Eu^{3+} using an SLM system containing 2-ethylhexyl phosphonic acid mono-2-ethylhexyl ester (PC-88A) [2]. Liang *et al.* separated the Eu^{3+} up to 95.3% using a dispersion combined liquid membrane (DCLM) in the presence of 2-ethyl hexyl phosphonic acid-mono-2-ethyl hexyl ester (P507) [15]. Eu^{3+} pertraction trend also in the SLM system was determined by N,N,N′,N′-tetra-2-ethylhexyl diglycolamide (T2EHDGA) as the extractant. Under optimum conditions, the membrane diffusion coefficient was 4.25×10^{-6} cm^2.s [16].

In this study, for the first time the influence of various parameters on Eu^{3+} transport through a supported liquid membrane (SLM) containing Cyanex 272 was investigated based on design expert statistical analysis software as a new method. The aim of the research was to establish whether the correlations predicted by the software have sufficient accuracy in predicting the Eu^{3+} transport *via* a SLM. In case of acceptable accuracy, it is possible to save costs related to the consumption of raw materials by conducting fewer tests using this method.

MATERIALS AND METHODS

Materials

To prepare the organic phase, Cyanex 272 (bis (2,4,4-trimethylpentyl) phosphinic acid) as an extractant and kerosene as a diluent were used. The hydrophobic polytetrafluoroethylene (PTFE) membranes used in the present study were procured from Millipore (Billerica, MA, USA). The PTFE membrane was placed inside the organic phase, and a supported liquid membrane (SLM) was prepared.

The feed solution was prepared by dissolving Eu(NO$_3$)$_3$.6H$_2$O and (Dy(NO$_3$)$_3$.6H$_2$O in distilled water. The pH of the solutions was adjusted using HNO$_3$ or NaOH. The stripping phase solutions were prepared by dissolving a certain amount of nitric acid in distilled water. All materials except the PTFE membrane were purchased from Merck (Darmstadt, Germany). All chemicals used were of analytical grade and used without purification.

Apparatuses

The pH of the aqueous solutions was measured using a Sartorius pH meter. The interfacial tension of the phases was measured by the device model Krüss GmbH. The viscosity was measured using an ubbelohde viscometer.

The membrane system consists of two chambers of feed and stripping phases with the same volume of 200 mL. The Plexiglas chambers have no direct contact with each other and exchange ions with each other only through the membrane. Ion concentrations in the aqueous phase were measured using a UV–Visible spectrophotometer (model Cary 100, Varian, Palo Alto, CA, USA).

To determine the concentration of ions in the aqueous solutions with a UV-Vis device, the procedure provided by Marczenko was used [17]. First, standard solutions were prepared and then the concentration of the desired samples was determined based on the values of the prepared standards.

Experimental procedure

For experiments, the prepared membrane was placed in the membrane system. The speed of the stirrers in the feed and stripping phases was set at 500 rpm. The feed and stripping solutions were sampled at regular intervals. The following equation was used to calculate the experimental permeability coefficient (P) in the membrane [18]:

$$P \frac{A}{V_f} t = \ln \left(\frac{[M^{3+}]_f}{[M^{3+}]_{f,0}} \right) \tag{1}$$

where $[M^{3+}]_{f,0}$ and $[M^{3+}]_f$ are the concentrations of Eu^{3+} ions in the feed at t = 0 and t = t, respectively. A and V$_f$ are the effective membrane area and the feed phase volume, respectively. The value of P under different experimental conditions can be calculated by plotting $\ln([M^{3+}]_f / [M^{3+}]_{f,0})$ *versus* t. By the values of P and drawing the changes of 1/P with $[H^+]^3$ at a constant concentration of the extractant, the permeability coefficient in the membrane and the mass transfer coefficient at the feed-membrane surface was determined using the following equation [18].

$$\frac{1}{P} = \frac{1}{K_f} + \frac{d_m}{D_{m,c}} \frac{\zeta [H^+]^3}{\varepsilon K_e [HR]^3} \tag{2}$$

The parameters K$_f$, D$_{m, c}$, d$_m$, K$_e$, ε, and ζ are the mass transfer coefficient in the feed phase (m/s), the complex penetration coefficient in the membrane (m/s), the membrane thickness (m), the reaction equilibrium constant (unitless), the membrane porosity, and membrane tortuosity, respectively [19]. In a previous study, the K$_e$ of europium was determined to be 7.58×10^{-5} [19]. The following equation was used to calculate the percentage of metal transfer through the membrane:

$$Extraction\% = \left(\frac{[M^{3+}]_{f0} - [M^{3+}]_f}{[M^{3+}]_{f0}} \right) \times 100 \tag{3}$$

Experimental design

The experiments of Eu transport *via* the SLM are designed utilizing RSM based on the central composite design (CCD) with design expert software. A 2^3 CCD with 3 independent variables (feed phase pH, extractant concentration, and stripping phase concentration) was investigated at five different levels (-α,-1, 0, +1, +α) containing 20 experiments [20].

Analysis of variance (ANOVA) was used to analyze the data obtained from the design of experiment and the degree of impact of the main variables, interaction between factors, standard deviation coefficients, etc. Analysis of variance, or ANOVA, is a statistical method that separates observed variance data into different components to use for additional tests [21, 22]. The significance of the coefficients of the model is determined using the F and P-values. P-values less than 0.05 for each factor indicate that it is statistically significant [23].

Mechanism of reaction

In low-polarity organic solvents, organophosphorus extractants are present in the form of a dimer $(HA)_2$. Therefore, the extraction reaction can be considered as follows [1]:

$$Eu^{3+} + 3(HA)_{2,org} \overset{k_e}{\leftrightarrow} Eu(HA_2)_{3,org} + 3H^+_{aq} \qquad (4)$$
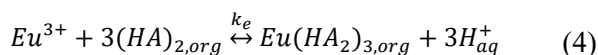
In this mechanism, Eu^{3+} ions are transferred from the feed phase to the recovery (stripping) phase, and the protons move in the opposite direction. The driving force for this transfer mechanism is the concentration gradient of protons. Therefore, ions pass from the feed phase to the recovery phase in the opposite direction of their concentration gradient. This condition occurs when the concentration of protons in the recovery phase is much higher than in the feed phase.

RESULTS AND DISCUSSION

Study of interfacial tension of organic and aqueous phases

Fig. 1 shows the interfacial tension of distilled water and of the organic phase of the membrane as a function of the concentration of Cyanex 272 extractant in the kerosene. The results show that the surface tension decreases on increasing the extractant concentration in the organic phase. Therefore, the extractants show surface activity in kerosene. A decrease in interfacial tension is observed in three areas: a gentle slope at low extractant concentrations (region 1), then an almost sharp slope at reduced interfacial tension (region 2),

and finally, nearly zero slope at high extractant concentrations (region 3). The decrease in interfacial tension is due to the adsorption of the extractant molecules. The Gibbs relation expresses it [24]:

$$\Gamma = -\frac{d\gamma}{RT\,dlna} \qquad (5)$$

where Γ, γ, a, and R are the surface accumulation density (mol m^{-2}), interfacial tension (N m^{-1}), the surface activity of the adsorbed components in the organic phase (mol L^{-1}), and the universal gas constant (J K^{-1} mol^{-1}), respectively.
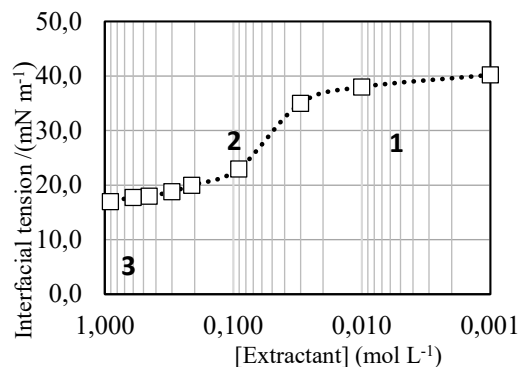
Fig. 1. Interfacial tension of organic phase and aqueous phase at different concentrations of the extractant

Fig. 2 shows the changes in the interfacial tension of the organic and aqueous phases as a function of the Eu^{3+} concentration in the aqueous phase. When the liquid membrane phase is in contact with an aqueous solution (containing metal ions), the interfacial tension changes due to the formation of complex molecules on the surface. Since the formed complexes have different surface activities, at a low concentration of extractant (0.03 mol L^{-1}), the interfacial tension increases with the increasing concentration of europium ions.
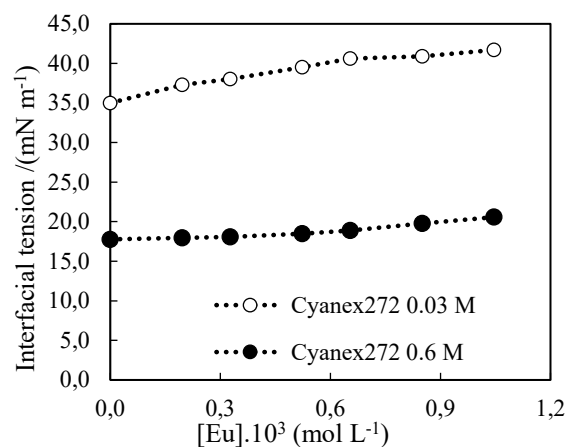
Fig. 2. Interfacial tension of organic phase and aqueous phase with different concentrations of Eu^{3+}

In other words, the formed complexes have lower surface activity than free extractant molecules due to their low tendency to form hydrogen bonds with water molecules.

As a result, the concentration of complexes formed on the surface increases with increasing the concentration of Eu^{3+} ions. So, interfacial tension also increases. This increase continues until all the extractant molecules on the surface form complexes with Eu^{3+} ions. At high concentrations of the extractant (0.6 mol L^{-1}), the increase in interfacial tension with increasing concentrations of metal ions is negligible.

Study of parameters affecting Eu^{3+} transfer with RSM

The effect of feed phase pH, extractant concentration and stripping phase concentration was investigated using RSM. The results are presented in Table 1. The permeability of Eu^{3+} was the response of the experiments. Experiments 5, 9, 13, 14, 18, and 19 have the same test condition, which indicates the appropriate repeatability of the experiments. The proposed model also provides the predicted results.

Analysis of variance. Analysis of variance (ANOVA) was used to analyze the data and determine the effect of the main parameters, the interaction between them, and the standard deviation coefficients. The results showed that the quadratic model is the best model for fitting the data obtained from the experiments. The results of ANOVA for the proposed regression model are reported in Table 2. Values of P less than 0.05 for each expression indicate that it is statistically significant.

Table 1. The levels of effective parameters and the results of membrane permeability tests for Eu^{3+} transfer using RSM.

Run	Feed phase pH	Extractant concentration (mol L^{-1})	Stripping phase concentration (mol L^{-1})	Eu^{3+} permeability $\times 10^5$ (m s^{-1}) (Experimental)	Eu^{3+} permeability $\times 10^5$ (m s^{-1}) (Model predicted)
1	3.25	0.10	1.75	0.33	0.33
2	1.61	0.26	2.49	0.40	0.39
3	1.61	0.74	2.49	0.77	0.86
4	0.50	0.50	1.75	0.70	0.71
5	3.25	0.50	1.75	1.14	1.16
6	3.25	0.50	3.00	0.98	1.01
7	1.61	0.74	1.01	1.20	1.02
8	4.89	0.26	1.01	1.32	1.26
9	3.25	0.50	1.75	1.27	1.16
10	3.25	0.50	0.50	1.02	1.32
11	4.89	0.74	2.49	1.67	1.53
12	3.25	0.90	1.75	0.88	0.94
13	3.25	0.50	1.75	1.17	1.16
14	3.25	0.50	1.75	1.16	1.16
15	6.00	0.50	1.75	2.18	2.28
16	1.61	0.26	1.01	0.48	0.48
17	4.89	0.26	2.49	1.07	1.07
18	3.25	0.50	1.75	1.25	1.16
19	3.25	0.50	1.75	1.19	1.16
20	4.89	0.74	1.01	1.88	1.77

Table 2. Results of ANOVA for Eu^{3+} transfer data

Source	Sum of squares	df	Mean square	F value	p-value
Model	0.35	6	0.058	68.35	<0.0001
pH (A)	0.17	1	0.17	203.69	<0.0001
Ex. Con. (B)	0.85	1	0.085	100.80	<0.0001
Str. Con. (C)	0.0089	1	0.0089	10.57	0.063
AB	0.0037	1	0.0037	4.42	0.0555
A²	0.0039	1	0.0039	4.72	0.0490
B²	0.069	1	0.069	81.61	<0.0001
Residual	0.01	13	0.0008		

The quadratic model for Eu^{3+} transfer *via* SLM containing Cyanex 272 is as follows:

$$P \times 10^5 = \begin{pmatrix} 0.387 + 0.056pH + 1.727Ex - \\ 0.034\,Str - 0.055pH * Ex + 0.0062pH^2 \\ -1.215\,Ex^2 \end{pmatrix}^{0.33} \quad (6)$$

The F-value for the model is equal to 31.83, which indicates the model validity. The coefficient of determination (R-squared) and the adjusted R-squared were 0.98 and 0.96, respectively. Therefore, the experimental data and the model predictions are very well matched. A comparison of experimental data with the statistical model provided by the software is presented in Fig. 3. It can be observed that the predicted values are very close to the experimental values.
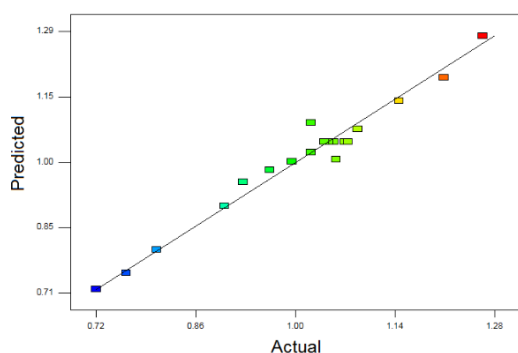
Fig. 3. Comparison of experimental data with the statistical model

The graph of the residuals *versus* the experimental data is shown in Fig. S1. It is observed that the resulting chart has a random trend and does not follow a specific pattern. Therefore, there are no latent variables and no systematic errors.

Study of the effect of parameters with RSM

The influence of effective parameters on Eu^{3+} transfer is shown in Figs. 4(a) to (c). As Eu^{3+} ions move from the feed to the stripping phase, the protons move in the opposite direction. The concentration gradient of protons is the driving force for the transfer of Eu^{3+} ions. Therefore, the acidity of the feed phase affects the transfer. The impact of feed phase pH in the range of 0.5 to 6 on the Eu^{3+} transfer was investigated. The results showed that by increasing the pH of the feed phase to 5, the penetration of Eu^{3+} increases. With the increment of pH of the feed phase, the rate of complex formation at the boundary of the feed phase and liquid membrane phase increases. As a result, a higher concentration gradient of the complex increases the penetration of Eu^{3+} *via* the membrane [25].

At lower pH values, the concentration of H^+ ions at the membrane boundary is higher than that of Eu^{3+} ions. As a result, competition with metal ions occurs at the interface of the feed and liquid membrane phase. Therefore, the transfer of metal ions is reduced [26].
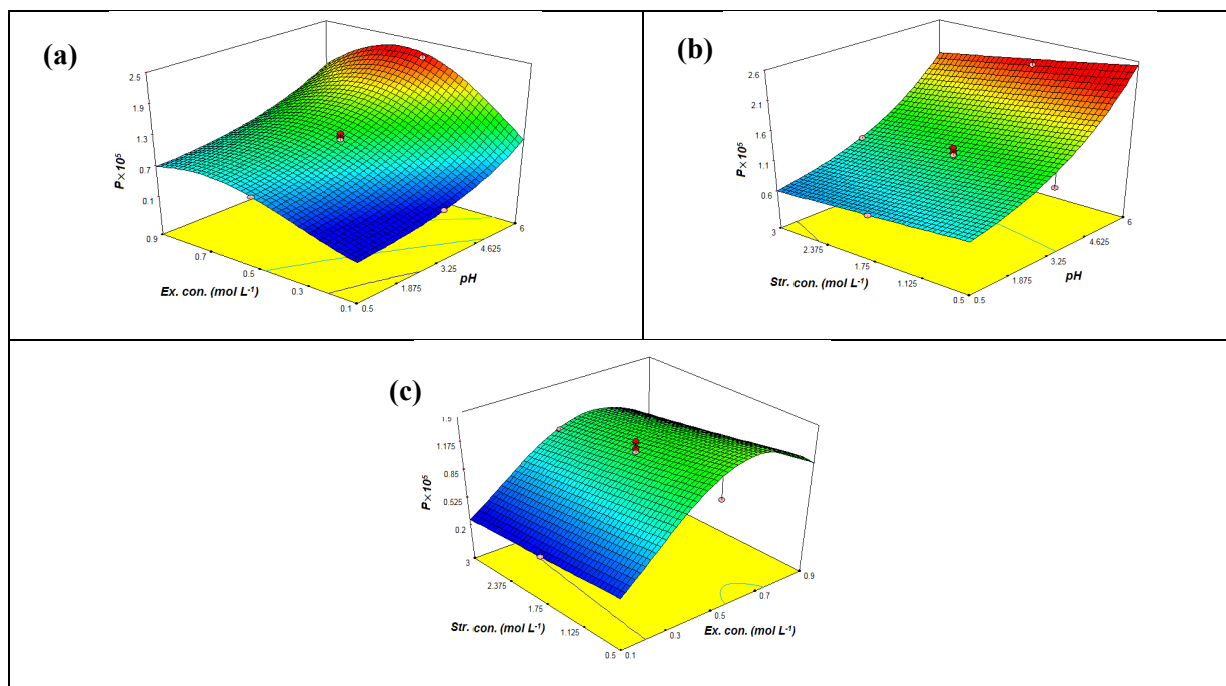
Fig. 4. Influence of effective parameters on membrane permeability for Eu^{3+} transfer. a) feed phase pH and extractant concentration; b) feed phase pH and stripping phase concentration; and c) stripping phase concentration and extractant concentration

The effect of stripping phase concentration (0.5-3 mol L^{-1}) was also investigated. According to Eq. 2, the driving force for the transfer of Eu^{3+} increases with increasing HNO$_3$ concentration in the stripping phase. As a result, the permeability of the membrane increases. The membrane permeability slightly decreases with an increase in the HNO$_3$ concentration to 3 mol L^{-1}. In this case, the concentration of protons at the interface between the liquid membrane and the stripping phase increases. Some extractant molecules react with the protons at the interface between the liquid membrane and the stripping phase. As a result, the membrane permeability is reduced [21]. Increasing the acid concentration in the stripping phase reduces the interfacial tension between the liquid membrane phase and the aqueous phase and favors the dissolution of the extractant in the aqueous phase [22]. Also, the high contact time between the acidic aqueous solution and the membrane phase causes gradual degradation of the latter.

In investigating the effect of extractant concentration on Eu^{3+} penetration, the maximum value obtained in these diagrams can be explained by the change in the viscosity of the liquid membrane. In the first part of the diagram, the higher concentration of the extractant increases the Eu^{3+}-extractant complex concentration. So, the membrane permeability increases. On the other hand, the viscosity of the liquid membrane phase increases with the extractant concentration increment, which lowers the penetration of complexes *via* the liquid membrane [10]. Changes in the viscosity of the liquid membrane are shown in Fig. 5. According to experimental data, there is an exponential relationship between viscosity and extractant concentration, which is expressed as follows:

$$\mu = \alpha \exp(\beta C) \qquad (7)$$

The constant values of α and β are 1.4943 and 0.7702, respectively. The diffusion coefficient of the complex in the liquid membrane with increasing extractant concentration was calculated by Eq. 2 and is reported in Table 3. As can be observed, the diffusion coefficient decreases with increasing extractant concentration.
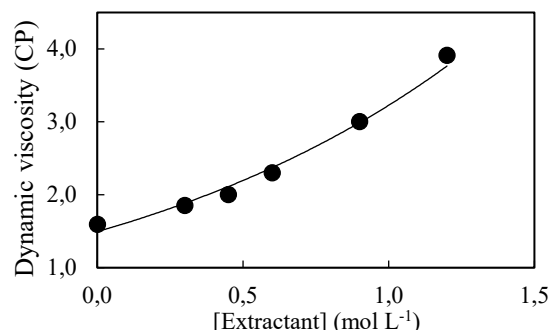
Fig. 5. Influence of extractant concentration on the liquid membrane viscosity.

Table 3. Influence of extractant concentration on the diffusion coefficient of the complexes in the liquid membrane.

$D_{m,c}$ (m^2 s^{-1})	Cyanex272 concentration (mol L^{-1})
1.51×10^{-9}	0.1
7.33×10^{-10}	0.3
3.05×10^{-10}	0.6
5.42×10^{-10}	0.9

Validation of the proposed model. ANOVA showed that the model is well consistent with the data. For model validation, the experimental conditions of the parameters were randomly selected, and the experiment was performed. Then the obtained results were compared with the values predicted by the model. The error values in Table 4 show that the model has well predicted the experimental results.

The design-expert software predicts that at pH=6, [HNO$_3$] = 0.1 mol L^{-1}, and [Cyanex 272] = 0.57 mol L^{-1}, maximum permeability (2.47×10^{-5} m s^{-1}) can be expected. Under optimum conditions, experimental permeability was obtained at 2.35×10^{-5} m s^{-1}.

Table 4. Validation of the Eu^{3+} transfer model using random experiments.

Run	Feed phase pH	Extractant concentration (mol L^{-1})	Stripping phase concentration (mol L^{-1})	Predicted Eu^{3+} permeability ×10^5 (m s^{-1})	Experimental Eu^{3+} permeability ×10^5 (m s^{-1})	Error (%)
1	0.8	0.25	1	0.38	0.35	8.10
2	1.5	0.8	2	0.85	0.90	4.17
3	2.7	0.5	0.8	1.14	1.09	5.10
4	3.5	0.7	2.5	1.18	1.26	5.98
5	4.7	0.4	1.5	1.50	1.53	2.11
Optimum point	6	0.57	1	2.47	2.35	5.38

Study of the effect of membrane pore size

To study the effect of membrane pore size on permeability, PTFE supports with pore sizes of 0.22, 0.45, 1, and 5 μm, porosity of 85%, and uniform thickness (150 μm) were examined. The results in Fig. 6 show that the permeability and stability of the membrane decreased with the increment of membrane pore size. This trend indicates that larger pores have lower ability to hold the liquid membrane [27].
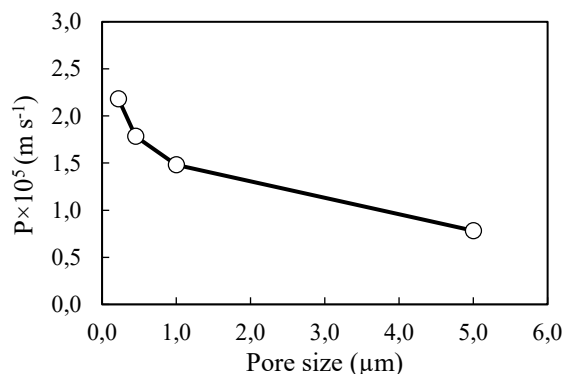
Fig. 6. Effect of the membrane pore size on the permeability ([Eu]=0.61×10^{-3} mol L^{-1}, [Cyanex 272]=0.6 mol L^{-1}, pH=6).

Therefore, on increasing the size of the pores, the exit of the liquid membrane from the pores of the support becomes faster and causes instability.

Reaction kinetics

The highest permeability occurs at the extractant concentration of 0.57 mol L^{-1}, stripping concentration of 1 mol L^{-1}, and pH=6. The concentration-time diagram under these conditions ([Eu]=0.61×10^{-3} mol L^{-1}), is shown in Fig. 7. The results showed that the increasing trend in the stripping phase is approximately equal to the decrement trend in the feed phase. Therefore, the accumulation of Eu^{3+} ions in the li*quid membrane phase is negligible.

Fig. 8 shows the changes in ln (C/C$_0$) *versus* time. As observed, there is a linear relationship between them. Therefore, the transfer of Eu^{3+} ions *via* the SLM using the Cyanex 272 extractant has first-order kinetics.
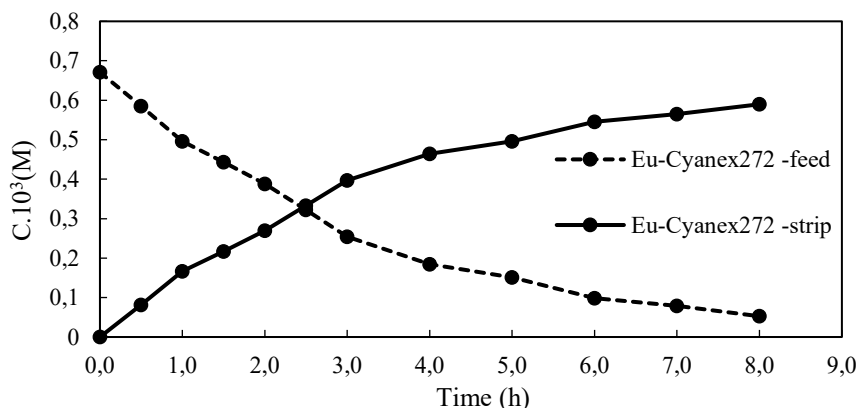
Fig. 7. Changes in Eu^{3+} concentration *versus* time under optimal conditions.

$$y = 0.317x - 0.031$$
$$R^2 = 0.99$$
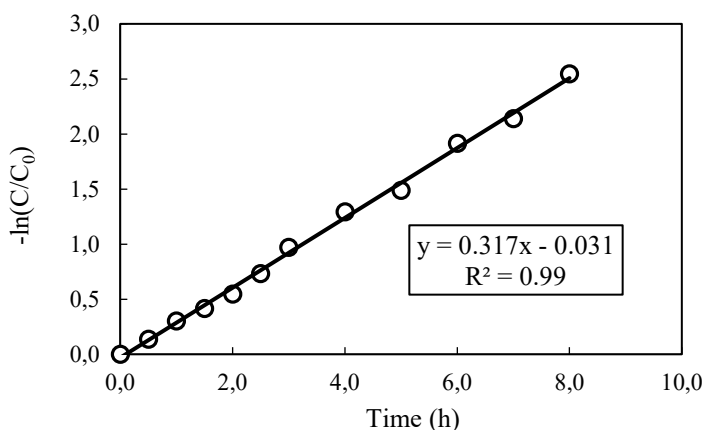
Fig. 8. Kinetics of Eu^{3+} transfer under optimal conditions.
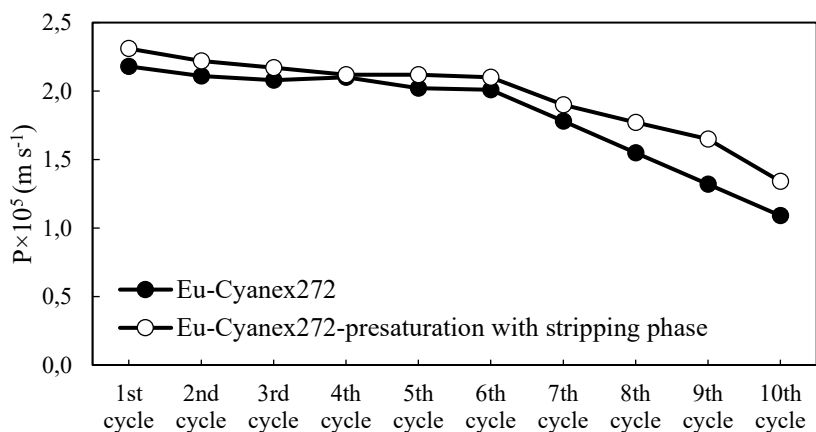
Fig. 9. SLM stability and effect of saturation of the liquid membrane and stripping phases on it.

Table 5. Previous studies on the extraction of Eu^{3+} using liquid membranes.

Extractant	Diluent	Stripping agent	Method	Extraction %	Stability	Ref.
D2EHPA	Kerosene	HNO_3	SDLM	94.2%	N/A	[30]
T2EHDGA	n-Dodecane	HNO_3	SLM	95.0%	20 days	[31]
PC-88A	Kerosene	HCl	SLM	N/A	N/A	[2]
P507	Kerosene	HCl	DCLM	95.3%	N/A	[15]
TOA + TBP	Kerosene	N/A	CSLM	N/A	50 h	[13]
D2EHPA+Cyanex 272	Kerosene	HNO_3	SLM	96.0%	9 days	[12]
Cyanex 272	Kerosene	HNO_3	SLM	92.3%	6 days	This work

Evaluation of SLM stability

For evaluating the stability of the used SLM, ten consecutive experiments were done with one support. The experiment duration was 4 h, and after each run, feed and stripping phase solutions were replaced with fresh ones. The results are shown in Fig. 9. After six runs, the permeability did not decrease significantly.

The solubility of the organic and aqueous phases (especially that of the stripping phase) is one of the main causes of SLM instability [28]. The organic and stripping phases were saturated before use in the SLM to study this effect. The results showed that saturation improves the stability of the membrane.

After five days and a reduction of membrane permeability, to compensate for the lost liquid membrane phase, the polymer support of the membrane was again immersed in the organic phase for 24 h and reused. The results showed that the membrane permeability is 1.75 $m^2 s^{-1}$, and its value is less than in the first cycle. Zang *et al.* stated that the reason for this decrement was the increase in the pore size due to its continuous use [29]. A summary of previous studies for the extraction of Eu^{3+} using liquid membranes and their stability is presented in Table 5. A comparison of the results shows that the presence of Cyanex 272 in the LM provides stability and Eu^{3+} extraction in the range of reported studies.

Separation of Dy and Eu^{3+} by Taguchi method

Dysprosium is an element that is commonly found with europium. Due to the similar chemical properties of Dy and Eu, the separation of these elements is significant [32, 33]. In this section of the experiments, the separation of dysprosium and europium was investigated. Taguchi method was used to study the effect of different parameters on the separation factor (SF). Optimization of the separation factor was performed using Qualitek-4 software. The studied factors included the ratio of metal ions concentrations in the feed phase, extractant concentration in the membrane phase, feed phase pH, and stripping phase concentration. To minimize the error of the experimental results, the experiments were repeated, and the mean separation factor (SF) was calculated. The separation factor of dysprosium and europium was calculated from the following equation:

$$SF(Dy/Eu) = \frac{([Dy]/[Eu])_{strip}}{([Dy]/[Eu])_{feed,t=0}} \qquad (8)$$

Table 6. Parameters, levels and separation factors (SF) of Dy and Eu

Run	pHf (A)	[HNO$_3$] (B)	[Cyanex272] (C)	[Dy]/[Eu] (D)	SF (Dy/Eu) (Y)
1	0.5	0.5	0.3	0.5	2.57
2	0.5	1	0.45	1	2.80
3	0.5	2	0.6	2	1.61
4	2	0.5	0.45	2	1.88
5	2	1	0.6	0.5	1.09
6	2	2	0.3	1	1.21
7	4	0.5	0.6	1	1.40
8	4	1	0.3	2	1.29
9	4	2	0.45	0.5	1.04
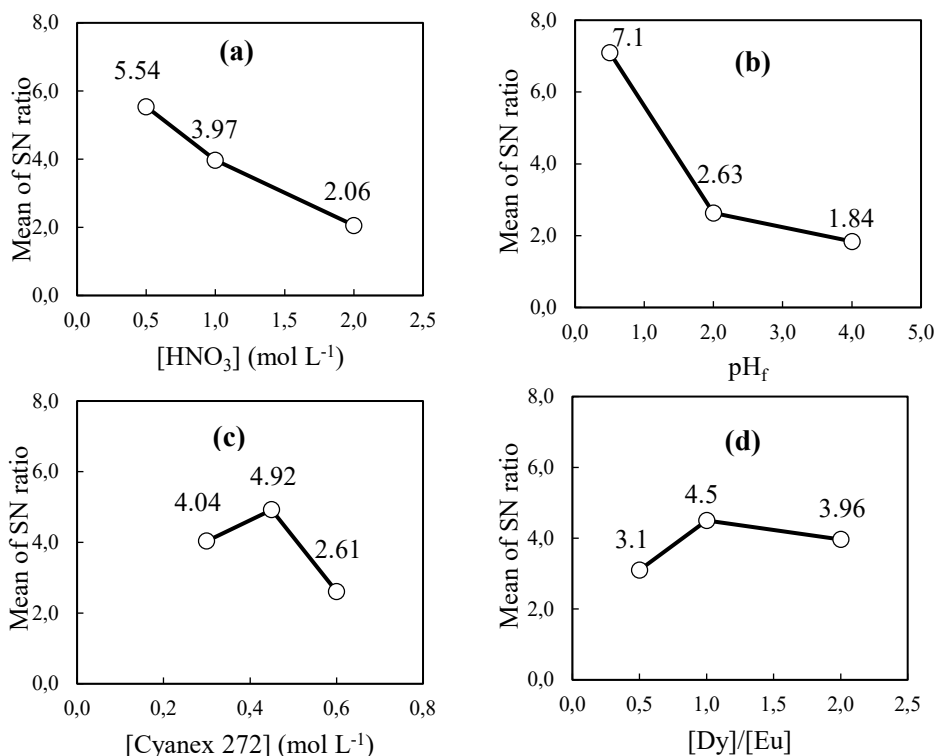
Fig. 10. Effect of a) stripping phase concentration; b) feed phase pH; c) extractant concentration in the membrane phase and d) ratio of metal ions concentrations in feed on the SF of Dy and Eu

The parameters, levels, and SFs of Dy and Eu^{3+} are presented in Table 6. The tool that the Taguchi design method uses to analyze the results is the signal/noise (SN) ratio. Fig. 10 shows the changes in the SN ratio at different levels of factors affecting the SF. In Fig. 10, higher SN values indicate a more significant SF. The results predict that at pH=0.5, [HNO$_3$]=0.5 M, [Cyanex 272] = 0.45 mol L^{-1} and Dy/Eu=1, a maximum separation factor (3.02) can be expected. Under these conditions, a validation test was repeated, and SF=2.73 was obtained. Analysis of variance (ANOVA) showed that the most important factor influencing the SF of Dy and Eu^{3+} is the pH of the feed phase. On the other hand, based on the hard and soft acid-base (HSAB) theory [34], the low pH of the solution favors the nature of the

Cyanex 272 molecules, and therefore the Dy ions have a stronger tendency to interact with them.

CONCLUSIONS

In this paper, a SLM system was used for the transport of Eu^{3+} using Cyanex 272 extractant. The effect of parameters such as feed phase pH, extractant concentration, and stripping phase concentration were studied with RSM. A quadratic model was proposed that was in good agreement with the experimental data. The results showed that the feed phase pH and Cyanex 272 concentration were the effective parameters in the Eu^{3+} transfer through the SLM. The kinetic studies also verified the first-order model for transferring of Eu^{3+} ions.

Membrane permeability of 2.35×10^{-5} m s^{-1} was obtained with 0.57 mol L^{-1} Cyanex 272, pH = 6, and

stripping phase concentration of 1 mol L^{-1}. At these optimum conditions, the membrane was suitably stable for six runs. However, the stability and hence, the permeability of the membrane decreased with the increment of membrane pore size.

The maximum separation factor (SF = 2.73) of Dy^{3+} and Eu^{3+} was obtained at pH = 0.5, [HNO$_3$] = 0.5 mol L^{-1}, [Cyanex 272] = 0.45 mol L^{-1}, and Dy^{3+}/Eu^{3+} = 1.

REFERENCES

1. N. Krishnamurthy, C. K. Gupta, Extractive metallurgy of rare earths. CRC press, 2015.
2. C.-J. Lee, B.-R. Yang, *The Chemical Engineering Journal and The Biochemical Engineering Journal,* **57** (3), 253 (1995).
3. S. Wu *et al.*, *Chemical Engineering Journal,* **335**, 774 (2018).
4. G. Saipriya, R. Kumaresan, P. K. Nayak, K. A. Venkatesan, M. P. Antony, T. Kumar, *Journal of Radioanalytical and Nuclear Chemistry,* **314** (3), 2557 (2017).
5. R. Banda, F. Forte, B. Onghena, K. Binnemans, *RSC Advances,* **9 (**9), 4876 (2019).
6. B. B. Mishra, N. Devi, *Journal of Molecular Liquids,* 271, 89 (2018).
7. P. Ren *et al.*, *Inorganic Chemistry,* **59** (19), 14218 (2020).
8. F. Zahakifar, A. Charkhi, M. Torab-Mostaedi, R. Davarkhah, *Radiochimica Acta,* **106** (3), 181 (2018).
9. F. Zahakifar, A. Charkhi, M. Torab-Mostaedi, R. Davarkhah, *Journal of Radioanalytical and Nuclear Chemistry,* **316** (1), 247 (2018).
10. V. S. Kislik, Liquid membranes: principles and applications in chemical separations and wastewater treatment. Elsevier, 2009.
11. P. Zaheri, T. Mohammadi, H. Abolghasemi, M. Ghannadi Maraghe, *Chemical Engineering Research and Design,* **100**, 81 (2015).
12. P. Zaheri, H. Abolghasemi, M. G. Maraghe, T. Mohammadi, *Chemical Engineering and Processing: Process Intensification,* **92**, 18 (2015).
13. A. G. Gaikwad, *Talanta,* **63 (**4), 917 (2004).
14. R. Kumar, S. A. Ansari, P. Kandwal, P. K. Mohapatra, *Chemical Engineering Research and Design,* **168**, 307 (2021).
15. P. Liang, W. Liming, F. Xinglong, *Chinese Journal of Chemical Engineering,* **19** (1), 33 (2011).
16. S. Panja, P. K. Mohapatra, S. K. Misra, S. C. Tripathi, *Separation Science and Technology,* **46** (12), 1941 (2011).
17. Z. Marczenko, M. Balcerzak, Separation, preconcentration and spectrophotometry in inorganic analysis, Elsevier, 2000.
18. P. Zaheri, H. Abolghasemi, T. Mohammadi, M. G. Maraghe, *Chemical Papers,* **69** (2), 279 (2015).
19. P. Zaheri, H. Ghassabzadeh, H. Abolghasemi, M. G. Maraghe, T. Mohammadi, *The Canadian Journal of Chemical Engineering,* **95** (3), 524 (2017).
20. F. Zahakifar, A. Keshtkar, E. Z. Souderjani, M. Moosavian, *Progress in Nuclear Energy,* **124**, 103335 (2020).
21. M. R. A. Shadbad, P. Zaheri, H. Abolghasemi, F. Zahakifar, *Chemical Engineering and Processing-Process Intensification,* 109268 (2023).
22. F. Zahakifar, A. Charkhi, M. Torab-Mostaedi, R. Davarkhah, A. Yadollahi, *Journal of Radioanalytical and Nuclear Chemistry,* 1 (2018).
23. H. Arabi, S. Milani, H. Abolghasemi, F. Zahakifar, *Journal of Radioanalytical and Nuclear Chemistry,* **327**, 653 (2021).
24. J. Zhao, X. Sun, W. Li, S. Meng, D. Li, *Journal of Colloid and Interface Science,* **294** (2), 429 (2006).
25. M. Hasan, R. Aglan, S. El-Reefy, *Journal of Hazardous Materials,* **166** (2-3), 1076 (2009).
26. K. Chitra, A. Gaikwad, G. Surender, A. Damodaran, *Journal of Membrane Science,* **125** (2), 257 (1997).
27. X. Yang, A. Fane, *Journal of Membrane Science,* **156** (2), 251 (1999).
28. M. C. Wijers, M. Jin , M.Wessling, H. Strathmann, *Journal of Membrane Science*, 147(1), 117 (1996).
29. H.-D. Zheng, B.-Y. Wang, Y.-X. Wu, Q.-L. Ren, *Colloids and Surfaces A: Physicochemical and Engineering Aspects,* **351** (1-3), 38 (2009).
30. P. Liang, W. Liming, Y. Guoqiang, *Journal of Rare Earths,* **29** (1), 7 (2011).
31. S. Panja, P. Mohapatra, S. Misra, S. Tripathi, *Separation Science and Technology,* **46** (12), 1941 (2011).
32. P. Zaheri, H. Abolghasemi, T. Mohammadi, M. G. Maraghe, *Korean Journal of Chemical Engineering,* **32** (8), 642 (2015).
33. M. Mallah, F. Shemirani, M. Ghannadi Maragheh, *Journal of Radioanalytical and Nuclear Chemistry,* **278** (1), 97 (2008).
34. J. E. Huheey, E. A. Keiter, R. L. Keiter, O. K. Medhi, Inorganic chemistry: principles of structure and reactivity. Pearson Education India, 2006.

Synthesis, characterization and application of undoped TiO$_2$ and co-doped TiO$_2$ (with Ba & Co) for the photocatalytic degradation of Coomassive brilliant blue (CBB) dye under UV light irradiation

F. Akbar Jan[1]*, Sh. Khalid[1], N. Ullah[2], R. Ullah[1]

[1]Department of Chemistry, Bacha Khan University Chrasadda, Khyber-Pakhtunkhwa, 24420 Pakistan
[2]Department of Chemistry, Qauid-i-Azam University Islamabad, 45320 Pakistan

Titanium oxide (TiO$_2$) and Ba and Co co-doped TiO$_2$ nanoparticles were synthesized through a sol-gel method. The synthesized nanoparticles were characterized using X-ray diffraction (XRD), Fourier transform infrared spectroscopy (FTIR), UV-visible spectroscopy (UV-Vis), and scanning electron microscopy (SEM). Using X-ray diffraction analysis different parameters were calculated, such as crystallite size, d-spacing, dislocation density, number of unit cells, cell volume, morphological index, microstrain and instrumental broadening. The average particle size of both titanium oxide (TiO$_2$) and Ba and Co co-doped TiO$_2$ nanoparticles was calculated to be 15.98 nm and 24.69 nm, respectively. Scanning electron microscopy revealed that TiO$_2$ has rough spherical morphology with small particles agglomeration while Ba and Co co-doped TiO$_2$ nanoparticles consist of slightly larger blocks of agglomerated particles with irregular morphology. Doping of TiO$_2$ with Ba and Co decreased the band gap from 3.10 eV to 2.92 eV. The characterized particles were used as a photocatalyst for the degradation of Coomassive brilliant blue dye in aqueous solution under UV light. The effect of different parameters, e. g. irradiation time, initial dye concentration, pH of the medium and catalyst dosage on the percent degradation was also studied. The dye degradation linearly increased with an increase in irradiation time. About 93% and 77% dye degradation was observed at 240 min duration using undoped and Co-Ba-doped TiO$_2$, respectively. The degradation of the dye was found to decrease with an increase in initial dye concentration. On increasing the amount of Co-Ba-doped TiO$_2$ catalyst the rate of degradation increased while using bare TiO$_2$ the percent degradation decreased with increase in catalyst dose up to 0.05 g. At low pH higher degradation was found as compared to higher pH. Co and Ba co-doped TiO$_2$ powders exhibited high photocatalytic activity towards discoloration of Coomassive brilliant blue dye.

Keywords: Titanium oxide (TiO$_2$), Ba and Co co-doped TiO$_2$, nanoparticles, Coomassive brilliant blue dye, UV light

INTRODUCTION

Modern textile and dyeing industries have led to the direct or indirect dumping of more and more toxic substances to air and water thereby threatening environment and humanity [1]. There is a dire need for the removal of dyes from local and industrial water effluents with cost-effective technologies in compliance with growing environmental rules and regulations. Coomassive brilliant blue dye belongs to the group of non-azo dyes and is used as an acid wool dye. It is also used as a reagent for staining proteins in electrophoresis techniques and for measuring protein [2]. Coagulation by chemical agents and resins, activated carbon, electro catalytic decomposition, ultrafiltration and biological treatment are wastewater treatment technologies currently in use [3]. The dyes are resistant to biological, as well as physical treatment technologies[4]. The other methods have their own demerits but advanced oxidation processes (AOP) which are used for the photodegradation of toxic compounds have gained the attention of scientists in recent years [5]. Semiconductor material-based photocatalysts have been extensively used in the fields of solar energy conversion, cleaning and sterilization, sewage treatment and air purification. Production of no secondary pollutants, mild reaction conditions, high efficiency and high stability and complete mineralization of pollutants are among the merits of the photocatalytic oxidation process over the other techniques. Constructing an efficient photocatalyst with visible light response and conducting an in-depth study of its mechanism is required now-a-days to boost the efficiency of the waste water purification process [6]. Both homogenous and heterogeneous catalysis are used for the degradation of various families of hazardous materials [7]. Photocatalytic degradation using a nanocatalyst has been employed as a preferred effective method for the demineralization of organic pollutants. Nanomaterials have unique properties, i.e., large surface area, ease of preparation and wide energy gaps which can be altered by doping with other metals. A number of compounds including

---

ZnO, SnO$_2$ and ZnO$_3$ are used for photocatalytic degradation. Titanium dioxide is one of the important candidates for nanomaterials. It is relatively safe, nontoxic, and cheap, it is also used as a whitening ingredient in toothpastes. It is used in photochemistry ranging from large-scale products to more advanced applications including dye-sensitized solar cells, photoelectrolysis of water and environmental remediation[8, 9]. Owing to its large band gap (3–3.2eV) the efficiency of TiO$_2$ is limited to the UV range [10]. In order to improve degradation and recovery efficiency, both metal and non-metal oxides are doped and co-doped with it. Doping causes shifting of both the conduction band (CB) and valence band (VB) of TiO$_2$ to more negative values resulting in the formation of $\cdot O^{2-}$ which significantly enhances photodegradation. Photodegradation efficiency is also affected by carrier separation, and transfer reduction potential [11]. As the conduction band of TiO$_2$ is higher in energy than the Fermi level of the noble metal, thus photo promoted electrons can efficiently migrate to the metal, leaving holes in the TiO$_2$ valence band [12]. Studies have reported the degradation of toluene and methylene blue under visible light using Zr, S and B, Zr co-doped TiO$_2$ [13]. Co-doping of TiO$_2$ using Ba, Zr and Co has drawn the attention because these dopants not only increase the surface area but also thermally stabilize the TiO$_2$ which retards the combination of electrons and holes. Less dense anatase phase TiO$_2$ formation is facilitated by Ba^{2+} due to its more electropositive nature and hence high photocatalytic activity. The effect of elements with large ionic radii: Ba^{2+}(1.3 Å), Zr^{3+} (0.79 Å) and Zr^{4+} (0.68 Å) has also been studied while using them for the photocatalytic degradation of the pollutant dye Rhodamine B [14]. Keeping in view the advantages of co-doping a study was designed to synthesize and characterize undoped TiO$_2$ and Ba &Co co-doped TiO$_2$. Application of bareTiO$_2$ and co-doped TiO$_2$ NPs for the photocatalytic degradation of Coomassive brilliant blue dye in aqueous medium was among the objectives of the study.

EXPERIMENTAL

Synthesis of TiO₂ and doped TiO₂ nanoparticles (NPs)

TiO$_2$ nanoparticles were synthesized through sol gel technique. Figure 1 represents the schematic diagram for the synthesis of TiO$_2$ nanoparticles. First 4.21 ml of titanium (IV) iso-propoxide was added to 12 ml of iso-propanol and the mixture was stirred for 5 min using a magnetic stirrer. Thus, we got an alkoxide solution. A mixture of one ml water and five ml iso-propanol was prepared and added drop wise to the alkoxide solution. The mixture was then stirred for 24 h at ambient temperature. Upon completion of the reaction the precipitate was dried at 100 $^{\circ}$C in an oven. It was finally calcined at 500 $^{\circ}$C and 1000 $^{\circ}$C in a furnace. The above-mentioned sol-gel technique was also applied for the synthesis of Ba and Co co-doped TiO$_2$NPs with addition of 3% (1.5% of each dopant) of barium chloride and cobalt chloride hexahydrate salts to the TTIP solution before the hydrolysis step.

Characterization techniques

The synthesized nanoparticles were characterized using X-ray diffraction (XRD), scanning electron microscopy (SEM), energy dispersive X-ray (EDX), UV-Vis spectrophotometry and FTIR spectroscopy.
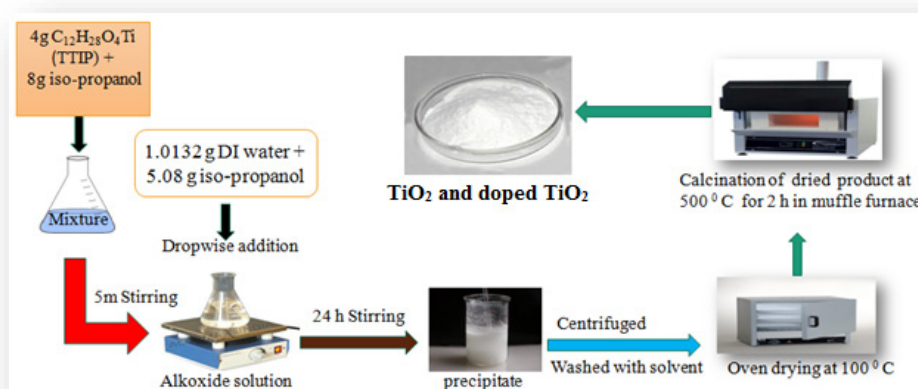
Fig. 1. Schematic diagram of the sol-gel method for the synthesis of TiO$_2$ and doped TiO$_2$NPs.

Preparation of the dye solution

The stock solution (500 ppm) of Coomassive brilliant blue dye (CBB) was prepared by dissolving 0.125 g of dry powder of dye in distilled water and vigorously shaking. Then working solutions of different concentrations were prepared from the stock solution. The working solutions were prepared using the dilution formula given in equation (1):

$$M_1V_1 = M_2V_2 \tag{1}$$

Photocatalytic degradation of dye

The photocatalytic activity of TiO₂ NPs and barium and cobalt co-doped TiO₂ NPs was evaluated in the degradation of the organic dye Coomassive brilliant blue in aqueous solution. For comparison the photocatalytic degradation of the dye was carried out under UV light and sun light. The maximum absorption of Coomassive brilliant blue dye was found at 556 nm and was used as a monitor wavelength for photodegradation. An appropriate amount (0.01 to 0.05 g) of photocatalyst was separately added to the working solutions. The mixed solution was stirred for 30 min in the dark to establish desorption/desorption equilibrium before the photodegradation reaction. Then the dispersion was kept in a light source. In the experiments an UV-lamp was placed 15 cm above the surface of the solution in a locally designed equipment. The dye degradation was checked at various intervals of time, and the catalyst was removed by centrifugation. The same process was repeated in sun light. The absorbance of the centrifuged solution was measured by UV-Vis spectrometry. The percent photodegradation of Coomassive brilliant blue dye was calculated using the following relation given in equation (2):

$$D(\%) = \frac{C_0 - C_t}{C_0} \times 100 \tag{2}$$

where C_0 and C_t denote the concentrations of Coomassive brilliant blue dye at time 0 min and t(s), respectively, and t is the irradiation time.

RESULTS AND DISCUSSION

XRD study

Figure 2 shows the XRD spectrum of the synthesized materials.

$$D = \frac{K\lambda}{\beta \cos\Theta} \tag{3}$$

where D is the crystallite size, K is the Scherrer constant having a value of 0.9, λ is the diffraction wavelength of light, β shows the full width at half maximum of sharp peaks and Θ is the angle of reflection.

The average crystallite sizes of undoped and doped TiO₂ are 15.98 nm and 24.69 nm, respectively.
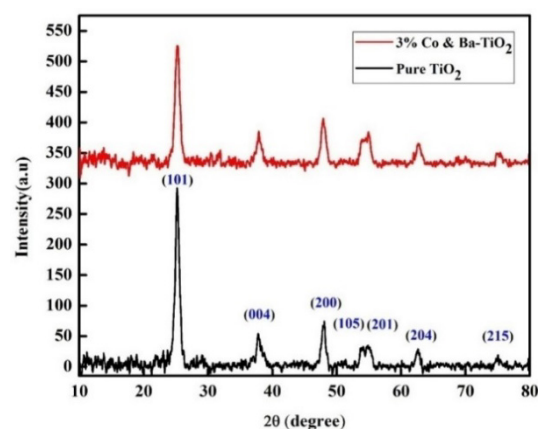
Fig. 2. XRD pattern of (a) TiO₂ and (b) Ba and Co co-doped TiO₂ nanoparticles.

XRD d-spacing

d-Spacing was calculated using Bragg's law; the d-spacing is the interplanar spacing between the two atoms shown in equation (4):

$$2 \, d \sin\Theta = n\lambda \tag{4}$$

where λ is the wavelength of X-rays; its value is 1.5406 Å for CuKα [15]. The values of d-spacing for 2Θ positions at 25.16°, 37.84°, 48.09°, 53.91°, 55.06°, 62.70° and 75.07° for TiO₂ and for doped TiO₂ are 25.30°, 38.00°, 48.10°, 55.03°, 62.6°3 and 75.21° as shown in Tables 1 and 2.

XRD dislocation density

Dislocation is the irregularity or crystallographic imperfection within the crystal structure or a deviation from a perfect crystal structure. Material science well explains the numerous properties influenced by the presence of dislocation within the crystal. The movement of one dislocation hinders the other dislocations present in the crystal structure. Also, the bigger the dislocation the larger will be the hardness of sample [16]. The formula for calculation of dislocation density is shown in equation (5):

$$\delta = \frac{1}{D^2} \tag{5}$$

where δ represents the dislocation density and D is the crystallite size of the nanoparticles. The values of the dislocation density for TiO₂ and doped TiO₂ are shown in Tables 1 and 2.

Table 1. Diffraction angle, FWHM (β), particle size (D), d-spacing, dislocation density, number of unit cells and morphology index of TiO₂ nanoparticles.

Diffraction Angle (2θ in degree)	FWHMβ) (Radians)	Particle Size (D) (nm)	d-Spacing (Å)	Dislocation Density (m^{-2})×10^{-3}	Number of Unit Cells ×10^{-3}	Morphological Index (Unitless)
25.30	0.0068	20.44	2.80	2.40	33.91	0.59
38.00	0.0061	47.93	2.43	0.43	437.20	0.61
48.10	0.0050	31.59	1.91	1.00	125.18	0.64
55.03	0.0061	31.59	1.60	1.01	125.18	0.61
62.63	0.0064	21.71	1.45	2.23	40.63	0.60
75.21	0.0099	14.04	1.20	5.02	10.98	0.50

Table 2. Diffraction angle, FWHM (β), particle size (D), d-spacing, dislocation density, number of unit cells and morphology index of co-doped TiO₂ nanoparticles.

Diffraction Angle (2θ in degree)	FWHM(β) (Radians)	Particle Size (D) (nm)	d-Spacing (Å)	Dislocation Density (m^{-2})×10^{-3}	Number of Unit Cells ×10^{-3}	Morphological Index (Unitless)
25.16	0.0121	11.84	3.53	7.10	6.53	0.62
37.84	0.0054	27.80	2.37	1.23	85.31	0.78
48.09	0.0082	18.78	1.89	2.83	26.30	0.70
53.91	0.0082	19.30	1.70	2.60	27.27	0.70
55.06	0.010	14.32	1.66	4.81	11.66	0.64
62.70	0.016	10.69	1.48	8.72	4.63	0.55
75.07	0.020	8.68	1.26	13.20	2.50	0.50

The number of unit cells of the crystal system was calculated using the formula given in equation (6):

$$n = \pi \left(\frac{4}{3}\right) \times \left(\frac{D}{2}\right)^{3} \times (1/V) \quad (6)$$

There is an inverse relation of the number of unit cells with the dislocation density as shown by the equation ($n = \frac{(constant)}{\delta^{\frac{3}{2}}}$). Dislocation density is a defect in which the layers of the crystals in the crystal lattice are dislocated from their original position. The graphical plot and the equation show that by increase in the number of unit cells the dislocation density of the lattice structure decreases.

The particle size is in direct relation with the number of unit cells. This is also confirmed by the relation between the particle size and the number of unit cells, $n = \pi\left(\frac{4}{3}\right) \times \left(\frac{D}{2}\right)^{3} \times \left(\frac{1}{V}\right)$. Here the number of unit cells is in direct relation with the third power of the particle size.

XRD cell volume

TiO₂ has tetragonal crystal symmetry [17]. Known the values of space groups the cell volume of tetragonal crystal symmetry of TiO₂, doped TiO₂ can be calculated using equation (7):

$$V = a^{2}c \quad (7)$$

where V is cell volume, and c represents the unit cell axis dimensions. The cell volume of TiO₂ and doped TiO₂ tetragonal system is $130.36 \times 10^{6} m^{-3}$.

XRD morphological index

The morphological index for TiO₂ tetragonal system was calculated from FWHM of the XRD data. The formula for calculation of morphological index is given in equation (8):

$$M.I. = \frac{FWHM_h}{FWHM_h + FWHM_p} \quad (8)$$

where M.I. represents the morphological index, $FWHM_h$ shows the highest FWHM value which was obtained from the peak. The values calculated for TiO₂ and doped TiO₂ tetragonal system are given in Tables 3 and 4.

XRD microstrain

Microstrain is defined as the variation across the individual crystallite lattice parameter in terms of root mean square. The microstrains of TiO₂ and doped TiO₂ tetragonal system were calculated using the formula shown in equation (9):

$$\varepsilon = \frac{\beta}{4 \tan \Theta} \tag{9}$$

where ε is the microstrain and β represents the FWHM of the diffraction peaks. Moreover, the relationship between the microstrain and the broadening is due to micro deformation [18]. The value of the microstrain cannot be negative. The values for TiO₂ and doped TiO₂ tetragonal system are given in Tables 3 and 4. The FWHM of the strain parameter also increases.

Table 3. FWHM (β), and microstrain (ε) of TiO₂ nanoparticles.

FWHM(β) (Radians)	Microstrain (Unitless)
0.0068	0.052
0.0061	0.008
0.0050	0.002
0.0061	0.072
0.0064	0.014
0.0099	0.024

Table 4. FWHM (β), and microstrain (ε) of doped TiO₂ nanoparticles.

FWHM(β) (Radians)	Microstrain (Unitless)
0.0121	0.212
0.0054	0.019
0.0082	0.039
0.0082	0.005
0.010	0.062
0.016	0.061
0.020	0.25

XRD instrumental broadening

When the particle size is less than 100 nm then substantial broadening in X-ray diffraction line will happen. Broadening will occur in the diffraction pattern due to the reduction of crystallite size and strain in the crystal system [19]. Both instrument and sample broadening combined to form total broadening shown by equation (10):

$$\beta^2{}_D = [\beta^2{}_{measures} - \beta^2{}_{Instrumental}] \tag{10}$$

$$D = \frac{K\lambda}{\beta_D \cos\Theta} \text{ or } \quad \cos\Theta = \frac{K\lambda}{D}\left(\frac{1}{\beta_D}\right) \tag{11}$$

$$\beta_{hkl} = \beta_s + \beta_D \tag{12}$$

where β_s is the sample broadening and β_D is the instrumental broadening.

$$\beta_{hkl} = \left(\frac{K\lambda}{\beta_D \cos\Theta}\right) + 4\,\varepsilon\,\tan\Theta \tag{13}$$

$$\cos\Theta\,\beta_{hkl} = \left[\left(\frac{k\lambda}{\beta_D}\right) + 4\,\varepsilon\,\sin\Theta\right] \tag{14}$$

Equation (14) stands for UDM (uniform deformation model) and means that the strain is uniform in all crystallographic directions, ε is the microstrain of the crystal system and instrumental broadening.

UV-Vis studies

Figure 3 shows the UV-Vis spectrum of the undoped TiO₂ and co-doped TiO₂ nanoparticles. The wavelength range of the spectrometer was set from 200 nm to 800 nm. The UV-Vis spectrum corresponding to undoped TiO₂ NPs dispersed in deionized water shows a broad absorption peak at 297 nm with a fundamental edge of absorption at 512 nm, which is formed by extrapolating the straight line to come across the X-axis. In the UV-Vis spectrum of the co-doped NPs a maximum absorption band appeared at 220 nm with a fundamental edge of absorption shifted toward higher wavelengths. The results show a red shift in the spectrum as compared to undoped TiO₂ NPs.
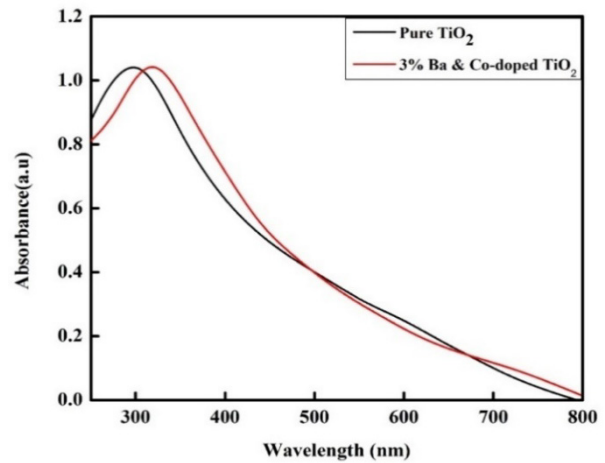
Fig. 3. UV-Vis spectra of TiO₂ and Ba-Co co-doped TiO₂ nanoparticles.
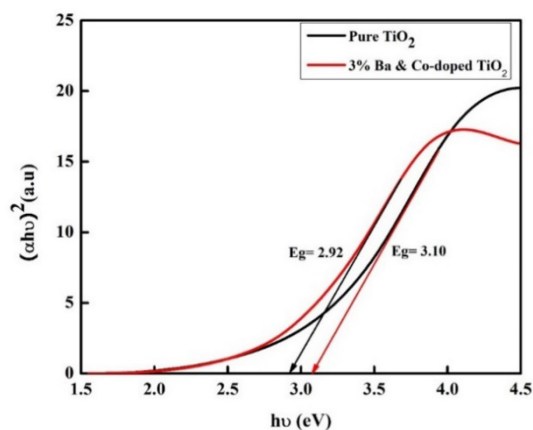
Fig. 4. Band gaps of TiO$_2$ and Ba-Co co-doped TiO$_2$ nanoparticles.

Band gap

The band gap values of undoped TiO$_2$ NPs and co-doped TiO$_2$ NPs were calculated using UV-Vis spectroscopic data as shown in Figure 4. The concerned equation (15) is given below.

$$\alpha h\upsilon = A(h\upsilon - Eg)^n \tag{15}$$

where α is the absorption coefficient, υ is the energy of photon, A is the proportionality constant, n is the transition index. The band gap values of TiO$_2$ and doped TiO$_2$ NPs came out to be 3.10 eV and 2.92 eV, respectively. The results show tuning in the band of doped TiO$_2$ as compared to undoped TiO$_2$ NPs.

FTIR studies

FTIR measurements were performed over the wave number range of 400-4000 cm^{-1}. Figure 5 shows the FTIR spectrum of undoped and doped TiO$_2$ NPs calcined at 500 °C. Small peaks in the range of 400-1000 cm^{-1} reveal the formation of anatase phase of TiO$_2$ NPs corresponding to bending mode of Ti-O-Ti. The broad peak at 3461 cm^{-1} corresponds to the O-H stretching of the alcohol solvent. The symmetric stretching vibration of the carboxylate group occurs at 1435 cm^{-1}. The symmetric and asymmetric vibration modes at 3010 cm^{-1} and 2986 cm^{-1} correspond to an alkyl chain. The intense peak at 1740 cm^{-1} corresponds to the reaction between acetic acid and TTIP in the formation of the ester in a sol-gel reaction. In the doped TiO$_2$, the vibration band at a position below 600 cm^{-1} is corresponding to the bending mode of the metal oxide [20].
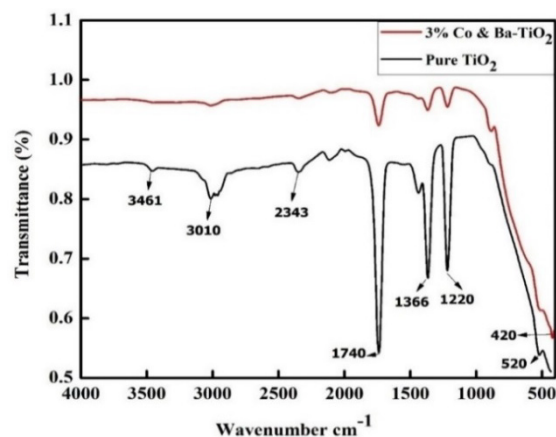
Fig. 5. FTIR spectra of TiO$_2$ and Ba-Co co-doped TiO$_2$ nanoparticles.

SEM studies

The morphologies of synthesized nanoparticles were analyzed through scanning electron microscopy. Figures 6a and 6b show the SEM images of undoped TiO$_2$ and doped TiO$_2$ NPs, respectively. The undoped TiO$_2$ clearly shows rough spherical morphology with small particle agglomeration. In the doped TiO$_2$ NPs slightly larger blocks of agglomerated particles with irregular morphology are present as compared to undoped TiO$_2$.
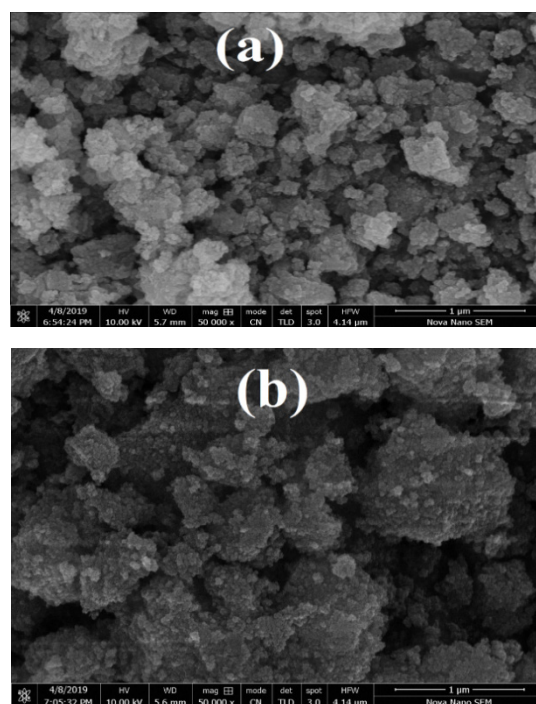
Fig. 6. SEM images of (a) TiO$_2$ and (b) barium and cobalt co- doped TiO$_2$ nanoparticles.

EDX studies

Elemental composition of barium and cobalt co-doped TiO_2 nanoparticles was studied using EDX to investigate the presence of elements in the synthesized nanoparticles as shown in Figure 7. Table 5 summarized the chemical composition of the obtained powders. The results show that the ratio of dopants present in the sample is in accordance with the theoretical value.
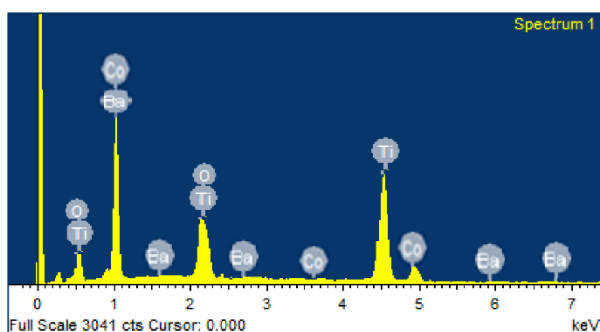
Fig. 7. EDX spectrum of Ba-Co doped TiO_2 nanoparticles.

Table 5. EDX composition of Ba-Co doped TiO_2 nanoparticles.

Sample	wt% (O)	wt% (Ti)	wt% Dopant (Ba & Co)
Ba & Co co-doped TiO_2	59.95	37.08	2.97

Mostly the titanium dioxide is doped with transition metals because the latter possess incomplete d-orbitals with variable oxidation state which enhance the photocatalytic activity of doped nanoparticles. An example is the capability of cobalt and barium to give Co^{2+}, Co^{3+} and Ba^{2+}, Ba^{3+} which retard the recombination of photo-generated carriers.

Due to the comparable atomic radii of cobalt and titanium, cobalt acts as a charge snare in the TiO_2 crystal. TiO_2 doping with such metals changes the optical band gap [21]. The photocatalytic degradation of wastewater containing organic dye under UV light was done using cobalt and barium doped TiO_2. The combination of cobalt and barium with TiO_2 tapers the titanium oxide band gap and causes a shifting of the absorption edge. The above discussed characteristic of Co and Ba doped TiO_2 improves the photocatalytic degradation of the organic dye.

Photocatalytic degradation of the dye

Effect of irradiation time. The photocatalytic degradation of Coomassive brilliant blue dye was monitored under UV-light at different time intervals ranging from 20 to 280 min. First the experiment was carried out under visible light irradiation but the degradation was not so fruitful. The synthesized undoped TiO_2 and Co-Ba co-doped photocatalyst were used for the degradation of Coomassive brilliant blue dye. About 0.01 mg of undoped TiO_2 and cobalt-barium co-doped TiO_2 were used for the degradation of same dye. Separate solutions of dye were taken in a 150 ml beaker.

The prepared dye solution was kept in a locally designed photoreactor chamber under constant stirring using a magnetic bar with a speed of 60 rpm. About 3 ml was collected from each sample after an interval of 20 min. In the intervals of 20 min all the reaction mixture was collected up to 240 min duration. After that each sample was centrifuged and analyzed using UV spectrophotometry. Initially the degradation of Coomassive brilliant blue was very low both for undoped TiO_2 and Co-Ba co-doped TiO_2 as is evident from the data in Table 6 because a smaller number of hydroxyl radicals was formed due to slow bond cleavage. When irradiation continued, around 48% degradation was observed in 40 min [22]. The absorption spectrum showed that 93% degradation took place in case of Co-Ba co-doped photo catalyst in 240 min, where 70% dye degradation was observed for undoped TiO_2 photocatalyst at the same interval of time.

The results showed that the highest degradation of Coomassive brilliant blue dye was observed using Co-Ba co-doped TiO_2, which is comparatively greater than that of undoped TiO_2. Table 6 and Figures 8 and 9 show the comparative % degradation of Coomassive brilliant blue dye with increasing time using Co-Ba co-doped TiO_2 and undoped TiO_2 photocatalyst.

Table 6. Comparative % degradation of Coomassive brilliant blue dye with increasing time using Co-Ba co-doped TiO_2 and undoped TiO_2 photocatalyst.

Time, (minutes)	20	40	60	80	100	120	140	160	180	200	220	240
% Degradation using Co-Ba co-doped TiO_2	47	48	48	51	56	60	60	66	70	74	88	93
% Degradation using undoped TiO_2	47	48	48	51	56	56	60	60	64	66	67	77
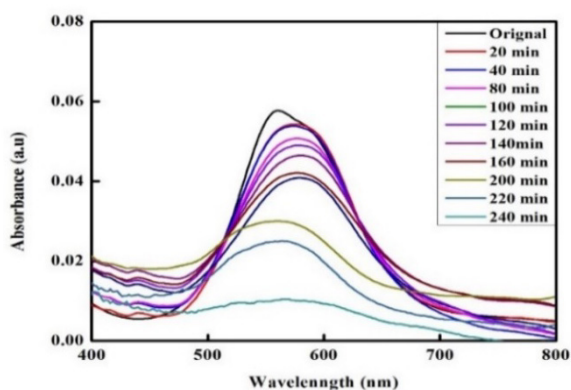
Fig. 8. Comparative % degradation of Coomassive brilliant blue dye with increasing time, using TiO_2 photocatalyst.
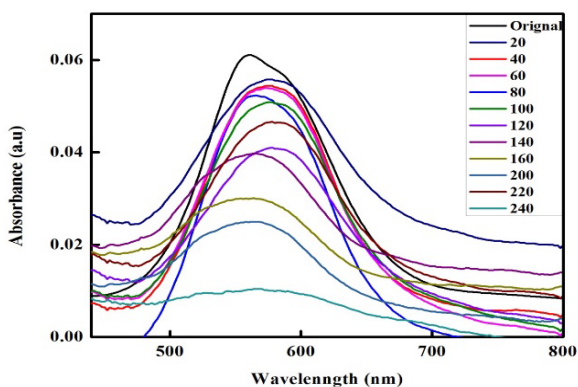
Fig. 9. Comparative % degradation of Coomassive brilliant blue dye with increasing time using Co-Ba co-doped TiO_2 photocatalyst.

Effect of dye concentration. The adsorption of dye molecules takes place at the surface of the photocatalyst. During the process of photocatalysis, the dye concentration should no+t be in the bulk of the solution but react with the present amount of photo catalyst in the given solution. In this study different concentrations of Coomassive brilliant blue dye were used in the course of experimentation keeping the amount of photocatalyst and irradiation time constant. Exactly 0.01 mg of both Co-Ba co-doped and undoped TiO_2 photocatalyst were used for different initial concentrations of Coomassive dye ranging from 10 ppm to 50 ppm. The data obtained during the experiment and the outcome of the process are presented in Table 7 and Figures 10 and 11.

It was found that with increase in the initial concentration of the Coomassive brilliant blue dye the % degradation decreases. When the concentration of Coomassive brilliant blue dye increased from 10 ppm, a stronger interaction between dye molecule and photocatalyst took place

which formed a large number of intermediate reactants that covered all the surface of the photocatalyst and protected it from further engagement, as a result the formation of hydroxyl radicals decreased. It should be considered that the water changes its physical property and becomes turbid due to higher concentration of dye by blocking the energetic photon to reach and activate the photocatalyst. After that there is no active site present here for the absorption of water to generate the hydroxyl ion which plays an important role in the degradation of dye [23, 24]. The percent degradation of the dye obtained by using different concentrations is shown in Table 7. It can be seen from the table that with an increase in concentration of dye, the active sites of the surface are occupied and ultimately more dye molecules take possession on the surface of the catalyst and screen the catalyst from upcoming light photons, which in turn decreases the approach of photon to reach the dye solution.

Fig. 10. Comparative % degradation of Coomassive
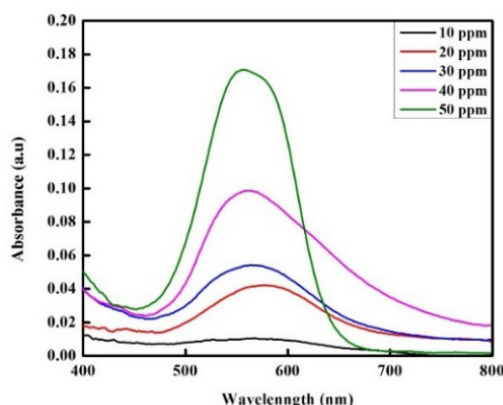
brilliant blue dye with increasing dye concentration using 0.01 mg of TiO_2 photocatalyst

The following table shows the comparative % degradation of Coomassive brilliant dye with increasing concentration of the dye from 10 ppm to 50 ppm using Co-Ba co-doped TiO_2 and undoped TiO_2photocatalyst. Again, it is clear that at low concentration (10 ppm) the dye degradation was maximum (94 %) in case of doped TiO_2 and 77% in case of undoped TiO_2. The rate of degradation decreased with increasing concentration of the dye as evident from the given tables and figures.

Table 7. Comparative % degradation of Coomassive brilliant blue dye with increasing dye concentration using Co-Ba co-doped TiO_2 and undoped TiO_2photocatalyst.

Concentration (ppm)	10	20	30	40	50
% Degradation using undoped TiO_2	77	75	73	71	59
% Degradation using Co-Ba co-doped TiO_2	94	83	77	75	60
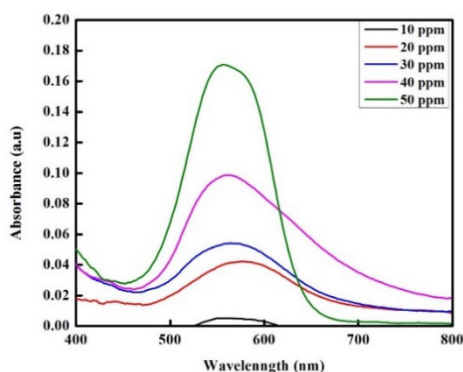
Fig. 11. Comparative % degradation of Coomassive brilliant blue dye with increasing dye concentration using 0.01 mg of Co-Ba co-doped TiO$_2$ photocatalyst.

Effect of catalyst dosage. The catalyst amount plays an important role in photocatalytic degradation of dye. The degradation process of dye must be investigated at different amounts of catalyst because a little increase or decrease on amount of catalyst can affect the rate of dye degradation. This is due to the fact that the increase in the amount of photocatalyst generates a large number of active sites on its surface and increases the number of hydroxyl radicals in the solution mixture. To study the effect of photocatalyst dosage; to the various solutions (10 ppm) of Coomassive brilliant blue dye different weights ranging from 0.01 mg to 0.05 mg of the catalysts were used. The experiment was carried out under UV light and the degradation time was 240 min. Degradation was noted using 0.01 mg, 0.02 mg, 0.03 mg, 0.04 mg, and 0.05 mg of undoped TiO$_2$ photocatalyst. The maximum degradation (85.5%) was obtained using 0.01 mg of TiO$_2$ photocatalyst.

After that when increased the amount of undoped TiO$_2$ catalyst up to 0.02 mg, 0.03 mg, 0.04 mg, 0.05 mg the degradation was found to decrease: 77%, 54%, 48%, and 38%, respectively (Table 8 and Figure 12).

For the same concentration of dye, 0.01 mg to 0.06 mg of Co-Ba-doped TiO$_2$ catalyst was used and 85%, 77%, 77%, 89%, and 95% degradation was observed (Table 8 and Figure 13). Using 0.05 mg of Co-Ba-doped TiO$_2$ 99.5% degradation was observed while using 0.01 mg of undoped TiO$_2$ it was 85.5%. In case of undoped TiO$_2$ it was observed that by increasing catalyst amount the degradation rate decreased. The reason behind is that the solution becomes turbid which covers all the surface of catalyst and forms a suspension which does not allow the photons to reach the surface of TiO$_{2n}$ photocatalyst and generate hydroxyl radicals [25, 26].
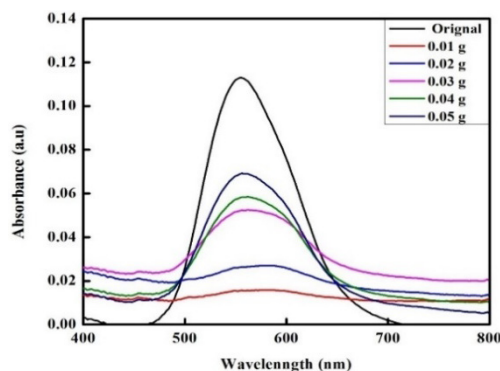
Fig. 12. Comparative % degradation of Coomassive brilliant blue dye with catalyst dose using undoped TiO$_2$ photocatalyst.

Table 8. Comparative % degradation of Coomassive brilliant blue dye with increasing amount of undoped TiO$_2$ and Co-Ba co-doped TiO$_2$.

Catalyst amount (mg)	0.01	0.02	0.03	0.04	0.05	0.06
% Degradation using undoped TiO$_2$	85.5	77	54	48	38	30
% Degradation using Co-Ba co-doped TiO$_2$	85	77	77	89	95	88

Table 9. Percent degradation obtained at various pH values by using undoped TiO$_2$ and Co-Ba co-doped TiO$_2$ photocatalyst.

pH value	3	4	5	8	9
% Degradation using undoped TiO$_2$	85	82	78	69	51
% Degradation using Co-Ba co-doped TiO$_2$	92	84	81	76	49

Fig. 13. Comparative % degradation of Coomassive brilliant+ blue dye with catalyst dose using Co-Ba co-doped TiO₂ photocatalyst**.**

The increase in degradation rate of Co-Ba-doped photocatalyst by increasing the amount from 0.01 mg to 0.05 mg can be explained in terms of generation of a large number of active sites on the surface of the doped photocatalyst and the uncovered surface of the catalyst for UV radiation whereas a great number of photons are available to reach catalyst surface and generate a large number of OH radicals which is responsible for typical discoloration. Furthermore, decrease occurred in the degradation of dye when we increased the catalyst amount from certain optimal level.

From Figure 13 it is clear that with increase in the amount of Co-Ba co-doped photocatalyst an increase in % degradation of CBB occurred.

Effect of pH. pH is the most essential parameter, therefore the degradation of Coomassive dye was investigated at various pH values. From the standard stock solution of Coomassive brilliant blue dye 100 ml of different solutions each having a concentration of 10 ppm were prepared. The pH was adjusted to 3, 4, 5, 6, 8 and 9.

The pH of Coomassive dye solution was calibrated by using 0.1 molar HCl and 0.1 molar NaOH earlier in the experiment. The natural pH value of Coomassive brilliant blue dye is 5.5 which shows its amphoteric character so that it may generate positive or negative charge on its surface during degradation process. The results showed that maximum degradation occurred at pH below 5 which indicates that the optimum pH for degradation was acidic due to the formation of a cation moiety (like hydronium ion) upon protonation which increases its oxidizing ability thus maximum degradation 85% was observed at pH=3 while in a basic medium (pH=9) it was 51% (Figure 15). The effect of proton and hydroxyl is given below:
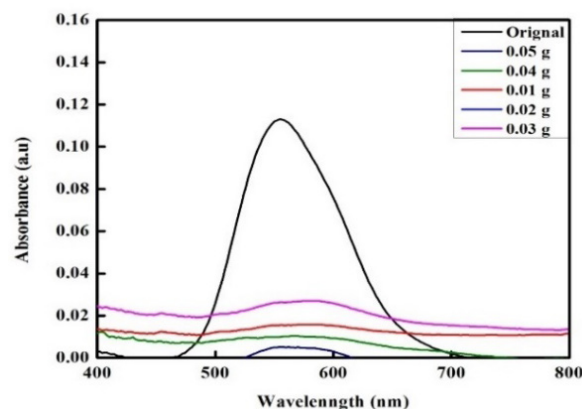
Fig. 14. Comparative % degradation of Coomassive brilliant blue dye with pH using 0.05 g of undoped TiO₂.

$$TiOH + H^+ \longrightarrow TiOH_2^+$$

$$TiOH_2^+ + H_2O \longrightarrow TiOH + OHTiO$$

The reason behind this is that in acidic medium the titania surface gets protonated and becomes positively charged while in alkaline medium the surface is covered by electrons and becomes negatively charged.
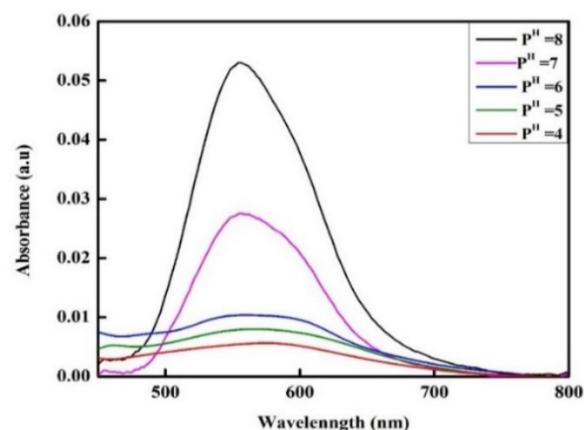
Fig. 15. Comparative % degradation of Coomassive brilliant blue dye with pH using 0.05 g of Co-Ba co-doped TiO₂ photocatalyst.

The higher catalytic activity of TiO₂ photocatalyst is reported in acidic medium and it acts as a Lewis acid. However, a higher concentration of H⁺ can also lower the rate of the reaction from the optimum level. In the presence of a positive charge TiO₂ shows good oxidizing activity. In this case the Coomassive dye acts as a Lewis base and easily adsorbs on the surface of anionic TiO₂ catalyst. This helps the accumulation of the dye at the lower pH. In basic conditions this type of complexation does not take place because of the comparable adsorption of hydroxyl group and the Coomassive dye molecule. In addition, electronic repulsion occurs because of

indirect charge of the catalyst with the dye molecules. In case of Co-Ba co-doped TiO₂ photocatalyst efficient degradation of Coomassive dye occurs in acidic medium (pH=3) - the degradation efficiency of dye is 92% while in basic medium (pH=9) it equals 49% (Figure 15). The reason behind the higher degradation at lower pH could be rationalized by the iso-electric point of TiO₂. It is known from the literature survey that the exact zero-point charge of Co and Ba co-doped TiO₂is at pH 6.8. Therefore, at a pH lower than 6.8 the surface of TiO₂ becomes positively charged, and will negatively charge at a pH higher than 6.8. On this justification at pH<6.8 the concentration of positive charges increases on the surface of catalyst. As a result, a higher photocatalytic degradation takes place at acidic pH due to the positively charged surface of the doped photocatalyst and generation of a higher concentration of hydroxyl radicals which are responsible to increase the degradation speed in acidic environment. However, the decrease in decolorization efficiency at basic pH is due to the presence of negative charges at the surface of the doped photocatalyst. The available negative charge causes electrostatic repulsion among the negatively charged Coomassive dye and TiO₂ nanoparticles. It follows from the above discussion that the degradation of Coomassive dye decreases in alkaline medium and increases in acidic medium, the maximum degradation being reported at pH=3 using both undoped and doped titanium dioxide photocatalyst [27, 28]. The % degradation obtained at various pH values is briefly presented in Table 9.

CONCLUSIONS

By doping with Co and Ba the band gap of TiO₂ NPs decreased. Using bare and co-doped TiO₂ NPs for the photocatalytic degradation of Coomassive brilliant blue dye the percent degradation increased with increase in the irradiation time and decreased with increase in the dye concentration. Increasing the amount of co-doped TiO₂ NPs the rate of degradation increased while in case of bare TiO₂ it decreased. Higher degradation was noticed at low pH while it decreased with increase in pH. Co-Ba-doped TiO₂ NPs can effectively be used for the degradation of Coomassive brilliant blue dye in aqueous medium.

Conflict of Interest
There is no conflict of interest between the authors.

REFERENCES

1. Q. Sun, K. Li, S. Wu, B. Han, L. Sui, L. Dong, *New J. Chem.*, **44**, 1942 (2020).
2. M. Rauf, S. Ashraf, S. Alhadrami, *Dyes and Pigments*, **66**, 197 (2005).
3. E. Pino, C. Calderón, F. Herrera, G. Cifuentes, G. Arteaga, *Fron. Chemist.*, **8**, 365 (2020).
4. A. Ajmal, I. Majeed, R.N. Malik, H. Idriss, M.A. Nadeem, *RSC Adv.*, **4**, 37003 (2014).
5. A. Kumar, G. Pandey, *Mater. Sci. Eng. Int. J.,* **1**, 1 (2017).
6. Y. Li, W. Wang, F. Wang, L. Di, S. Yang, S. Zhu, Y. Yao, C. Ma, B. Dai, F. Yu, *Nanomater.*, **9**, 720 (2019).
7. M. Okano, K. Itoh, A. Fujishima, K. Honda, *J. Electrochem. Soc*., **134**, 837 (1987).
8. M.B. Mukhlish, F. Najnin, M.M. Rahman, M. Uddin, *J. Sci. Res.,* **5**, 301 (2013).
9. M. Amini, M. Ashrafi, *Nanochem. Res.,***1**, 79(2016).
10. G. Sadanandam, K. Lalitha, V.D. Kumari, M.V. Shankar, M. Subrahmanyam, *Int. J.Hydrogen Energy*, **38**, 9655 (2013).
11. C. Lv, X. Lan, L. Wang, Q. Yu, M. Zhang, H. Sun, J. Shi, *Catal. Sci. Technol.,***9**, 6124 (2019).
12. P. V. Kamat, Photophysical, photochemical and photocatalytic aspects of metal nanoparticles, ACS Publications, 2002.
13. D. S. Meshesha, R. C. Matangi, S. R. Tirukkovalluri, S. Bojja, *South Afr. J. Chem. Eng.,* **23**, 10 (2017).
14. X. Hong, Z. Wang, W. Cai, F. Lu, J. Zhang, Y. Yang, N. Ma, Y. Liu, *Chem. Mater.,* **17**, 1548 (2005).
15. M. A. Islam, M.J. Haither, I. Khan, M. Islam, I*OSR . Electric Electron Eng.,*3, 18 (2012).
16. V. Manikandan, A.K. Palai, S. Mohanty, S.K. Nayak, *J. Photochem. Photobiol. B: Biology,* **183**, 397 (2018).
17. M Ahmed, E.E. El-Katori, Z.H. Gharni, *J. Alloys Comp.,* **553**, 19 (2013).
18. J. Haider, Z.N. Jameel, S.Y. Taha, *Eng. Technol. Jour.,* **33**, 761 (2015).
19. E. Filippo, C. Carlucci, A.L. Capodilupo, P. Perulli, F. Conciauro, G. A. Corrente, G. Gigli, G. Ciccarella, *Mater. Res.,***18**, 473 (2015).
20. A. Caricato, S. Capone, G. Ciccarella, M. Martino, R. Rella, F. Romano, J. Spadavecchia, A. Taurino, T. Tunno, D. Valerini, *Appl. Surf. Sci.,* **253**, 7937 (2007).
21. S. Salvi, P. Lokhande, H. Mujawar, Photodegradation of Rhodamine 6G dye by Cd, Sr doped ZnO photocatalyst, synthesized by mechanochemical method, International Conference on Communication and Signal Processing 2016 (ICCASP 2016), Atlantis Press, 2016.
22. A. Dodd, A. McKinley, T. Tsuzuki, M. Saunders, *Mater. Chem.Phys.,* **114**, 382 (2009).
23. N. Daneshvar, D. Salari, A. Khataee, *J. Photochem. Photobiol. A: Chemistry,* **162**, 317 (2004).
24. Z. Mengyue, C. Shifu, T. Yaowu, *J. Chem. Technol. Biotechnol.,* **64**, 339 (1995).

25. E. M. Saggioro, A. S. Oliveira, T. Pavesi, C. G. Maia, L. F. V. Ferreira, J.C. Moreira, *Molecules*, **16**, 10370 (2011).
26. K.M. Reza, A. Kurny, F. Gulshan, *Appl. Water Sci.,* **7**, 1569 (2017).
27. B. Viswanathan, *Curr. Catal.,* **7**, 99 (2018).
28. A. M. Santhosh, K, K. M.Yogendra, I.H. Mahadevan, N. Mallikarjuna, Madhusudhana, *J. Technol. Innov. Res.(JETIR)*, **5**, 2349 (2018).

The performance of activated carbon in Al-ion based supercapacitors

B. Shenbagabalakrishnan*, V. Gayathri

Nanomaterials Research Laboratory, Department of Physics, Thiagarajar College of Engineering, Madurai - 625015, India

Activated carbon (AC), an extraordinary material, is vital in supercapacitor applications. The use of flower stalks from coconut tree (FSCT), as a raw material for synthesis is the highlight of our research. AC is produced by utilizing aluminium chloride hexahydrate ($AlCl_3.6H_2O$) as an activating agent in the chemical activation procedure. The BET surface area of the synthesized carbon material is about 50 m^2g^{-1} with high content of micropores. In this context, most of the pores have a 0.5-1 nm diameter. AC demonstrates excellent electrochemical performance in 5M aqueous aluminium nitrate nonahydrate ($Al(NO_3)_3.9H_2O$) electrolyte and exhibits a specific capacitance value of 64 Fg^{-1} at 0.1 Ag^{-1} and equivalent serial resistance (ESR) of 23 Ω, measured by impedance spectroscopy. It is worth noting that the retention of the capacitance of the electrode was sufficiently high even after 1000 cycles.

Keywords: Flower stalks, Amorphous carbon, Activating agent, Al ion, Supercapacitor, Capacitance retention, Nyquist plot

INTRODUCTION

Clean, renewable energy production and energy storage is the primary solution to environmental pollution and the depreciation of fossil fuels [1]. The requirements of high energy and power density are the main scope of research in energy and fuels [2]. Various techniques are available to improve the supercapacitors energy density, e.g., the presently investigated hybrid capacitors, composite electrodes and multivalent ion-based electrolytes [3]. Multivalent ion-based electrolytes got great attention compared to univalent ion electrolytes due to the larger number of electron transitions [4]. Aluminium is an excellent multivalent ion electrolyte among others, due to its smaller ionic radius, high volumetric and gravimetric capacity and safety aspects [5]. Since the size of an electrolyte ion is smaller than the size of a micropore of AC, it can access a larger specific surface area of the pores, which leads to achieving an increased value of specific capacitance [6]. In this context, the Al ion with low ionic radius is a more suitable electrolyte ion for porous electrodes to enhance the specific capacitance. Carbon is a pearl in the sea of energy storage due to its properties such as inertness and stability of material with a wide potential window, cost-effectiveness and abundance [7]. Porous carbon, among other forms of carbon structures, is well adopted in energy storage, CO_2 capture, hydrogen storage and water treatment applications [8-10]. Hence, it becomes a promising electrode material.

Physical and chemical activation are the two techniques adopted to obtain activated carbon [11, 12]. The second route is the simplest and most efficient way of getting AC using chemical agents like KOH and $ZnCl_2$ [13-15]. Compared to other activating routes, KOH-based activation has produced highly microporous AC [16]. In recent times, the performances of AC as an electrode in different electrolytes are highlighted in the literature as follows: $H_4P_2O_7$-activated carbon from leather waste has a surface area of 381 m^2g^{-1}, which gives a specific capacitance of 550 Fg^{-1} in 6M KOH electrolyte [17].

Biomass is activated by KOH pre-treatment for 18 h. It has a high micropore surface area of 639 m^2g^{-1} and a pore volume of 0.26 cm^3g^{-1}, which gives a specific capacitance of 162 Fg^{-1} in 6M KOH electrolyte [18]. Spent coffee grounds precursor is activated with KOH at a ratio of 1:1.5, affording a specific surface area of 2330 m^2g^{-1}, providing a specific capacitance of 84 F/g [1] at 1A g^{-1} in 1M Na_2SO_4 electrolyte [19]. Some authors have used H_3PO_4 as an activating agent to prepare durian shell-based AC with a surface area of 2004 $m^2 g^{-1}$ and a pore diameter of 3.34 nm. They have reported a specific capacitance of 93.1 Fg^{-1} in 1.5M Na_2SO_4 electrolyte [20].

Novel activated carbon will be produced by an original chemical activation procedure, using aluminium chloride as an activating agent. The micropores of activated carbon play an important role in enhancing the specific capacitance of the supercapacitor. It is worth mentioning that $AlCl_3$ is expected to improve the porosity of the carbon. To our knowledge, there are no literature data on the production of activated carbon with this activating agent.

EXPERIMENTAL

The flower stalks of the coconut tree (FSCT) were taken as the source of carbon, and aluminium chloride hexahydrate ($AlCl_3. 6H_2O$ [A.R. grade from Kemphasol, India]) was used as an activating agent. Aluminium nitrate nonahydrate ($Al(NO_3)_3.9 H_2O$) from Merck acted as an aqueous electrolyte. The raw fresh FSCT was thoroughly

washed with distilled water to remove dirt and impurities, followed by a complete sundry. Then it was heated for 6 h in a muffle furnace at 500° C. The activating agent was prepared by mixing $AlCl_3$ powder with distilled water at 0.1 mg/ml concentration. Carbon powder of weight 0.5 g already derived from flower stalks was soaked in this solution for 24 h and then rinsed several times with distilled water to remove any residuals present in the material. After this step, it was completely dried out for hours and then heated in a microwave oven for 3 min. Thus, we get the microporous carbon which is ready to use. The methodology of our work is presented in Fig. 1. The structural analysis of the sample was performed using Bruker D8 Advance X–ray diffractometer, with Cu Kα as the source and scintillation counter as a detector. The measured angle ranged from 10° to 80°, as shown in Fig. 2(a). To investigate the disorders and the presence of impurities, Raman spectra of the sample were recorded with a He–Cd laser of 325 nm wavelength (Horiba Jobin Yvon of LabRAM HR Evolution Model). The Raman spectrum for the sample was taken in the range of 0 to 4000 cm^{-1}, which is indicated in Fig. 2(b). The morphological studies of the sample were performed on a VEGA3 TESCAN scanning electron microscope. The SEM image in the 2 μm range with a magnification of 10kX is shown in Fig. 3(a). Jeol / JEM 2100 HRTEM with

LaB6 electron gun was used to study the surface nature of the sample, and the images in the 20 nm scale are presented in Fig. 3(b). BET surface area and pore analysis were performed with the help of BELSorp – max, BEL Japan, Inc. For this, the degassing temperature was fixed at 200°C at a pressure of 2.096×10^{-4} Pascal and kept for 2 h to remove the adsorbed impurities on the sample, if any.

The 'as-prepared' AC was investigated to evaluate its electrochemical properties with the help of an Auto lab electrochemical workstation. Further analysis was carried out by cyclic voltammetry (CV), Galvan static charge/discharge (GCD) and EIS. All the data were taken through a standard three-electrode system. For this study, platinum wire was taken as a counter electrode, Ag/AgCl as a reference electrode and a 3 mm diameter glassy carbon as a working electrode. The sample was pasted on the bottom of the surface, which is a working electrode in a mass of 1.12 mg and dried at 70°C for 12 h. The sample consisted of 80% active material (AC), 15% carbon black, and 5% PTFE as a binder. To get better results, the working electrode was dipped into 5M aqueous Al-ion electrolyte (prepared from $Al(NO_3)_3$ powder) for 2 h before starting the measurement. The CV studies were recorded in the potential range from 0 to 1 V, and the EIS analysis was carried out by applying input frequency in the range of 10 kHz to 0.1 Hz at a perturbation of 5 mV.
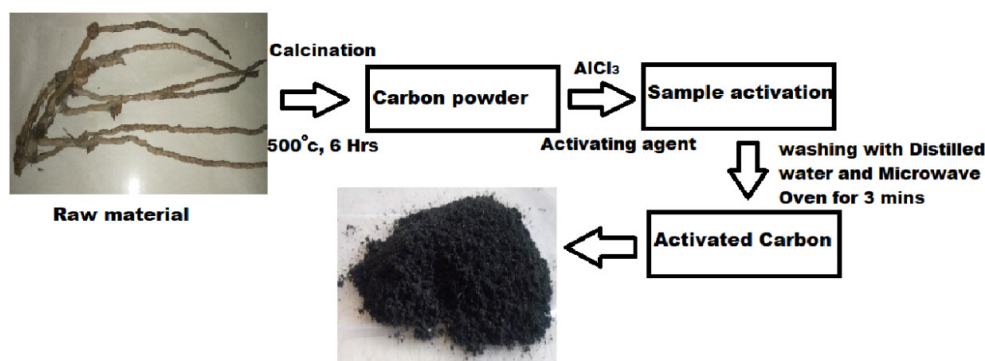
Figure 1. Step-by-step preparation process of AC from FSCT
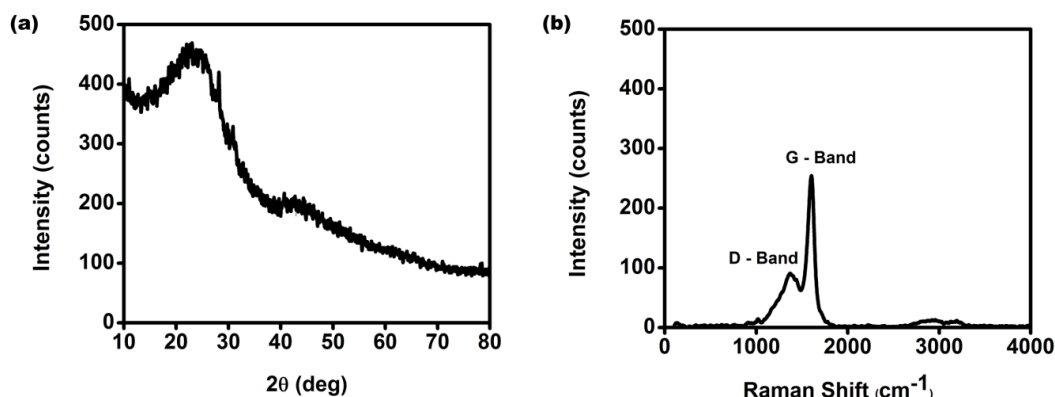
Figure 2. (a) XRD pattern of AC prepared from flower stalks of the coconut tree; (b) Raman spectrum of the AC sample showing the peaks of D and G-bands

RESULTS AND DISCUSSION

X-ray diffraction analysis

The prepared AC sample was probed through X-ray diffraction analysis. The following information was then congregated. The prominent peaks' positions in 2θ angle were around 25° and 44° shown in Fig. 2(a), which represent (002) and (100) planes of orientation, respectively (compared with JCPDS No: 75-1621) [21]. At the same time, the broad width of the peak shows that it is an amorphous material; that is, its crystallite size is very small (i.e., ~ 1 nm). This concise range of definite orderly atom arrangements also confirms its amorphous nature [22]. There are two conflict peaks observed in the Raman spectrum corresponding to D–band (1369 cm^{-1}) and G–band (1604 cm^{-1}), which are presented in Fig. 2(b). In addition, the spectrum also shows a broad peak with lower intensity in and around 3000 cm^{-1}, which we predict to come from the 2D band. In the Raman spectra, the vibration from the C=C in-plane is called a G-band. This deliberately indicates the purity of carbon materials [23], whereas the D-band comes from the 'out of plane vibrations'. This evinces the structural disorder like vacancies or adsorbed impurities that befall. The intensity of the D-band dropped when contrasted with the G- band, i.e., the I_D / I_G ratio (0.36) substantiated that the level of defects is very low [24].

Scanning electron microscopy analysis

The SEM image illustrates the sheet-like morphology of the sample, which is shown in Fig. 3(a), whereas the HRTEM seems spongy and permeable in nature, as presented in Fig. 3(b) and also exhibits a larger number of narrow pores on the surface. The pore diameter measured from the TEM image is approximately in the range of 2 to 10 nm. The obtained data demonstrate that the nitrogen low-temperature adsorption isotherm (Fig. 4(a)) belongs to type-I according to IUPAC classification, where the amount of adsorbed nitrogen gas molecules approaches saturation of total pore volume at a limiting value of 17 cm^{3}g^{-1}. This uptake is governed by the accessible micropore volume rather than the internal surface area. A steep uptake at very low p/p_0 is due to enhanced adsorbent–adsorptive interactions in narrow micropores, resulting in micropore filling. Generally, for nitrogen and argon adsorption at 77K and 87K, microporous materials of width < ~ 1nm give type-I(a) isotherms whereas materials having pore size distributions over a broader range, including wider micropores and possibly narrow mesopores (< ~ 2.5 nm), show type-I (b) isotherms. Our sample having micro and mesopores exhibits a type-I(b) isotherm, as expected. The obtained results indicated an H4 hysteresis loop that agrees with the IUPAC classification for a sample with micro-mesoporous nature [25]. This was further confirmed by Barrett, Joyner, and Halenda's (BJH) plot, where we observed the diameter of most of the pores to be ~ 0.9 nm, occupying almost 90% of the sample volume. Pores of diameter ranging from 0.4 nm to 2 nm were also present in this sample within a smaller volume, as presented in Fig. 4(b). The sample's surface area was calculated through BET, and it worked out to be 50 m^{2}g^{-1}.
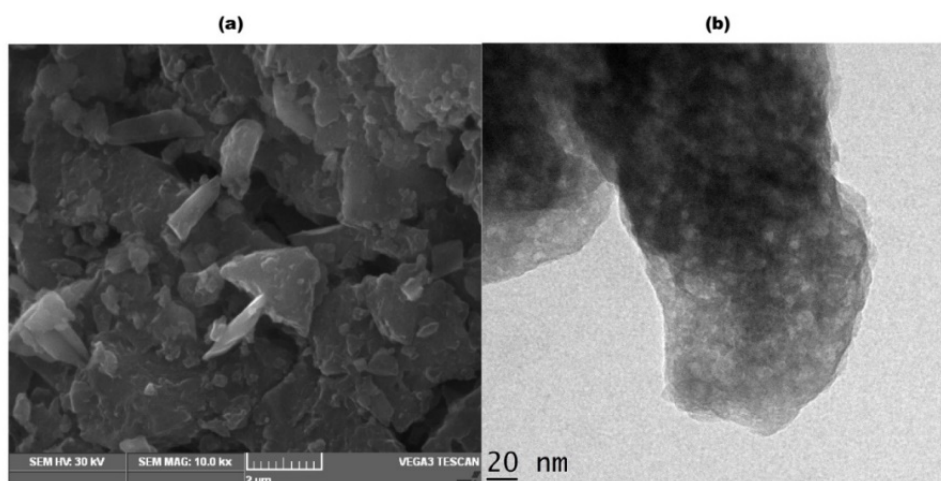
Figure 3. (a) SEM image of AC; (b) as-prepared AC HRTEM image with magnification
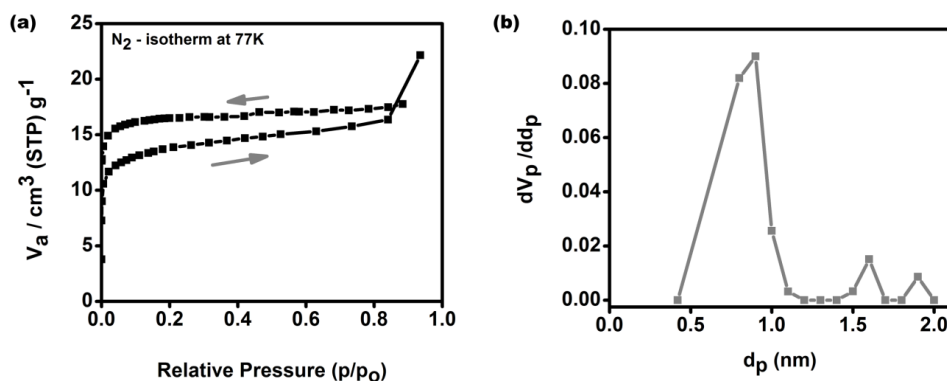
Figure 4. (a) N_2 adsorption and desorption isotherm; (b) pore size distributions of AC
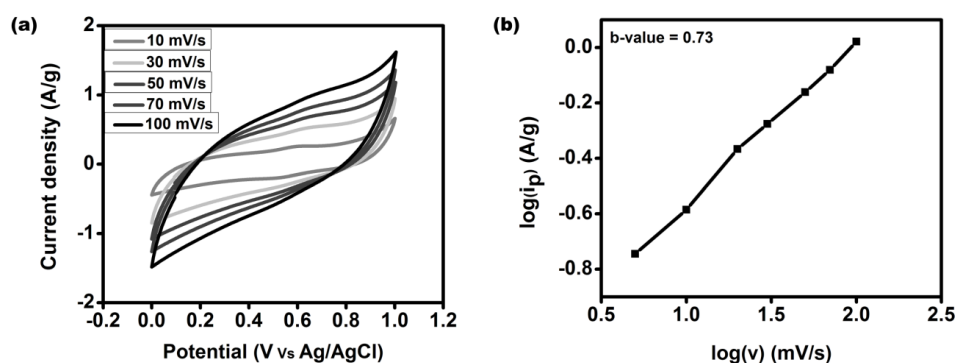
Figure 5. (a) CV of AC at various scan rates ranging from 10 mVs^{-1} to 100 mVs^{-1}; (b) b-value graph for the AC electrode plotted in-between scan rate and peak current of cathodic sweeps

Electrochemical behavior

To understand the electrochemical behavior of the sample, a three-electrode system was employed in the CV and GCD measurements. The CV was measured over the sample's potential range of 0 to 1V is in 5 M Al(NO$_3$)$_3$ electrolytic solutions. The CV showed that the sample exhibits a quasi-rectangular shape because of the double layer and pseudo-capacitance behavior, as shown in Fig. 5(a). The pseudo-capacitance behavior was due to the intercalation/deintercalation of Al ions into the pores of AC [30]. The contribution of pseudo capacitance was high at the lower scan rate, and became less when the scan rate was increased while at the lower scan rate, the ions get enough time to isntercalate into the pores of AC [31].

There occurred a cathodic peak at 0.6V and an anodic peak at 0.5V. Therefore, if no peak occurs, the EDLC's contribution significantly affects the higher scan rate [26]. Fig. 5(b) shows that the cathodic peak current linearly varies according to the corresponding scan rates. In this context, the calculated b-value of 0.73 confirms the presence of dual capacitance. From Fig. 6(a), let's compare the galvanostatic charge and discharge profiles of two different current densities with individual time scales. The tiger-tooth-shaped charge and discharge patterns deliberately show the existence of dual capacitance. This is discussed briefly in the CV curve itself. In particular, around 30% of its total charge was given while discharging, and the remaining charges were delivered slowly. The short time taken for charging and discharging depicts its high suitability for supercapacitor applications. The specific capacitance calculated from GCD at 0.1 Ag^{-1} was 64 Fg^1 and was compared with other electrolytes, (see Table 1). From this, we can see that our sample provides high specific capacitance even at the low surface area for dual capacitance. Further, the feature of micropores of the AC and low ionic radius of the Al^{3+} ions also contribute to this enhancement.

Fig. 6(b) gives the exponential variation of the specific capacitance concerning the current density. The capacitance retention rate for 1000 cycles was gradually amplified due to the electrochemical activation of the electrode through the diffusion of Al^{3+} ions into the pores consecutively during GCD, as given in Fig. 6 (c). This is confirmed by the enlargement of the CV curve taken after the GCD cycles compared to the starting state, as shown in Fig. 7(a). Fig. 7 (b) shows the sample's complex plane plot (Nyquist plot). It unveils the impedance in different frequency regions. We have obtained an ESR value of ~23 Ω, corresponding to the kinetics of Al^{3+} ions on the surface of the electrode. The absence of semi-circle reveals that the activated carbon manifests EDLC nature [28], and the slope at just above 45° angle in the low-frequency region elucidates the diffusion limitations due to the intercalation/deintercalation of Al^{3+} ions into the pores [29]. After several cycles, the impedance spectrum slightly reduces the ESR value. Also, the angle of slope deviates from capacitor's behavior and confirms the electrode's electrochemical activation through the diffusion of Al^{3+} ions into the pores, as indicated in Fig. 7 (b).

100
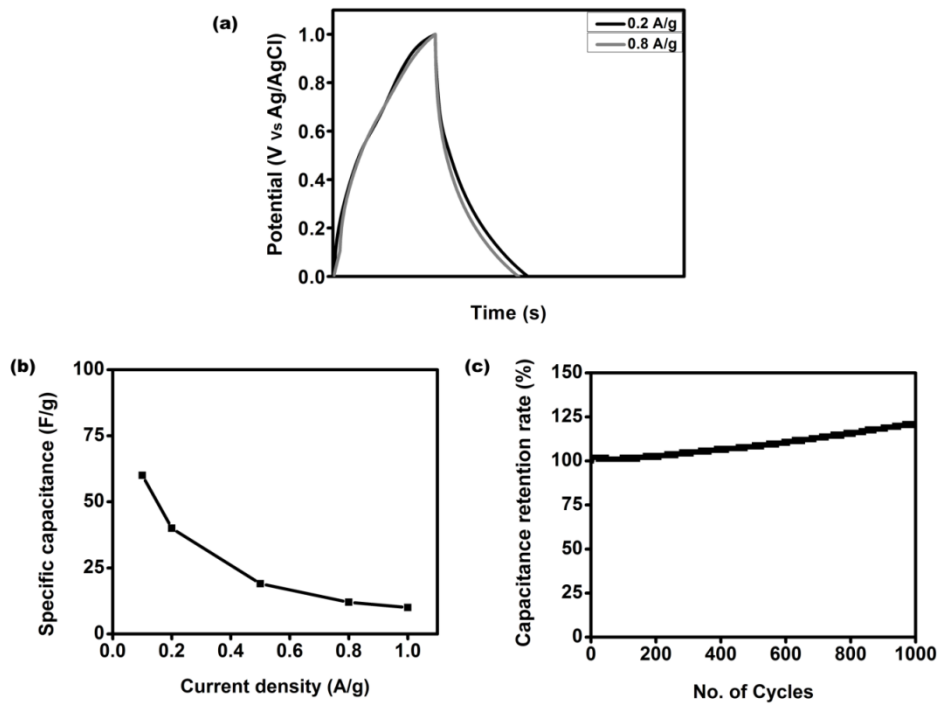
Figure 6. Comparison of the GCD curve for two different current densities: (a) 0.2 and 0.8 Ag^{-1}; (b) calculation of specific capacitance for AC electrode for various current densities from 0.1 to 1 Ag^{-1}; (c) retention of specific capacitance up to 1000 GCD cycles.

Table 1. Performance of AC with different electrolytes

Electrolyte	Surface area (m^{2}g^{-1})	Avg. pore diameter (nm)	Specific capacitance (Fg^1)	Potential window (V)	Ref.
1M Na$_2$SO$_4$	2330	-	84	1.9	[19]
1M H$_2$SO$_4$	614	3.4	74	0.8	[30]
6M KOH	900	2.32	73	0.9	[31]
5M Al(NO$_3$)$_3$	50	0.9	64	1	This work
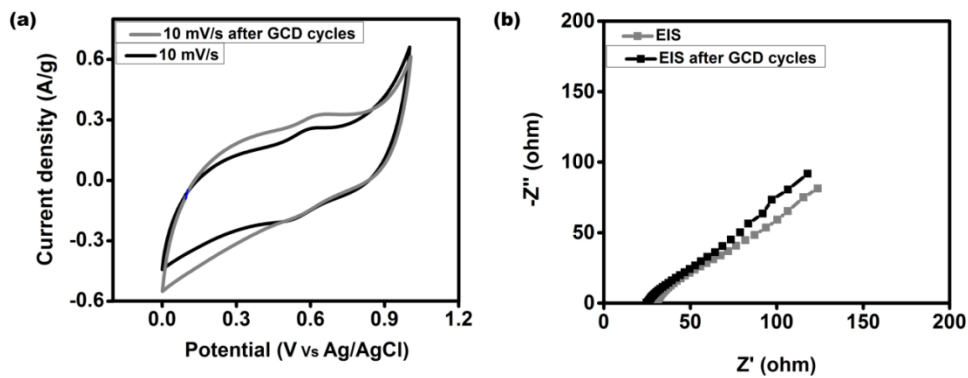
Figure 7. Cyclic voltammograms and complex plane plots of AC before (a) and after (b) 1000 GCD cycles.

CONCLUSIONS

In the present work, we have incorporated two novel ideas: an electrolyte based on multivalent ions and an electrode of AC prepared using $AlCl_3.6H_2O$ as an activating agent. AC prepared from flower stalks from the coconut tree (natural and inexpensive) proved to be an efficient electrode material with outstanding performance as a supercapacitor with Al ion-based electrolyte. The prepared sample has amorphous nature with very slight structural defects. The as-prepared AC exhibited double-layer capacitance, as well as pseudo-capacitance behavior. This dual behavior is due to the intercalation/deintercalation of Al ions into the pores of the AC. This becomes one of the most important factors in giving a high specific capacitance value of 64 Fg^{-1}, even though the sample's surface area is low. From this analysis we concluded that $AlCl_3$ can also effectively act as an activating agent to create micropores on the surface of AC. Further, enlargement of the surface area is possible by increasing the ratio between the activation agent and carbon, which is in progress. We could observe that this nature-derived AC is aptly suitable for aqueous-based Al ion supercapacitor applications.

Conflicts of interest: The authors declare no conflicts of interest.

REFERENCES

1. G. Olabi, C. Onumaegbu, T. Wilberforce, M. Ramadan, M. A. Abdelkareem, A. H. Al-Alami, *Energy*, **214**, 118987 (2021).
2. K. Sharma, A. Arora, S. K. Tripathi, *J. Energy Storage*, 21, (2019).
3. J. Cao, H. Xu, J. Zhong, X. Li, S. Li, Y. Wang, M. Zhang, H. Deng, Y. Wang, C. Cui, M. Hossain, Y. Cheng, L. Fan, L. Wang, T. Wang, J. Zhu, B. Lu, *ACS Appl. Mater. Interface*, **13**, 7 (2021).
4. Ponrouch, J. Bitenc, R. Dominko, N. Lindahl, P. Johansson, M. R. Palacin, *Energy Storage Mater.,* **20**, 253 (2019).
5. S. K. Das, S. Mahapatra, H. Lahan, *J. Mater, Chem. A*, **5** (14), 6347 (2017).
6. J. A. Lin Ritter, B. N. Popov, *J. Electrochem. Soc.,* **146** (10), 3639 (1999).Y. Wang, L. Zhang, H. Hou, W. Xu, G. Duan, S. He, K. Liu, S. Jiang, *J. Mater. Sci.*, **56**(1), 173 (2020).
7. M. Mohan, V. K. Sharma, E. A. Kumar, V. Gayathri, *J. Energy Storage*, **1** (2), 35 (2019).
8. S. He, G. Chen, H. Xiao, G. Shi, C. Ruan, Y. Ma, H. Dai, B. Yuan, X. Chen, X. Yang, *J.Colloid Interface Sci.,* **582**, 90 (2021).
9. S. A. Borghei, M. H. Zare, M. Ahmadi, M. H. Sadeghi, A. Marjani, S. Shirazian, M. Ghadiri, *Arab. J. Chem.,***14** (2), 102958 (2021). .
10. H. Shang, Y. Lu, F. Zhao, C. Chao, B. Zhang, H. Zhang, *RSC Adv.,***5** (92), 75728 (2015).
11. M. Sevilla, R. Mokaya, *Energy Environ. Sci.*, **7** (4), 1250 (2014).
12. M. M. Baig, I. H. Gul, *Biomass and Bioenergy*, **144**, 105909 (2021).
13. S. Suhdi, C. Wang, *Appl. Sci.,***11** (9), 3994 (2021).
14. Z. Higai, E. Huang, W. Qian, *Environ. Prog. Sustain. Energy,* **40** (2) (2020).
15. R. Hidayu, N. Muda, *Procedia Eng.,* **148**, 06 (2016).
16. S. I. El-Hout, S. Y. Attia, S. G. Mohamed, S. M. Abdelbasir, *J. Environ. Manag.,* **304**, 114222 (2022).
17. G. A. Yakaboylu, C. Jiang, T. Yumak, J. W. Zondlo, J. Wang, E. M. Sabolsky, *Renew. Energy*, **163**, 276 (2021).
18. L. Adan-Mas, P. Alcaraz, F. Arévalo-Cid, A. López-Gómez, F. Montemor, *J. Waste Manag.,***120**, 280 (2021).
19. J. P. Tey, M. A. Careem, M. A. Yarmo, A. K. Arof, *Ionics*, **22** (7), 1209 (2016).
20. P. Mavin, J. Wirat, L. Paveena, *Mater. Res. Express*, **9**, 065603 (2022).
21. B. R. Puri, L. R.Sharma, *ShobanLalNagin Chand and Co*, **31**3 (1992).
22. S. Divya T. Nann, *ChemElectroChem*, **8** (3), 492 (2020).
23. R. D. Nagarajan, A. K. Sundramoorthy, *Sens. Actuators B Chem.,* **301**, 127132 (2019).
24. M. Thommes, *Chem. Int.*, **38** (1), 25 (2016).
25. K. C. Tsay, L. Zhang, J. Zhang, *Electrochim. Acta*, **60**, 428 (2012).
26. X. Luo, Y. Chen, Y. Mo, *New Carbon Mater.*, **36**, 49 (2021).
27. B. E. Conway, Electrochemical supercapacitors: scientific fundamentals and technological applications. Springer Science & Business Media, 2013.
28. M. A. Scibioh, B. Viswanathan, Materials for Supercapacitor Applications, Elsevier, 2020, p. 336.
29. M. Jain, M. Ghosh, S. Krajewski, Kurungot, M. Michalska, *J. Energy Storage*, **34**, 102178 (2021).
30. M. P. Chavhan, S. Ganguly, *Ionics*, **23**, 2037 (2017).

Chemical kinetics: cyclisation reaction of hydrazinecarbothioamide, thioacetamide, and thiobenzamide with ethyl 2-bromoacetate

P. S. Sadavarte, B. H. Zaware*, S. J. Takate

Department of Chemistry, New Arts, Commerce, and Science College, Ahmednagar (Affiliated to SPPU, Pune), Maharashtra, 414001 India
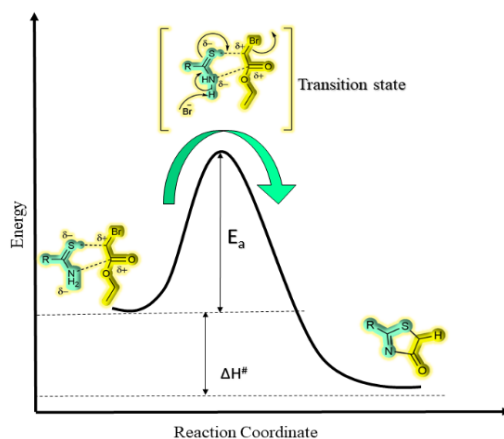
Transition state of the reaction

Substituted thiazolidine is formed from the cyclization reaction of hydrazine carbothioamide, thioacetamide, and thiobenzamide (thioamide) with ethyl 2-bromoacetate, and second-order reaction kinetics for both reactants are exhibited by the reaction, as determined by the Van't Hoff differential method. Thermodynamic parameter Energy of activation (E_a =65.1079 kJ/mol/K, 54.54 kJ/mol/K, 36.87 kJ/mol/K), enthalpy ($\Delta H^{\#}$=60.1195 kJ/mol/K, 49.56 kJ/mol/K, 31.95 kJ/mol/K), entropy ($\Delta S^{\#}$ = -65.862 J/mol), Gibbs' free energy ($\Delta G^{\#}$ = 79.87k J/mol, 76.72 k J/mol, 76.56 k J/mol) and frequency factor ($A = 2.77 \times 10^{+09}$, $1.51 \times 10^{+08}$, $1.12 \times 10^{+05}$) was obtained by pH metric study of the reaction. According to the double-sphere mechanism, the distance between two atoms in solution with ethanol and isopropyl alcohol was calculated.

Keywords: kinetics, order, entropy, Gibbs' free energy, frequency factor, enthalpy.

INTRODUCTION

A link between medicinal chemistry and chemical synthesis is acted upon by thiazolidine structures, which encourage researchers to look at potential new therapeutic agents. The thiazolidine structure, which contains a five-membered heterocyclic ring with nitrogen in the third position and sulfur in the first position, is present. A variety of naturally occurring and biologically active molecules contain it as part of their structure. Its pharmacological aspects are improved by the presence of sulfur, making it useful as a carrier in the synthesis of important chemical combinations. A range of biological applications, such as antioxidant, anticancer, antispasmodic, antibacterial, anti-inflammatory, and neuroprotective effects, have

been demonstrated by it. It is highly valued as an ingredient because of its wide range of biological responses. Many synthetic methods have been applied to increase the selectivity, purity, product yield, and pharmacokinetic activity of thiazolidine and its derivatives, based on literature research. These methods include synthesis methods such as multicomponent reactions, click reactions, nano catalysis, and green chemistry. Reports have been made on the advantages of the green synthesis of thiazolidine and its derivatives, as well as their pharmacological activity [1]. 2-Hydrazinothiazolon-5-one (m.p. = 230°C) was produced under microwave irradiation in a solventless system by the condensation reaction of thiosemicarbazide with chloroacetic acid. A lengthy reaction period and a

---

solvent is required for this reaction under normal heating [2]. Further reports of reactions between ethyl bromoacetate and substituted thiosemicarbazide and 1,1-dimethylsemicarbazides have been observed [3]. Previously, a kinetic study of thiazole formation using 3-chloroacetyl acetone and thioamides was reported by us [4]. The kinetics of 3-chloroacetyl acetone with various thioureas in ethanol has been reported [5]. The kinetics of the reaction between hydrazinecarbothioamide, thioacetamide, and thiobenzamide with ethyl 2-bromoacetate is yet to be investigated.

MATERIALS AND METHODS

Glass-distilled water was used in the investigation. All of the chemicals used in this work, including hydrazinecarbothioamide, thioacetamide, and thiobenzamide with ethyl 2-bromoacetate (Loba), are of analytical quality. A digital pH meter (Model: EQ-614A by Equiptronics) was employed to monitor the pH change as the reaction progresses. Absolute alcohol and glass-distilled water were used in the experiment. A standard solution (Scheme 1) was prepared using pure alcohol as the solvent, along with ethyl 2-bromoacetate and hydrazine carbothioamide, thioacetamide, and thiobenzamide:
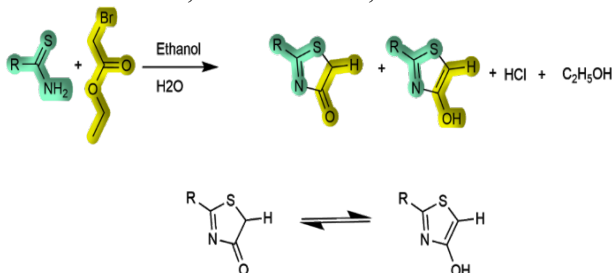
Scheme 1. Reaction scheme

Kinetic measurements were carried out at different concentrations of reactants, temperatures, dielectric constants, and ionic strengths. A solution that contained the appropriate amount of hydrazine carbothioamide, thioacetamide, and thiobenzamide was added to an appropriate solution containing ethyl-2-bromoacetate at the same temperature. The pH meter readings were recorded at a particular time interval. According to the second-order integrated rate law, all the calculations were carried out. Equal amounts of hydrazinecarbothioamide, thioacetamide, and thiobenzamide with ethyl-2-bromoacetate were mixed and kept overnight under similar experimental conditions. Then the reaction mixture was neutralized with $NaHCO_3$ and extracted with diethyl ether. 2-hydrazineylthiazol-4-ol and 2-hydrazineylthiazol-4(5H)-one were characterized as the product, based on their spectral data and reported melting points of 230°C. The product was

104

recrystallized from ethanol and purified using column chromatography with n-hexane and ethyl acetate.

RESULTS AND DISCUSSION

The order n of the reaction [6] involving the following equation was determined using Van't Hoff's differential method (Table 1).

$$n = \frac{log(\frac{dc}{dt})i - log(\frac{dc}{dt})ii}{logCi - logCii} \qquad (1)$$

Table 1. Order concerning both reactant and reagent

Reactant	Reagent	Reactant	Reagent
Hydrazine-carbothioamide	Ethyl 2-bromoacetate	1.17002	0.89022
Thioacetamide	Ethyl 2-bromoacetate	0.967	0.984
Thiobenzamide	Ethyl 2-bromoacetate	0.9745	0.83873

The stoichiometric study indicated that one mole of ethyl 2-bromoacetate reacts with one mole of hydrazinecarbothioamide, thioacetamide, and thiobenzamide. The rates of reaction were measured for different concentrations of hydrazinecarbothioamide, thioacetamide, and thiobenzamide at a constant concentration of ethyl 2-bromoacetate. A straight line was observed on the plot of $log_{10}(dc/dt)$) against log (thioamide) and the slope of the plot was nearly one (Fig. 1).
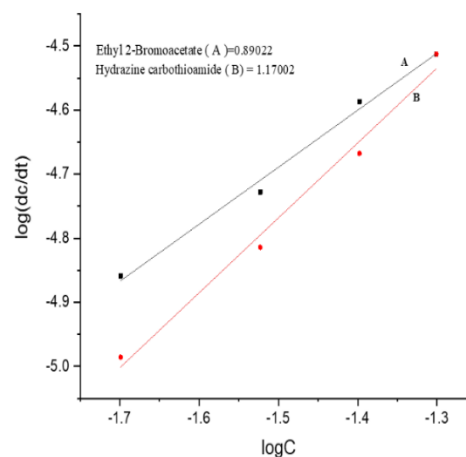
Figure 1. Order graph of hydrazinecarbothio-amide with ethyl 2-bromoacetate.

Similarly, different concentrations of ethyl 2-bromoacetate determined the rates while keeping the concentration of hydrazinecarbothioamide, thioacetamide, and thiobenzamide constant. Van't Hoff's differential method [6] was used to determine the order of reaction concerning ethyl 2-

bromoacetate and hydrazinecarbothioamide, thioacetamide, and thiobenzamide.

The transition-state theory [8] of reactions in solution was first introduced by Wynne-Jones and Eyring [7]. The activation energy for the formation of the product when the molecule crosses the energy barrier was reported by Eyring and Laidler [9]. The Arrhenius equation [10] is applicable to the reactions in solution, and it is contributed to by the activation energy E_a and pre-exponential factor A.

$$k = Ae^{\frac{-Ea}{RT}} \quad (2)$$

Second-order rate constants were determined at five different temperatures. The energy of activation (E_a) was determined according to the Arrhenius relationship by plotting a graph of $\log_{10}k$ against $\frac{1}{T}$ and the thermodynamic parameter like activation energy, pre-exponential factor, activation entropy, and free energy were determined. The negative entropies of activation (ΔS^*) of these reactions indicated the rigid nature of the transition state. With decreasing entropy [11], an activated complex is formed. The negative entropy specifies that the molecules are bound to the solvent, limiting their free movement. Additionally, the negative value of entropies of activation (ΔS^*) indicates that stable cyclic products are formed from less stable noncyclic reactant.

Following equations were used to calculate the thermodynamic parameters (Table 2):

$$Ea = \frac{4.576\, T_1.T_2(\log k_2 - \log k_1)}{T_2 - T_1} \quad (3a)$$

The value of the entropy change of the activated complex can be calculated by equation (3b):

$$k = \frac{RT}{Nh} e^{-Ea^{\#}/RT} * e^{\Delta S^{\#}/R} \quad (3b)$$

But $R/N = k_B$ (k_B=Boltzmann constant)

$$k = \frac{k_B T}{h} e^{-Ea^{\#}/RT} * e^{\Delta S^{\#}/R} \quad (3c)$$

Taking logarithms of both sides and simplifying them gives:

$$\frac{\Delta S^{\#}}{4.576} = \log k - \log \frac{k_B}{h} - \log T + \frac{Ea^{\#}}{4.576T} \quad (3d)$$

$$\Delta H^{\#} = Ea^{\#} - 2RT \quad (4)$$

$$\Delta G^{\#} = \Delta H^{\#} - T\Delta S^{\#} \quad (5)$$

According to equations from the literature, the effect of the salt was investigated, and it was found

that as the ionic strength increased, the rate of reaction was reduced, indicating that the reacting species were oppositely charged [12, 13] (Table 3, Figure 2).

$$I = \frac{1}{2}\sum c_i z_i{}^2 \quad (6)$$

$$\log \frac{k}{k_o} = 1.02 z_A z_B \sqrt{I} \quad (7)$$

In a mixed solvent with variable dielectric constant, Scatchard's equation [14] was employed using the double-sphere model according to electrostatic theory. A straight line is obtained when the logarithm of the rate constant is plotted against the reciprocal of the dielectric constant. The colliding spheres are held together in the liquid phase by the surrounding solvent molecules, and multiple collisions occur before they finally separate, acting as a "cage" [15]. A reaction between uncharged species is resulted due to the development of an activated complex that is more polar than the reactants, and the rate constant rises with increasing dielectric constant [16]. The cyclization reaction between hydrazinecarbothioamide, thioacetamide, and thiobenzamide, and ethyl 2-bromoacetate in ethanol-water and isopropyl alcohol-water system is governed by the double sphere model. (Table 4 and Figure 3).

$$\ln k = \ln k_0 - \frac{z_A z_B e^2}{4\pi\varepsilon\varepsilon_0 d_{AB} kBT} \quad (8)$$

- A rate of two is found for the reaction of ethyl 2-bromoacetate with hydrazinecarbothioamide, thioacetamide, and thiobenzamide.
- The rate of reaction being two is also shown by the suggested rate law.
- The same type of reaction mechanism as the cyclization of thiazole using thioamide and ethyl 2-bromoacetate is indicated by free energy (ΔG^*).
- Cyclic compounds are formed from open-chain compounds when there is a decrease in entropy (ΔS^*).
- The formation of nucleophiles and electrophiles in this reaction is indicated by the salt effect.
- Bimolecular reactions in the liquid phase of hydrazinecarbothioamide, thioacetamide, and thiobenzamide with ethyl 2-bromoacetate in an ethanol-water system and isopropyl alcohol-water system apply the double sphere model.

Expected reaction mechanism
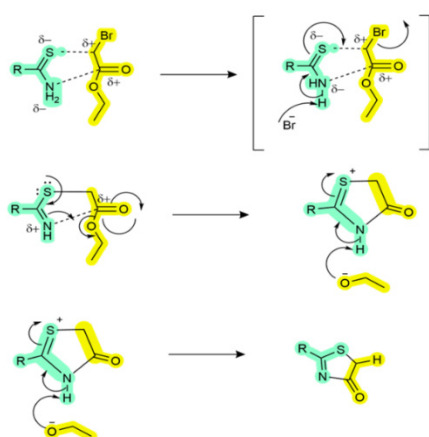
S$_1$ - ethyl 2-bromoacetate
S$_2$ - thioacetamide or thiobenzamide

$$\text{Rate} = k_1[S_1][S_2] - k_{-1}[\text{Intermediate}]$$

On applying steady state approximation:

$$\frac{d}{dt}[\text{intermediate}] = 0$$

$$= k_1[S_1][S_2] - k_{-1}[\text{Intermediate}]$$

$$- k_2[\text{Intermediate}]$$

$$[\text{Intermediate}] = \frac{k_1[S_1][S_2]}{k_{-1} + k_2}$$

Substituting the value of [Intermediate] in equation:

$$\text{Rate} = k_1[S_1][S_2] - \frac{k_{-1}.k_1[S_1][S_2]}{k_{-1} + k_2}$$

Scheme 2. *Proposed general mechanism and rate expression*

$$\text{Rate} = \left\{ k_{-1} - \frac{k_{-1}.k_1}{k_{-1} + k_2} \right\}[S_1][S_2]$$

Table 2. Thermodynamic parameters for the reaction of hydrazinecarbothioamide, thioacetamide, and thiobenzamide with ethyl 2-bromoacetate. (T =300K)

	A	E_a^* kJmol^{-1}	ΔH^* kJmol^{-1}	ΔS^* Jmol^{-1}	ΔG^* kJmol^{-1}
Hydrazinecarbothioamide	2.77× 10^{+09}	65.10	60.11	-65.86	79.87
Thioacetamide	1.51× 10^{+08}	54.54	49.56	-90.53	76.72
Thiobenzamide	1.12× 10^{+05}	36.87	31.95	-148.70	76.56

Table 3. Slope values for the salt effect for the graph of logk *versus* √μ

Reactant	Reagent	NaCl	LiCl
Hydrazinecarbothioamide	Ethyl 2-bromoacetate	-1.86125	-1.10995
Thioacetamide	Ethyl 2-bromoacetate	-0.44068	-0.46639
Thiobenzamide	Ethyl 2-bromoacetate	-0.25668	-0.31841
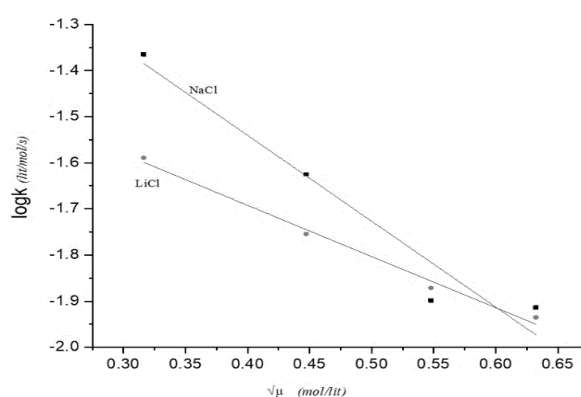
Figure 2. NaCl and LiCl effect on hydrazinecarbothioamide with ethyl 2-bromoacetate

Table 4. Solvent effect water-ethanol and water-isopropyl alcohol and d$_{ab}$ values

Reactant	Reagent	d$_{AB}$ = Ethanol (pm)	d$_{AB}$ = Isopropyl alcohol (pm)
Hydrazinecarbothioamide	Ethyl 2-bromoacetate	2.31 × 10^{+03}	2.79 × 10^{+03}
Thioacetamide	Ethyl 2-bromoacetate	3.86 × 10^{+03}	3.10 × 10^{+03}
Thiobenzamide	Ethyl 2-bromoacetate	1.60 × 10^{+04}	1.11 × 10^{+04}
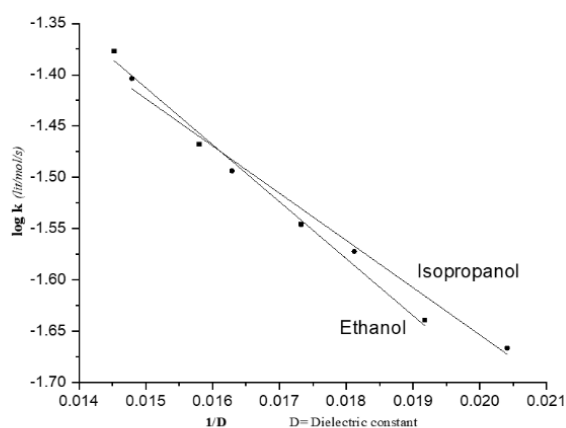
Figure 3. Solvent effect on hydrazinecarbothioamide with ethyl 2-bromoacetate

REFERENCES

1. N. Sahiba, A. Sethiya, J. Soni, D. K. Agarwal, S. Agarwal, Saturated five-membered thiazolidines and their derivatives: from synthesis to biological applications, **378** (2), Springer International Publishing, 2020. doi: 10.1007/s41061-020-0298-4.
2. M. M. Heravi, N. Nami, H. A. Oskooie, R. Hekmatshoar, *Phosphorus Sulfur Silicon Relat. Elem.*, **181** (1), 87 (2006), doi: 10.1080/104265090968992.
3. J. H. Cooley, S. Sarker, A. Vij, *Journal of Organic Chemistry*, **60** (5), 1464 (1995), doi: 10.1021/jo00110a058.
4. P. S. Sadavarte, B. H. Zaware, S. J. Takate, *Oriental Journal of Chemistry*, **38 (**4), 1031 (2022).
5. B. H. Zaware, S. R. Kuchekar, *Bulg. Chem. Commun.*, **46** (1), 180 (2014).
6. M. J. H. V. Hoff, Etudes de dynamique chimique, Amsterdam, Frederik Muller & Co, 1884, p. 333.
7. W. F. K. Wynne-Jones, H. Eyeing, *J. Chem. Phys.*, **3**, 492 (1935), doi: 10.1063/1.1749713.
8. K. J. Laidler, M. C. King, *Journal of Physical Chemistry*, **87** (15), 2657 (1983), doi: 10.1021/j100238a002.
9. K. J. Laidler, H. Eyring, *Ann. N. Y. Acad. Sci*, **39** (1), 303 (1939), doi: 10.1111/j.1749-6632.1939.tb55380.x.
10. S. Arrhenius, *Z. physik. Chem.*, **4** (2), 226 (1889).
11. S. Glasstone, *J. Chem. Soc.*, 723 (1936).
12. E. P. Debye, E. Hückel, *Phys. Z.*, **24**, 185 (1923).
13. V. K. La Mer, *J. Franklin Inst.*, **225** (6), 709 (1938), doi: 10.1016/s0016-0032(38)90929-9.
14. G. Scatchard, *Chem. Rev.*, **10** (1), 229 (1932), doi: 10.1021/cr60035a012.
15. E. Rabinowitch, *Trans. Faraday Soc.*, **33** (0), 1225 (1937), doi: 10.1039/TF9373301225.
16. J. G. Kirkwood, *J Chem Phys*, **2** (7), 351 (1934), doi: 10.1063/1.1749489.

Sustainable practices in contemporary livestock farming

E. N. Paunova-Hubenova*, E. D. Trichkova-Kashamova

Institute of Information and Communication Technologies, Bulgarian Academy of Sciences, Sofia 1113, Bulgaria

In recent years, the consumption of dairy and meat products increases worldwide. Alongside this trend, the environmental impact of livestock farms is also increasing. The main problems can be grouped as follows: energy consumption, release of greenhouse gases, clearwater consumption, and discharge of contaminated water. In an effort to reduce the impact of livestock farms, scientists from various fields are developing different solutions to the problems mentioned above. These solutions are highly interconnected, as the output products of one activity often are the input of another. This paper aims to present an analytical overview of the various existing and implemented solutions which help to increase energy independence and create zero-waste dairy production. The provided sustainable practices include: methods for lowering the GHG emissions, approaches for separation and purification of livestock farm waste, biogas producing by anaerobical digestion of organic waste, methods for filtration and purification of waste water. In addition to the ecological effects, the implementation of these practices brings economic profits for livestock farms. The economic efficiency, ecological, and social optimization functions are described.

Keywords: zero-waste production, environmental protection, economic efficiency, livestock farms, risk management.

INTRODUCTION

The increase in dairy and meat products consumption in the last decades leads to the creation of bigger livestock farms. In many cases, the growth of this industry causes significant ecological problems. The managers can weaken the impact on the environment by applying one or more methods for energy independence and zero-waste production of the farm. This paper aims to present an overview of a number of solutions to the environment issues.

By using these practices, the farm managers can also increase economic efficiency, as the consumable expenses decrease and, in some cases, the surplus biogas or energy can be sold to other consumers. Farm management must comply with the parameters of the enterprise when choosing the appropriate solutions to achieve maximum efficiency. It is recommended that processes be modeled in advance to optimize inputs, farm profits, and environmental impact [1, 2].

To deeply understand the environmental issues caused by livestock farms and the practices solving (or mitigating) them, we prepared the present short review. Hence, we conducted our investigation having in mind the following research questions:

RQ 1. What are the most applicable and effective solutions to the environmental problems caused by livestock farms?

RQ 2. What are the economic and social effects of the applied solutions, and how can they be optimized?

Structure of the paper

The second part briefly describes the methodology of the conducted research. The next section presents some practices for lowering the GHG emissions. Then, the applicable methods and process phases for separating of waste are provided. The fifth section explains the implementation of anaerobical digestion of organic waste for biogas production. The most popular approaches for filtration and purification of wastewater are presented in the next section. Optimization according to one of the researched criteria (economic, ecological, or social efficiency) is provided in the seventh section. The paper ends with a brief discussion on the presented solutions regarding the research questions and a conclusion.

Methodology

The literature review was conducted in two steps. Firstly, researchers looked for information about the main environmental problems caused by livestock farms. Some of the searched keywords were "livestock farms" or "dairy farms", combined with "environmental issues" or "ecological problems". According to literature sources [3, 4], the most significant are the following issues:

- Release of greenhouse gases, mainly methane, and CO_2, into the atmosphere;
- Energy consumption;
- Clearwater consumption;
- Discharge of contaminated water (effluent) into the environment.

---

* To whom all correspondence should be sent:
E-mail: elena.paunova@iict.bas.bg

In the second step, the authors searched for scientific publications on implementing effective solutions for the above-mentioned environmental issues. The authors used as keywords some of those found in the first step, such as "zero-waste production", "environmental protection", "greenhouse gases", "water purification", "economic efficiency", "risk management", and "waste management". The most significant results from the investigation of the selected papers are provided in the next sections.

Greenhouse gases management

One of the major environmental issues of livestock farms is the release of greenhouse gases (GHG) like methane and CO_2 into the atmosphere, which cause global warming. Some of the applied solutions include introducing appropriate feed additives for animals, processing waste (solid and liquid), obtaining [4] and using biofuels, fertilizers, etc. Figure 1 presents a list of activities that increase or decrease the GHG emissions from the farms.

To lower greenhouse gas emissions, livestock farms implement a variety of strategies that include solutions such as changes in feeding, husbandry, and management practices. These changes have an impact on animal health and welfare and should be studied in detail [5].
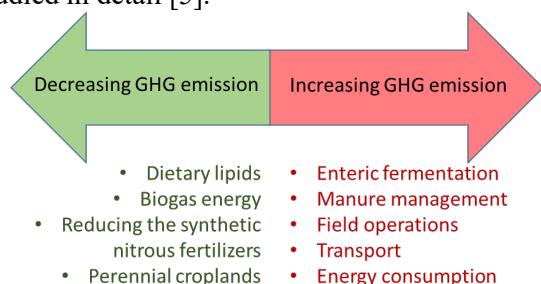
Fig. 1. Greenhouse gas emission in dairy farms [4]

Direct strategies to reduce greenhouse gas emissions (CH_4 and N_2O) from farmyard manure can be classified as reducing rumen methanogenesis, which can be divided into reducing total emissions and reducing emission intensity without directly targeting methanogenesis [6].

Supplementing with antimethanogenic drugs (such as antibiotics that lower methanogen populations) or electron (H^+) acceptors are two methods for lowering methanogenesis [5]. The natural function of the rumen is disrupted by these tactics, which are effective in lowering CH_4 emissions, and their improper use may result in rumen diseases, as well as possible health and welfare issues. The second set of solutions focuses on improving production efficiency to lower GHG emissions while maintaining current levels of

production, and it is designed for both ruminants and monogastric. Prominent tactics from this group include boosting feed efficiency or enhancing the herd's health, which operates as profitable tactics by simultaneously enhancing the environment's viability, economic return, or animal welfare as appropriate [5, 7].

Waste management

The livestock farms produce a huge amount of solid waste containing animals' manure, hair, and plant pieces from food or bedding. This matter should be separated according to the particle size and processed further.

The division of the solid matter of animal manure into fractions that can be removed by the main categories of separator or separation process is presented in Table 1.

Table 1. Division of the solid matter of animal manure into fractions [8]

Size, μm	Pollutant
More than 5000	Fibre
Up to 5000	Coarse solids
Up to 1000	Fine solids
Up to 20	Colloidal particles
Up to 1	Dissolved solids

Some of the main problems with biogas slurry are: low concentration, high production volume, and content of very low-molecular-weight (small-molecule) organic pollutants. The risk of groundwater contamination with these low-molecular organic pollutants increases during the process of enrichment (fertigation) of the biogas suspension [9]. The biogas slurry is put through a number of biotechnology processes that have to be modeled to optimize their parameters [10].

Animal hairs, bedding, and larger particles that make up the solid material provide fibrous material from animal manures with a characteristic texture. Following a screening procedure, it can be removed using a variety of separators since the solid material is retained as the slurry passes through a screen [8]. Due in part to the fibrous structure of a lot of the removed material, a fraction of particles that are smaller than the hole size can also be retained. The size of the holes can range from 1 to 5 mm or bigger. However, smaller screens are employed to keep more of the suspended materials [11].

When employed alone, particles with an effective size of about 1 mm are the cut-off for separators. Yet, the concept of particle size is ambiguous due to the physical properties of the fibre. More open screens are frequently required for cow slurries containing significant amounts of straw and associated material

in order to ensure adequate separator performance. Particles larger than the size of 5 mm can be defined as a coarse fibre fraction [8].

The applicable technique for particles smaller than 1 mm is based on a sedimentation principle, either by gravity or rapid sedimentation in centrifuges. The settling procedures frequently follow a biological treatment because raw slurry contains several naturally occurring but biodegradable organic surfactants that can prevent flocculation and settling. The separation process depends on the larger density of suspended particles than that of water. However, for animal slurries, this difference is negligible [12]. A preliminary screening procedure can be applied to eliminate the lighter fibrous debris.

Sedimentation processes have a substantial impact on bacteria elimination because they frequently form flocs that are joined to larger particles. This effect can be enhanced by adding flocculants, which also make it possible to remove additional colloidal material using the same technique. The process can be hastened by increasing the temperature, but usually to the same result [8].

Processing for the sludge phase consists of thickening or drying options, with the separated water going back into the feed stream. Filtration may be taken into account for the liquid phase if the amount of suspended materials is small. Due to the creation of a filter cake, which is aided by adding a filter aid like fine sand to the input stream, the retained particle size is likely to be lower than the pore size. A significant portion of the colloidal material may also be removed by filtration, leaving a largely cleared effluent in its place [13]. The impact on the much smaller virus particles will be significantly reduced, but there is no assurance that all bacteria will be eliminated.

The sole separation option for removing the smallest particles and the dissolved stuff itself is based on membranes. Again, filtering is the basic concept, but "crossflow" is frequently the arrangement. This fact suggests that wastewater is forced through the membrane under pressure, squeezing out the clear water (permeate) and leaving a concentrated stream in its place. Only dilute effluents are suitable for such a treatment [8].

Energy management

The energy is needed for various activities that take place on the dairy farm (Figure 2), e.g., milk heating or cooling, keeping the temperature within certain limits, supplying robotic systems, etc.

The author of [3] proposes the following solutions to these issues:

- reducing the volume of milk by condensation;
- using energy produced from farm waste products;
- implementing renewable energy sources such as solar panels.
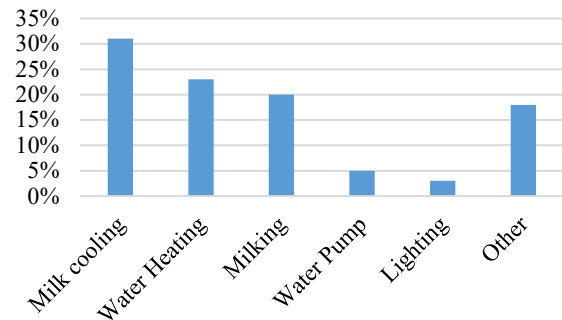
Fig. 2. Energy consumption in dairy farms [3]

Organic waste materials can be processed into useful substances through the application of anaerobic digestion (AD) [14, 15]. AD is a biological process of breaking down organic material in an anoxic environment. In this way, different types of waste can be processed, for example, animal manure, ~~and~~ plant, and industrial waste, and as a result, methane is released [16, 17].

Various models are applied to describe biogas production, most of which are mechanistic and empirical [18, 19]. The main difference between both types of models is their focus. Empirical models are based on mathematical equations to describe the stochastic relationships of various factors and parameters, as well as using real measured process data [20, 21], and mechanistic models focus more on the biological, chemical, and physical laws that relate to the production of biogas. Anaerobic digestion model no. 1 (ADM1) is used mainly for the second option, and it is a dynamic model that includes four stages of anaerobic digestion [22]. ADM1 is a biochemical process in which organic matter is broken down into carbohydrates, lipids, proteins, and inert compounds [19].

A large number of studies have applied an empirical model to predict the rate of biogas production. To investigate the methane production in the anaerobic digestion of swine wastewater, Deng *et al*. [23] use such a mathematical model (Deng model). The purpose of their study is to reveal the impact of organic loading rate (OLR) on methane production. According to their results, the developed model correctly reflects the influence of OLR on the methane production rate. Yang *et al*. [24] modified

the Deng model for methane production. The two models are represented by equations (1) and (2):

Deng model [23]:

$$R_p = \frac{R_{p\max}}{1+e^{(K_{LR}-L_r)}} \qquad (1)$$

Modified Deng model [24]:

$$R_p = \frac{R_{p\max}}{1+e^{K_D(K_{LR}-L_r)}} \quad , \qquad (2)$$

where R_p is the volumetric biogas production rate ($L\ L^{-1}\ d^{-1}$); $R_{p\max}$ is the maximum volumetric biogas production rate ($L\ L^{-1}\ d^{-1}$); L_r is the OLR ($g\ TS\ L^{-1}\ d^{-1}$). K_{LR} is the half-saturation constant ($g\ TS\ L^{-1}\ d^{-1}$), and equals the OLR at one half of the $R_{p\max}$. The index (K_D) denotes the speed of the volumetric methane production rate approaching the maximum as a function of temperature.

Water management

In recent years, two issues related to water management in livestock farms affect the environment:

- *Clearwater consumption.* The consumption of large quantities of drinking water is determined by activities related to the consumption of water by the animals, as well as the cleaning of udders before milking and of premises and milking crates.
- *Discharge of contaminated water* (effluent) into the environment. Many different chemicals are used in livestock farming, which, once processed, are discharged into rivers or lakes, polluting them. Water pollution can be divided into several categories depending on the type of pollutant:

  o inorganic (minerals, antibiotics, heavy metals, chemicals and other toxic substances);

  o organic (feces and waste of vegetable and animal origin, oils, lubricants and other petroleum products used by robots and machines in farms);

  o microbiological (pathogenic bacteria, viruses, some fungi, and parasitic worms).

The solution for both problems can be described in short as reducing the use of clean water by purifying and reusing contaminated water. There are many different methods of water purification, and the choice of one or a combination of them depends on the type of contaminant, degree of contamination, and potential harm. The purification methods and their application are presented in Table 2.

The authors of [25] apply UV disinfection and a 7-stage system with reverse osmosis for the purification of tap water and spring water, implemented in the form of a cascade system.

The reverse osmosis is increasingly used to improve the quality of purified drinking water. This method, however, is not directly applied to fresh water due to the possibility of membrane fouling [33] but is combined with other purification methods.

The authors of [34] propose a short classification of the methods of dairy wastewater treatment, which are mainly divided into biological, natural, physical, and chemical methods (Figure 3).

Table 2. Purification methods and their application

Method	Application	Ref.
Physical purification (mechanical, primary)	coarse substances separation	[25]
Physico-chemical purification	finely suspended particles in water	[25]
Chemical purification	pH adjustment and removal of some solutes	[26]
Biological (secondary) purification	conversion of biological substances from wastewater into biomass	[26]
Filtration	removal of suspended, colloidal and dissolved contaminants	[25]
Disinfection	pathogenic bacteria removal	[26]
Three-layer filter, representing ionosorption column	eliminates highly toxic concentrations of arsenic and chromium from water	[27, 28]
Ion exchange and reverse osmosis	for reducing nitrates in the waters	[29]
Filtration by reverse osmosis, distillation filtration, activated carbon filter for defluorination of aluminum	reducing the content of fluorides in drinking water	[25]
Chlorine compounds	disinfection of water and pipelines	[30, 31]
Microorganisms and the process is accompanied by the consumption of dissolved oxygen in the water	the organic matter is decomposed	[32]

One of the new and promising technologies for wastewater treatment is the separation through membranes, in which organic substances are segregated [35, 36]. This method is based on a pressure difference on both sides of the membrane,

which is used as a driving force to separate the different components in the wastewater [37].

In the management of waste manure from pig farms in populated areas and the efficient use of resources, pretreatment by sand filtration (SF) and ultrafiltration (UF) can be applied. Through ultrafiltration and optimization of the pretreatment process for fractionation of biogas suspension, the removal of part of the solid suspended substances and reduction of membrane clogging is achieved.
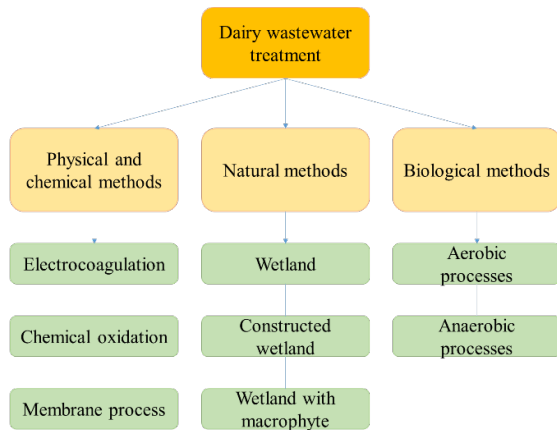
Fig. 3. Methods for dairy wastewater treatment [34]

According to the authors of [37], good ultrafiltration performance can be achieved by prefiltration through a sand column with parameters 100 kDa membrane, and 0.10 MPa transmembrane pressure. Reduction of membrane fouling and improvement of ultrafiltration efficiency is achieved with the reflux of permeate. Their experiments show a higher concentration of organic matter in the effluent without UF compared to those with permeate biochemical treatment. These results clearly show that the UF pretreatment process is suitable to be applied to the treatment of livestock farm wastewater.

Another way to treat wastewater from livestock farms is the Fenton process. The optimal conditions for removing sCOD (dissolved chemical oxygen demand) by this method are described in [38]. Integrating the process with other wastewater treatment methods can increase its potential. For example, after biofiltration, about 91% of sCOD can be removed, and coagulation removes 86% of sCOD [38]. A significant solids load is present in this type of wastewater. Therefore, the application of coagulation before the Fenton process is necessary. The Fenton process does not require complex equipment or hazardous reagents, making it simple and effective.

Optimization of economic, environmental, and social criteria

The optimization can be performed according to one of the following three criteria (Figure 4): economic, ecological, and social efficiency [39]. This section presents the three optimization functions.

The economic efficiency function includes the annual costs associated with the collection of waste mass from animal farms, its transportation, storage, and transformation, and storage of the resulting substances. It also includes the investment costs for the construction of waste processing facilities [40]. This function is defined by equation (3) aiming at its minimization:

Fig. 4. Sustainable development and management concept of Integrated Biogas Supply Chain [39]

$$COST = \sum_{t \in T}(LT_t TDC_t), \qquad (3)$$

where TDC_t is total costs of Integrated Biogas Supply Chain (IBSC) per year, [$ y^{-1}].

The price of the utilized biogas can also be used as a target function. This suggestion is valid for the whole time interval, provided that the regions' needs for this energy carrier are met.

$$COST_{TBG} = \sum_{t \in T}(LT_t TBG_t), \qquad (4)$$

where TBG_t is the total value of biogas used by the regions [$/y].

The criterion that is minimized in ecological optimization is Eco-Indicator 99 [41], which is a standardised approach to evaluating a process, a product, or an activity's global impact. This method can be implemented both in combination with an optimization model and as a standalone tool. The Eco-Indicator 99 which measures the environmental impact of all network operations in terms of the quantity of carbon dioxide equivalent produced over

the course of the goods' lifetimes, is used in the proposed environmental impact model.

$$ENV = \sum_{t \in T}(LT_t TEI_t), \qquad (5)$$

where TEI_t is overall environmental impact of IBSC $[kg_{CO_2 eq}.d^{-1}]$.

Environmental assessments are presented as environmental costs with a monetary equivalent of the environmental impact [40], which is determined by a global warming factor according to formula (6):

$$Cost_{ENV} = C_{CO_2} ENV, \qquad (6)$$

where $Cost_{ENV}$, $[\$ \, y^{-1}]$ are the environmental costs that should be paid, and C_{CO_2} is the coefficient of global warming $[\$/kg_{CO_2 eq}.]$, which most commonly used value is 0.135 $\$/kg_{CO_2 eq}$ [42].

Social Objective Function: Job creation is used as the social criterion, which includes: manufacturing jobs (direct), new contractor jobs (indirect), and new employees in local services (induced). Next, depending on reliance, the social impact in terms of employment generation is calculated (7).

$$JOB = \sum_{t \in T}(LT_t Job_t), \qquad (7)$$

where Job_t is the expected total number of jobs created.

According to [40], finding the values of the below presented decision variables is the problem solution, where the optimization criterion has a minimum value, is the goal of optimization:

- The number, size and location of bioreactors represent the structure of the Supply Chains network.
- Identification of the locations of livestock farms and the waste processing facilities.
- Flows of the transferred farm waste and biogas across the locations.
- Type and amount of the delivery transport for each connection.
- Quantity of GHG emissions produced at each step of the biogas deriving.

The optimization criteria can be divided into economic ($COST$ or $COST_{TBG}$) (3, 4), environmental (ENV or $Cost_{ENV}$) (5, 6) and social (7), looking for sustainability in:

- Minimizing the supply chain's overall logistics costs while accounting for fixed and variable expenses [\$].
- Minimizing the total quantity of GHG emissions, measured in [kg or \$] of carbon dioxide equivalent emissions $[kg_{CO_2 eq}.]$.
- Calculating the necessary workforce to ensure the sustained implementation of the IBSC's activities [Number of Jobs].

According to mixed integer linear programming [39], the optimization problem for the IBSC design is with a single aim, either environmental, social, or economic, with the remainder being treated as constraints. The supply chain's strategic design incorporates two layers of decision-making: those regarding the construction of the chain's superstructure and those regarding the allocation of farm waste and biogas flows among various locations.

Minimizing the GHG emissions $[kg_{CO_2 eq}./\text{d}]$: The goal is to reduce the total annual equivalent GHG emissions caused by the IBSC operation when the optimization problems involve an environmental criterion. This objective function's formulation is based on the overall GHG emissions from the supply chain and other fuels, which are evaluated using the Life Cycle Assessment approach, where emissions are added to each stage of the life cycle.

Minimizing the total annual costs, [\$/y]: The goal is to reduce the total annual costs when an economic criterion is present in the optimization problem. These latter costs comprise the annual totals for capital expenditures, operating expenses, government subsidies, and CO_2 emission costs [39].

Risk management

In addition to optimizing the activities in the livestock farms in terms of environmental, economic and social criteria, it is also necessary to implement economic risk management. The main types of risks, methods of their assessment and an algorithm for their reduction are presented below.

Economic risk for livestock farms is difficult to assess and manage due to multiple uncertainties [43]. Baquet et al. [44] defined five main types of risks related to production, marketing, credit, environment, and personal risk, respectively. Later, Hardaker [45] adds policy-related risk.

There are different methods for risk assessment in agriculture, e.g., "What if?", "Fuzzy matrix", "Scenario analysis", "Cost-benefit analysis" [43], etc.

Boneva and Vatchova [46] outlined the five steps in risk management (Figure 5):

```
┌─────────────────────┐
│  Identify possible  │
│  sources of risk    │
└─────────────────────┘
          │
          ▼
┌─────────────────────┐
│     Identify        │
│     outcomes        │
└─────────────────────┘
          │
          ▼
┌─────────────────────┐
│ Clarity on alternative │
│     strategies      │
└─────────────────────┘
          │
          ▼
┌─────────────────────┐
│     Evaluate        │
│   consequences      │
│    or outcomes      │
└─────────────────────┘
          │
          ▼
┌─────────────────────┐
│ Evaluate the trade-off │
│  between the cost of   │
│   risk and benefits    │
└─────────────────────┘
```
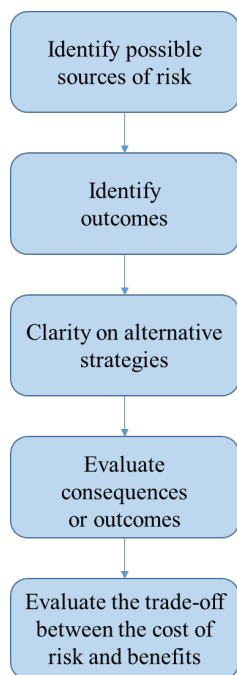
Fig. 5. Steps in risk management

Identify possible sources of risk;

- Identify outcomes that may occur (timing or cost changes);
- Clarity on alternative strategies (change in production plan or new technology);
- Evaluate consequences or outcomes for each possible outcome for each strategy;
- Evaluate the trade-off between the cost of risk and benefits.

Schilling [47] proposes an algorithm for risk reduction that includes the following four steps:

1. Planning and identification of risk-related information (documentation, internal and external circumstances).
2. During the implementation phase, approaches are sought to reduce risk influences.
3. Risk control includes validation, assessment, and search for adequate risk assessment methods.
4. Implement actions related to the improvement and correction of circumstances associated with increased risk.

DISCUSSION AND CONCLUSION

A brief discussion on the findings from this research is provided below with respect to our research questions:

RQ 1. What are the most applicable and effective solutions to the environmental problems caused by livestock farms?

For each of the above-mentioned environmental problems caused by livestock farms, there are

number of solutions. In most cases, the choice of a set of such solutions should be made after thorough research and planning of various aspects such as farm size, number and type of animals kept, long-term goals, and available resources. All the processes that make up such a solution must also be taken into account, since often the output materials from one process are input to another.

RQ 2. What are the economic and social effects of the applied solutions, and how can they be optimized?

Some of the solutions discussed in the article bring economic benefits to the farms that apply them. In order to expand their application, it is necessary to inform farm management about their benefits, as well as support in their implementation by stakeholders.

Other solutions, such as the treatment and reuse of wastewater, are not economically justified but are necessary from the point of view of reducing the impact of livestock farms on the environment. For their wider application, a change in the normative documents and monitoring their compliance is necessary.

The steps to manage risks, as well as an algorithm for their reduction, are presented. Depending on the risk type, different decisions can be made, some of which include choosing less risky technologies, diversification of key suppliers, risk-sharing strategies (including insurance), etc.

The presented sustainable practices would lead to a number of positive effects such as:

- environmental protection;
- zero-waste production;
- energy independence;
- economic efficiency.

Within the assessment of the solutions proposed, the key address ought to be what the goals of the broader farm strategy are. This is often a pivotal beginning point because it will shape the methodology that in turn will empower the choice of the cheapest innovation that's moreover effective.

REFERENCES

1. P. Popova-Krumova, Chr. Boyadjiev, Modeling and Simulation in Chemical Engineering, Project Reports on Process Simulation, Chr. Boyadjiev (ed.), Springer International Publishing, Book Series: Heat and Mass Transfer, 2022, p. 147.

a

2. P. Popova, Chr. Boyadjiev, *Biochemical Engineering Journal*, **39**, 397 (2008).

3. J. Upton, Reducing energy costs on dairy farms (2021). Available online: https://www.teagasc.ie/news-events/daily/dairy/reducing-energy-costs-on-dairy-farms.php (accessed on 28 Feb 2023).

4. V. Antonova, *RUDN University*, (2021). Available online: https://www.eurekalert.org/news-releases/587486 (accessed on 28 Feb 2023).

5. P. Llonch, M. J. Haskell, R. J. Dewhurst, S. P. Turner. *Animal*, **11** (2), 274 (2017).

6. A. Hristov, J. Oh, F. Giallongo, T. Frederick, M. Harper, H. Weeks, A. Branco, P. Moate, M. Deighton, S. Williams, M. Kindermann, S. Duval. *Proceedings of the National Academy of Sciences,* **112**, 10663 (2015).

7. S. Dimitrov, K. Pavlova, *Proceedings of the International Conference "Applications of Mathematics in Engineering and Economics" (AMEE)*. In press (2022).

8. C. H. Burton, *Livestock Science*, **112**, 208 (2007).

9. W. Zeng, J. Qiu, D. Wang, Z. Wu, L. He, *Science of the Total Environment,* **810,** 151294 (2022).

10. Chr. Boyadjiev, P. Popova-Krumova, Progress in Chemical Science Research, **2**, B P International, 2022, p. 1

11. S. Dimitrov, K. Pavlova, *Proceedings of 8th International Conference on Energy Efficiency and Agricultural Engineering (EE&AE)* In press (2022).

12. V. Mitev. *Finance: Theory and Practice,* **26** (6),166 (2022).

13. V. Mitev, *Journal of UMG „St. Ivan Rilski",* **62**, part. IV, Publishing House „St. Ivan Rilski", Sofia, 2019, p. 37.

14. C. Manjusha, B. Sajeena, *Procedia Technol.,* **24**, 654 (2016).

15. L. Kabaivanova, P. Petrova, V. Hubenov, I. Simeonov, *Life*, **12**, 702. (2022).

16. B. K. Ahring, Biomethanation; Springer: Berlin/ Heidelberg, Germany, 2003.

17. D. Deublein, A. Steinhauser, WileyVCH Verlag GmbH & Co, KGaA: Weinheim, Germany, 2003.

18. A.M. Enitan, J. Adeyemo, F.M. Swalaha, S. Kumari, F.Bux, *Rev. Chem. Eng*., **33**, 309 (2017).

19. J. Lauwers, L. Appels, I.P. Thompson, J. Degreve, J. F. van Impe, R. Dewil, *Progress. Energy Combust. Sci.,* **39**, 383 (2013).

20. S. Theuerl, C. Herrmann, M. Heiermann, P. Grundmann, N. Landwehr, U. Kreidenweis, A. Prochnow, *Energy Rev.,* **12**, 396 (2019).

21. V. Hubenov, J. Miteva-Staleva, R. Eneva, N. Boteva, L. Kabaivanova, *Ecological Engineering and Environment Protection*, **3**, 35 (2021).

22. K. Obileke, S. Mamphweli, E. L. Meyer, G. Makaka, N. Nwokolo, *Processes*, **9**, 643 (2021).

23. L. Deng, H. Yang, G. Liu, Y. Lei, *Appl. Energy,* **134**, 349 (2014).

24. H. Yang, L. Deng, G. Liu, D. Yang, Y. Liu, Z. Chen, *Water Resour.,* **102**, 464 **(**2016).

25. M. Stoev, N. Ivanova, E. Chorbadzhiyska, *Bulgarian Chemical Communications*, **54**, Special Issue B2, 52 (2022)**.**

26. J. Chervenkova, *University of Agribusiness and Rural Development Edition*, ISSN 1314-5703. *2* (2), 2013.

27. V. Campos, J. I. Sayeg, P. M. Buchler, *Communications in Soil Science and Plant Analysis*. **39** (11 &12), 1670 (2008).

28. Chr. Boyadjiev, M. Doichinova, B. Boyadjiev, & P. Popova-Krumova, Modeling of Column Apparatus Processes*,* Springer-Verlag, Berlin Heidelberg, 2016, p. 313.

29. Executive Environment Agency, Quality of drinking water, National report on the state and protection of the environment in the Republic of Bulgaria, 2014. Available online: http://eea.government.bg/bg/soer/2014/water/ kachestvo-na-piteynite-vodi (accessed on 28 Feb 2023). (in Bulgarian).

30. D. Uzun, E. Razkazova-Velkova, K. Petrov, V. Beschkov, *Bulgarian Chemical Communications* **47**(3), 859 (2015).

31. D. Uzun, E. Razkazova-Velkova, V. Beschkov, K. Petrov, *International Journal of Electrochemistry*, 7628761 (2016)

32. J. Wanga, S. Zhanga, H. Caoa, J. Maa, L. Huanga, S.Yub, X. Maa, G. Songc, M. Qiud, X. Wanga, *Journal of Cleaner Production*, **331**, 130023 (2022).

33. E. R. Cornelissen, D. J. H. Harmsen, B. Blankert, L. P. Wessels, W. G. J. van der Meer, *Desalination*, **509**, 115056 (2021).

34. P. Das, K. K. Paul, *Research Square* (2022). Available online: https://assets.researchsquare.com/files/rs-1774888/v1/db3827b0-52b9-44cf-aac4-1397d8016c98.pdf?c=1661954390 (accessed on 28 Feb 2023).

35. S. Hube, M. Eskafi, K. F. Hrafnkelsdottir, B. Bjarnadottir, M.A. Bjarnadottir, S. Axelsdottir, B. Wu, *Sci. Total Environ*., **710**, 136375 (2020).

36. H. Luo, T. Lyu, A. Muhmood, Y. Xue, H. Wu, E. Meers, R. Dong, S. Wu, *Chem. Eng. J.* **352**, 855 (2018).

37. W. Zeng, R. Lu, D. Wang, L. He, Zh. Wu, *Journal of Water Process Engineering,* **48**, 102859 (2022).

38. E. Domingues, E. Fernandes, J. Gomes, R. C. Martins, *Journal of Cleaner Production,* **293,** 126105 (2021).

39. E. Ganev, V. Beschkov, *Bulgarian Chemical Communications*, **54,** 3, 205 (2022).

40. E. Ganev, B. Ivanov, N. Vaklieva-Bancheva, E. Kirilova, Y. Dzhelil, *Energies*, **14,** 2261 (2021).

41. S. Hansen, S. Olsen, Z. Ujang, *Bioresour. Technol*., **104**, 358 (2012).

42. The Eco-indicator 99A damage oriented method for Life Cycle Impact Assessment, *Methodology Annex* (2001). Available online: https://www.presustainability.com/download/EI99_annexe_v3.pdf (accessed on 28 Feb 2023).

43. B. Vatchova, Y. Boneva, *Proceedings of International Conference "Robotics, Automation and*

Mechtronics'21, 25-27 October, Velingrad, Bulgaria, 2021, p. 23.

44. A. Baquet, R. Hambleton, D. Jose. Washington: USDA, Chapter 3, 1997.
45. J. Hardaker, R. Huirne, J. Anderson, G. Lien, Wallingfort: CABI Publishing, Chapter 1, 2004.
46. Y. Boneva, B. Vatchova, *Proceedings of International Conference "Robotics, Automation and*

Mechtronics'21", 25-27 October, Velingrad, Bulgaria, 2021, p. 27.

47. B. Schilling, Extension Training to Support Agritourism Development in the Northeast. https://nationalaglawcenter.org/research-by-topic/agritourism-2/.

Precision livestock farming as a useful tool to reduce environmental impact of the farms

E. D. Trichkova-Kashamova*, E. N. Paunova-Hubenova

Institute of Information and Communication Technologies, Bulgarian Academy of Sciences, Sofia, Bulgaria

The livestock industry has numerous and diverse impacts on the environment. Everyday farming practices, combined with continuous real-time monitoring of animal parameters, can have a significant impact on the assessment of animal welfare and health, and hence on the environment, which are current topics of public interest. Animal husbandry and the environment are two concepts that are constantly intertwined. This paper reviews and analyses the environmental impact of current livestock management practices and highlights the critical role of Precision livestock farming (PLF) in ensuring the effective application of existing and new information on farms as a potential guideline to reduce the problems and risks of environmental impact. Strategies and methods to reduce environmental risk situations are being explored. Solutions are proposed with an emphasis on PLF as a useful monitoring tool in this regard. For risk analysis of agricultural sites, quantitative models are proposed. These formal models are based on the portfolio theory.

Keywords: environmental impact, PLF, IoT, livestock management, mitigation strategies, risk analysis.

INTRODUCTION

The increasing consumption of food of animal origin in recent years has necessitated an increase in its production on farms. On the one hand, this leads to the creation of a greater number of farms with large herds. On the other hand, this can lead to a number of risks, including sudden changes in the By applying information technologies such as software (cloud computing, artificial intelligence) and hardware (sensors, computers, and smartphones) in livestock farming, it is possible to automatically monitor and control environmental, physiological, and behavioral variables, ensuring the productivity and well-being of livestock in relation to the environment without any disturbance or manipulation. A major challenge in the livestock sector is how the environmental impact of the sector should be resolved. Food production accounts for 26% of global greenhouse gas emissions [1]. The Intergovernmental Panel on Climate Change (IPCC) guidelines, which focus on farm activities, state that agriculture is responsible for over 10% of greenhouse gas emissions in the EU, with the majority of these emissions coming from the livestock sector. According to [2], more than 90% of NH_3, 37% of CH_4 and 65% of N_2O in the atmosphere come from the livestock sector. This sector uses up to 30% of total land and 8 to 15% of water resources. A major contribution to reducing environmental

impact would be to manage livestock production so that the performance of animals is closer to their genetic potential - less feed use, less manure and higher productivity. Keeping farmers competitive is a challenge and animal productivity is a key factor.

Digitalisation provides an opportunity to increase the competitiveness of the agricultural sector. The entry of information and communication technologies (ICT) into livestock farming and the increasing use of the Internet of Things (IoT) are opening up a new era of connectivity, in which things, people and animals are part of an exchange of data networks, leading to a new philosophy of the agricultural sector.

A number of authors [3-6] identify Precision livestock farming (PLF) as a valuable tool for reducing the environmental impact of livestock production. With PLF, farmers can ensure the good health and welfare of their animals, achieving good productive and reproductive outcomes, and reducing the environmental impact per unit of animal product. The main objective of PLF is to make livestock farming more economically, socially, and environmentally sustainable. This can be achieved through observation, behavioral interpretation, and where possible, individual animal control. Daily farming practices combined with continuous real-time monitoring of animal parameters can have a significant impact on reducing the problems and

---

* To whom all correspondence should be sent:
E-mail: elisaveta.trichkova@iict.bas.bg

risks associated with environmental impacts. More research is needed to better analyze and assess the actual potential of PLF as a guideline for reducing environmental impacts.

This paper reviews and analyses the environmental impact of current livestock management practices and highlights the critical role of PLF in ensuring the effective application of existing and new information on farms as a potential guideline to reduce the problems and risks of environmental impact. Strategies and methods to reduce environmental risk situations are being explored. Quantitative models are proposed for the risk analysis of agricultural sites. These formal models are applied from portfolio theory. This provides a basis for applying this theory to farm management decisions. The aim is to maximize return and minimize risk. By minimizing economic risk, potential losses in livestock production can be reduced. This would reduce the problems and risks associated with environmental impacts.

Environmental effects

Livestock farming is a key factor for sustainable agricultural production. They contribute to food security, nutrition, poverty reduction, and economic growth. By adopting best practices, the sector can reduce its impact on the environment and become more efficient in its use of resources.

The livestock sector is an important user of natural resources and has a significant impact on the environment, including air quality, global climate, land, soil quality, water quality, and biodiversity (Figure 1).

- A growth in meat consumption worldwide, leads to an increase of waste by livestock systems that pose dangers to the environment.
- Another impact of livestock farming on soil is the environmental pollution by antibiotics. Antibiotics are often used in the farming industry as veterinary drugs and growth promoters for therapeutic purposes.
- Livestock farming impacts on air through the emissions of ammonia (NH_3) and Green House Gases (GHG), arising simultaneously from animal housing, yards, manure storage and treatment, and land spreading. According to [7], implementing PLF ventilation control systems in animal housing can be reduced NH_3 emissions by 60-65%.
- Field application of livestock manure supply nutrients and micro-elements useful to crop growth, but also elements that can accumulate in their tissues and enter in the food chain.
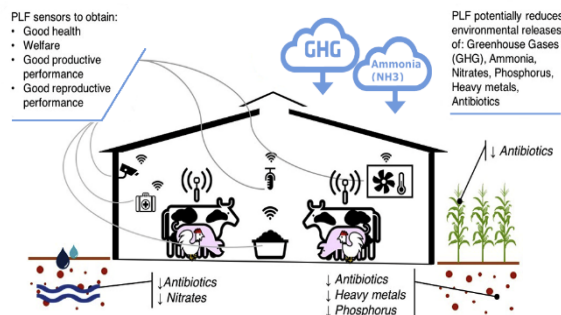
Figure 1. Effects of livestock farming on the environment [21]

Agriculture is responsible for the majority of global greenhouse gas emissions, according to the European Court of Auditors (ECA) [8].

Figure 2 shows the three main types of greenhouse gas emissions from agriculture, their main sources in the EU, and the share of these sources in total emissions from agriculture, which represent about 13% of total EU-27 greenhouse gas emissions (including an additional 2.7% from land use emissions and greenhouse gas removals from arable land and permanent grassland). Additional emissions not included in Figure 2 arise from the use of fuels for machinery and heating buildings, accounting for about 2% of total EU-27 emissions.

Figure 2. Main greenhouse gas emissions sources (CO_2 equiv.) Source: ECA based on the EU-27 GHG inventories in 2018 (EEA greenhouse gases, European Environment Agency (EEA)), [8]

Mainly methane (CH_4) from:
- Digestion of cattle and sheep feed.
- Storage of cattle and pig manure.

Mainly nitrous oxide (N_2O) from:
- Application of chemical fertilizers.
- Manure applied by farmers or deposited by grazing cattle.

Mainly carbon dioxide (CO_2) from:
- Treatment of drained organic soils (peatlands).
- Carbon sequestration on grassland and arable land.

Figure 3 shows the share of EU-27 emissions in 2020 (% of total kt (kilo tonnes) along gas), including the three main types of GHG. According

to the statistics, the emissions of N_2O (CO_2eq) in 2020 are 166,830 kt (43.6%), of CO_2 - 9,722 kt (2.5%), of CH_4 (CO_2eq) - 205,897 kt (53.8%).
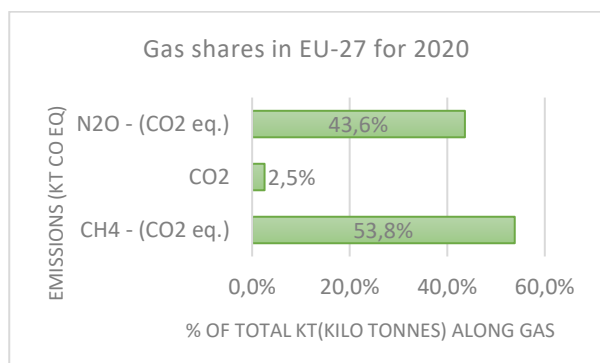
Figure 3. Gas shares in EU-27 for 2020. (Source: EEA greenhouse gases)

Trends in the EU from 2000 to 2020 for the three types of GHG emissions are shown in Figure 4.
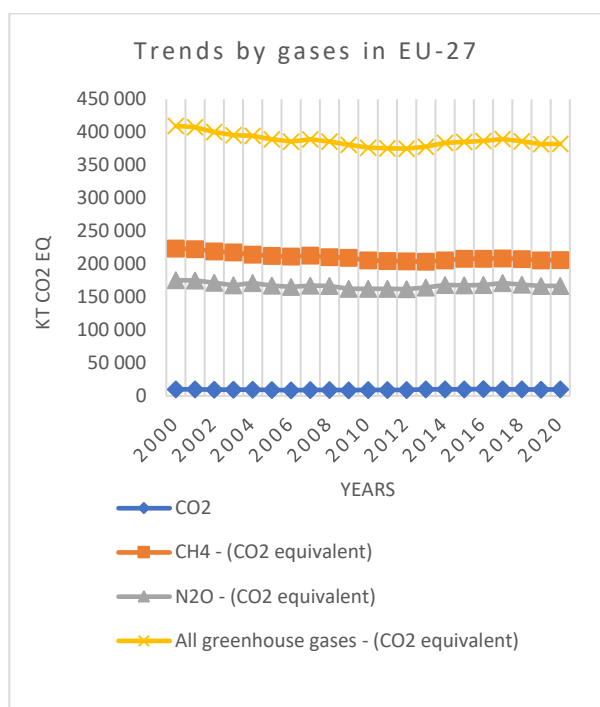
Figure 4. Trends by gases in EU-27 from 2000 to 2020, (Source: EEA greenhouse gases)

Some land use practices provide opportunities to reduce emissions and remove carbon dioxide (CO_2) from the atmosphere by storing carbon in the soil or in biomass (plants and trees). These practices include the restoration of drained peatlands or afforestation.

Emissions from the livestock sector, which mainly come from livestock farming, account for about half of the agricultural emissions and have remained stable since 2010.

Figure 5 shows the evolution of greenhouse gas emissions over the period 2000-2020. Between 2000 and 2010, they decreased mainly due to a decrease in fertiliser use and the number of farm animals. After 2010, emissions stopped falling.

According to the Intergovernmental Panel on Climate Change (IPCC, 2020), emissions of all greenhouse gases in the EU-27 from livestock, road transport, and public electricity and heat sectors are on a declining trend towards 2020. This trend is particularly pronounced in the energy sector, especially in the public electricity and heat sector (from 1,222,897 gigatonnes of CO_2 equivalent (CO_2eq) in 2003 to 655,620 tonnes of CO_2eq in 2020) (Figure 6). This indicates that more serious attention needs to be paid to so-called "green energy".
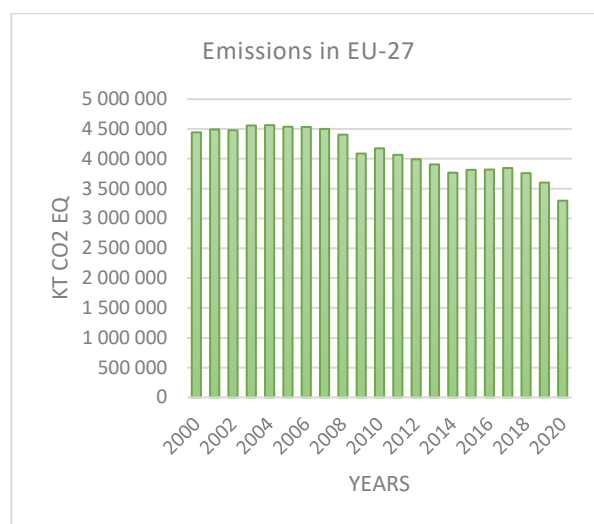
Figure 5. GHG emissions from agriculture in the EU-27 since 2000. (Total emissions (UNFCCC)) (Source: EEA greenhouse gases)

The research in [9] is aimed at investigating biogas production technologies, evaluating feedstocks and products, carefully investigating and evaluating all possible feedstock and product flows, and assessing the environmental impact of this activity. Based on the study, an optimisation model using Mixed Integer Linear Programming (MILP) was developed to determine potential locations and optimal parameters as well as transport flows of existing and potential activities.

However, the adoption of existing best practices and technologies in animal nutrition, health, and husbandry, as well as improved manure management, can make the global livestock sector more sustainable and reduce greenhouse gas emissions by up to 30%. In addition, carbon sequestration in biomass and pasture soils can significantly offset emissions from livestock production.

119
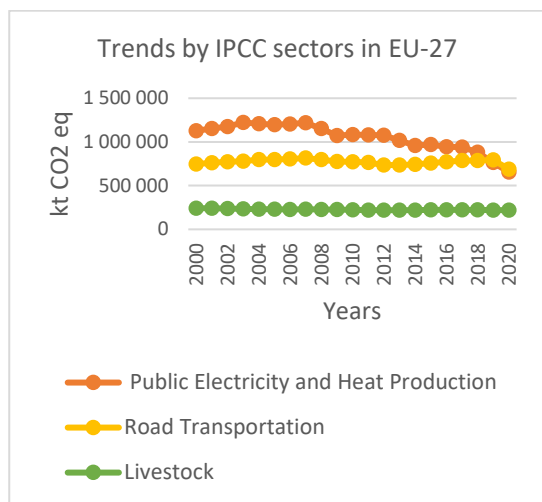
Figure 6. Trends by IPCC sectors in EU-27 since 2000. (Source: EEA greenhouse gases)

Mitigation strategies and methods

To address all of these issues, livestock systems and related agricultural activities need to move towards more sustainable practices.

The concept of sustainability applied to agricultural/livestock systems means that production levels are maintained within the capacity of the ecosystem that supports them.

The livestock sector is therefore in a difficult position, having to maintain high levels of production while at the same time improving its environmental performance.

Several sustainable development goals considered important and relevant to livestock production are shown in Figure 7.
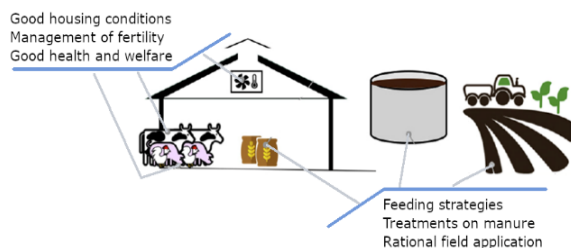
Figure 7. Mitigation strategies adopted in livestock farming [21]

These include fertility management, good health and welfare, good housing conditions, feeding strategies, rational field application, manure treatment.

According to [10, 11], an important step in the development of biotechnological process models is parameter identification by solving inverse problems. In [12, 13], an approach for parameter identification of multi-parameter models is proposed. This approach has been tested for the modelling of fermentation systems. The results

obtained show a reduction in the model error variance at each successive hierarchical level.

Therefore, in the face of resource scarcity and with a view to reducing greenhouse gas emissions, the sector must maximise efficiency in production, animal welfare and profitability for farmers using practices and technologies that reduce environmental impact.

According to [14], in order for livestock production to cope with the impacts of climate change, several mitigation strategies need to be adopted. Mitigation potentials can be grouped into three main categories: 1) intensification and related structural changes in the livestock system; 2) technical and management interventions; and 3) moderate demand for animal products [15]. The last category is less realistic due to the increasing global demand for animal products [16].

In recent years, considerable research effort has gone into developing methods and strategies to mitigate and reduce the environmental impact of agricultural practices. There is no mention in the literature of PLF technology specifically designed to reduce the environmental impact of livestock production. However, the use of PLF to support management strategies can reduce the environmental impact of farms. There are a number of issues that need to be addressed in this sector, such as monitoring animal health and welfare, reducing environmental impact and ensuring process productivity. PLF aims to provide farmers with a real-time monitoring and management system. This is fundamentally different from other approaches that attempt to monitor animal welfare, such as using human experts to assess animal-based indicators. These methods do not improve the life of the animal being monitored. It is much better to identify a problem while the animal is being reared and take immediate management action.

PLF allows the biological responses of animals to be continuously monitored, modelled and controlled. The continuous monitoring of PLF allows the farmer to intervene as soon as animals show the first signs of poor welfare or health [17]. Thus, good production outcomes based on animal health and welfare achieved through PLF can reduce the environmental impact of livestock production [18]. In other words, by optimising livestock performance, PLF indirectly reduces environmental impacts.

Internet of Things (IoT)

PLF is helping to improve the efficiency of livestock farming through the use of advanced IoT technologies and methods. By implementing smart solutions, many benefits are achieved such as:

improved animal health and welfare, increased economic efficiency, more optimal use of resources, precise control of all necessary processes, reduced carbon footprint and environmental impact of farms. Some studies have focused on ventilation to improve indoor air quality [7], ammonia emission measurement procedures [19] and dust monitoring in agricultural buildings [20]. Thus, the application of PLF methods improves the overall management of livestock farms [21].

In [22], the authors describe how PLF technology can provide solutions by describing its basic principles and how it can be applied on a larger scale.

Figure 8 shows how IoT offers many opportunities for modern farms, such as the collection of large amounts of data, information on the individual condition of animals and easy response to their needs, monitoring and control of various parameters.

The signals are sent and processed in cloud data centers and the control signals are sent back to the farm.

The point of IoT is to connect multiple standalone devices (sensors and controllers) to a local network, cloud server or the Internet. This creates an automated intelligent system that uses the information gathered from the devices and helps manage them in a unified and efficient way. For example, the extension of IoT with W-IoT technology is widely used in modern livestock farming for animal health monitoring and early disease detection. This application is supported by real-time analysis of animal health data sent by sensors.

Expanding IoT has led to a significant increase in the amount of data generated. To address the issue of processing and storing all the requirements and constraints associated with smart agriculture, cloud computing, and big data provide numerous tools [23].

The authors of [24] review, analyse and compare eight farm management software (FMS) platforms. The comparison is made based on several key features that characterise a modern FMS platform designed to make livestock and crop production more profitable, efficient and secure.

FMS platforms help to manage and solve many tasks of varying complexity [25]. Various tools aim to make important decisions in a short time. Farming and livestock applications not only speed up the process. They also provide a well-informed background. This increases the chances that the solution will be correct. A great advantage of modern life is that the entire complexity of these operations can be automated and digitised [26].
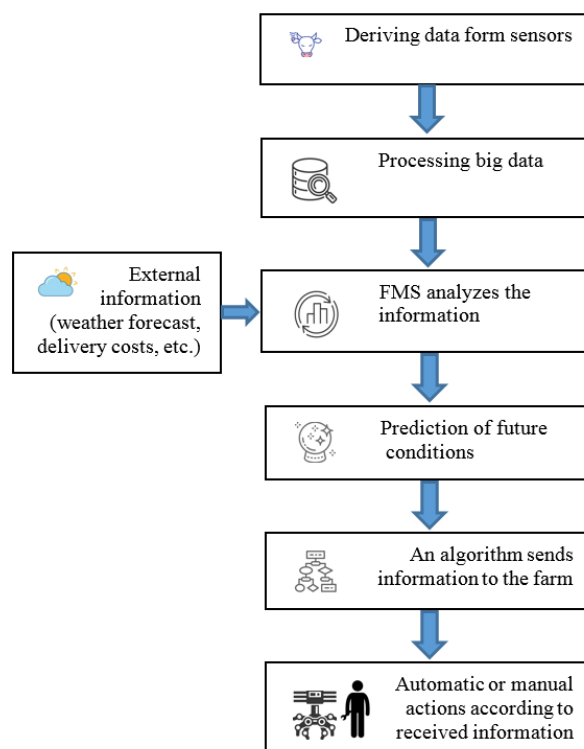
Figure 8. Application of IoT in Smart farming [22]

As a whole, there are three main applications of monitoring in precision farming: monitoring of livestock, monitoring of fields, and monitoring of greenhouse gases [27]. IoT allows farmers to monitor livestock using multiple sensors that monitor multiple animal variables such as heart rate, temperature and digestion. Field monitoring applications are designed to report on various conditions such as soil fertility, temperature, gas content, and the presence of disease in crops [28]. The use of IoT sensors and devices has also made it possible to remove some of the need for manual intervention. This has led to the development of intelligent greenhouses that can monitor and regulate various climatic parameters according to the needs of the plants [23].

Big Data

The vast amount of information produced and collected every day is processed and analysed using Big Data, which is beyond the capabilities of traditional techniques. Big Data serves as the basis for advanced technological and statistical tools that analyse huge amounts of data and extrapolate information. Big Data makes it possible to handle and use this ever-growing amount of data quickly and easily [29].

A key feature of Big Data is that it can be used to extract a huge amount of values, which requires the use of complex analytical methods.

Data processing covers a wide range of applications. These include image or video processing, decision support systems, and data loading and collection. Depending on the system requirements, any functionality that can work simultaneously to provide other services can be integrated.

On-farms risk management

Farm management is one of the most important resources in farm operations. Farm management determines how farm life is organised, how resources are allocated and how activities are carried out. It deals with different strategies and methods to keep a farm productive, sustainable, resilient and profitable. This would reduce the problems and risks associated with environmental impacts.

Decision making is the core activity of management. All decisions have certain outcomes or consequences [30]. In many situations, however, the outcome of a decision cannot be predicted.

Management strategies and sources of risk at agricultural sites are described and analysed in [31]. A comprehensive analysis of risk types and their assessment is given in [32]. Research and recommendations for risk management in agriculture are the focus of resource-based farm management [33, 34]. The management of farms aims at sustainable development and predictable results in their operation [35, 36]. The application of PLF technologies makes it possible to manage agricultural sites with quantitative assessments and the application of logical and formal models. This is a prerequisite for achieving optimal results in farm management, maximising production and income and minimising costs. Quantification approaches are recommended and applied in farm management [35] and environmental tasks [37]. The management of agriculture is aimed at the prospective development of production and economic performance [38-40]. The management is evaluated in an integral form by means of economic criteria [41]. Various criteria can be used to quantify the economic situation of a farm and its development. These criteria quantify the variables and parameters of its exploitation. The main issue is to provide a quantitative assessment of the components that result from the activities of the management of the farm. Such types of criteria, variables and parameters in management are discussed in detail in [42]. An important policy to follow when making production and financial decisions is to manage farms through risk aversion [43].

Sustainable management generally focuses on minimising risk and maximising return from the management of production and economic activities. All activities that the farmer is expected to manage are shown in Figure 9 and include:

1) Planning (doing scenario analyses);
2) Organization (resource allocation);
3) Monitoring (data collection/acquisition);
4) Controlling (comparison of actual and targeted key performance indicators (KPIs);
5) Identification of optimization opportunities (maximising profit and minimising risk).
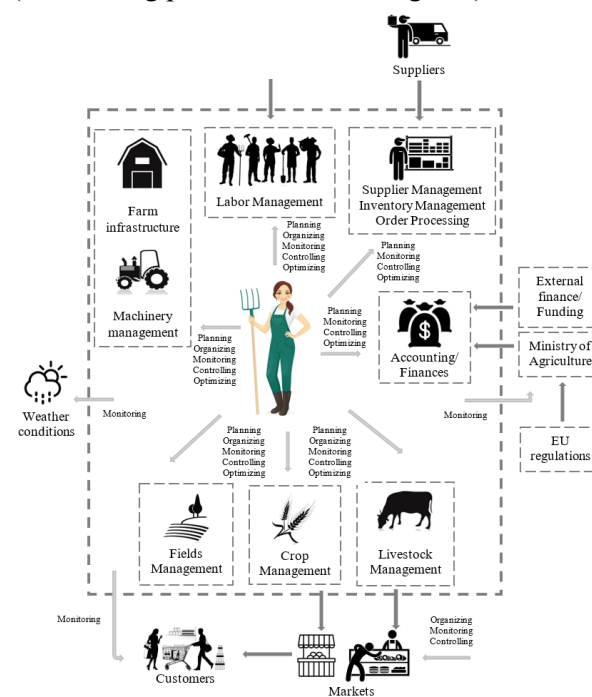
Figure 9. Farm management activities [22]

By minimising economic risk, potential losses in livestock production can be reduced and these are the guiding criteria for planning future resource allocation. The new point added in this study is the intelligent quantification of the functionality of the farm in order to reduce risk and at the same time analytically determine the best trade-off between return and risk.

The analytical formalisation of management decisions in the farm can be done by using relations from modern portfolio theory. The latter derives models that simultaneously consider the requirements for increasing the portfolio return and reducing the portfolio risk. The formalisation and quantification of risk indicators are successfully applied in portfolio theory [44-47]. Risk has a stochastic nature and its management must take this random behaviour into account [48, 49]. The statistical characteristics of a stochastic variable $R_i(t)$ change its values mainly in the diapason [E_i-σ_i, E_i+σ_i], where the value E is the average level of the stochastic variable for a given period. Therefore, if

the risk σ_i has a small value, the range around the mean E_i will be small and the real value of the stochastic variable $Ri(t)$ will be close to the mean E_i. This will benefit the quantification of the real value and its prediction for the case of decision making in farm management. In the opposite case, if the risk σ_i is a large value, it means that the real value of the stochastic parameter can vary in a wide range around the mean E_i, and the value $R_i(t)$ can be considered to be higher or lower than the estimated mean E_i. This case is not favourable for the management of the farm, since it is determined that there is a significant risk in the use of this variable in management. The real level of this parameter $R_i(t)$ can be in the range $[E_i\text{-}\sigma_i,\ E_i+\sigma_i]$, which in the case of high risk σ_i can be significantly different from the mean E_i.

The formal analytical relations for describing the mean value and the risk of a stochastic variable are performed with linear and quadratic relations. For a set of N random variables $R_i(t)$, their values are recorded in a discrete set of sequences of n values in time,

$$R_1 = [R_1^{(1)}, R_1^{(2)}, ..., R_1^{(n)}]$$
$$.... \qquad (1)$$
$$R_N = [R_N^{(1)}, R_N^{(2)}, ..., R_N^{(n)}].$$

These records make it possible to estimate the mean value E_i of the N variables for this time interval $1\div n$ and the corresponding deviations σ_i^2.

$$E_i = \frac{1}{n} \sum_{k=1}^{n} R_i^{(k)}$$

$$\qquad (2)$$

$$\sigma_i^2 = \frac{1}{n} \sum_{k=1}^{n} (E_i - R_i^{(k)})^2, i = 1 \dots N.$$

In this way, the risk of the stochastic variable $R_i(t)$ is estimated numerically as the standard deviation σ_i.

Another form of risk quantification is provided by the inequality of probabilities, which is applied with the Value at Risk (VaR) parameter [50]. VaR quantifies the level of risk in terms of the maximum probable loss [47]. There is an attempt to apply the VaR form of risk to resource allocation [51, 52]. The quantification of risk in the formal definition of VaR is applied in supply chain networks [53]. The estimation and use of the VaR formalisation is accepted as a promising way to manage risk [51].

The formal representation of VaR is shown by the density function of the risk index, which represents the return and loss variable in farm management. The positive value of the portfolio return is the farm management profit and the negative value is the loss [54].

The formal models discussed are applied from portfolio theory. This provides a basis for applying this theory to farm management decision making. The aim is to maximise return and minimise risk. The application of elements of portfolio theory can be found in [48], where the components of the portfolio are applied to inventory policy. In particular, risk in the form of VaR is formalised in terms of probabilistic relations. Such a probabilistic form of risk is used in [55] for decision making in inventory control in farm management. In [53], the VaR parameter is used to quantify the risk in the allocation of resources on a farm.

CONCLUSION

The EU's role in mitigating climate change in agriculture is crucial, as it sets environmental standards and co-finances most Member States' agricultural spending.

Ongoing technological development and validation of theoretical aspects and prototypes are contributing to the creation of diagnostic tools for PLF that can detect on-farm problems without manipulating animals (non-contact and non-invasive data collection) or inducing stress, providing the opportunity for early detection of disease outbreaks. In this context, the benefits to farmers include improved decision making, increased interest in the sector among young farmers, and a positive impact on overcoming problems and gaps with the end user by transforming raw data into useful information that can currently only be obtained through expert analysis and interpretation.

This paper reviews and analyses the environmental impacts of current livestock management practices and highlights the critical role of PLF in ensuring the effective application of existing and new information on farms as a potential avenue for reducing environmental impact issues and risks. Strategies and methods to reduce environmental risk situations are considered. Solutions are proposed with an emphasis on PLF as a useful monitoring tool in this regard.

Quantitative risk analysis models based on portfolio theory are proposed. Subsequently, the research will focus on the application of these models to achieve optimal production and environmental performance by minimizing risk situations at agricultural sites.

REFERENCES

1. J. Poore, T. Nemecek, *Science,* **60** (6392), 987 (2018).
2. FAOSTAT, Statistical Databases. Food and Agriculture Organization of the United Nations, Rome, 2021.
3. D. Berckmans, *Animal Frontiers*, **7** (1), 6 (2017).
4. A. N. Hristov, T. Ott, J. Tricarico, A. Rotz, et al., *Journal of Animal Science*, **91(**11), 5095 (2013).
5. P. Llonch, M. J. Haskell, R. J. Dewhurst, S. P. Turner, *Animals*, **11** (2), 274 (2017).
6. S. Shields, G. Orme-Evans, *Animals,* **5**(2), 361 (2015).
7. G. Zhang, P. Kai, C. Zong, *Papers Presented at the 6th European Conference on Precision Livestock Farming*, ECPLF, 883 (2013).
8. Common Agricultural Policy and climate, ECA 2021, Special Report:https://terraevita.edagricole.it/wp-content/uploads/sites/11/2021/06/La-relazione-della-Corte.pdf
9. E. Ganev, V. Beschkov, *Bulgarian Chemical Communications*, **54** (3), 205 (2022).
10. Boyadjiev Chr., P. Popova-Krumova. Chapter 1. *Progress in Chemical Science Research*, Vol. 2, B P International, 2022.
11. Chr. Boyadjiev, , M. Doichinova, , B. Boyadjiev, P. Popova-Krumova, Springer-Verlag, Berlin Heidelberg, 2016, p. 313.
12. P. Popova-Krumova, Chr. Boyadjiev, Chapter 7, In book: Modeling and Simulation in Chemical Engineering, Project Reports on Process Simulation, Chr. Boyadjiev (ed.). Springer International Publishing, Book Series: Heat and Mass Transfer, 2022, p. 147.
13. P. Popova, Chr. Boyadjiev, *Biochemical Engineering Journal*, **39** (2), 397 (2008).
14. T. Kaufmann, *Animal Nutrition*, **1** (3), 104 (2015).
15. M. Herrero, B. Henderson, P. Havlík, et al. *Nature Clim. Change,* **6**, 452 (2016).
16. M. Rojas-Downing, A. P. Nejadhashemi, T. Harrigan, S. A. Woznicki, *Climate Risk Management*, **16**, 145 (2017).
17. K. N. Dominiak, A. R. Kristensen, *Computers and Electronics in Agriculture*, **133**, 46 (2017).
18. T. Van Hertem, L. Rooijakkers, D. Berckmans, et al., *Computers and Electronics in Agriculture*, **138**, 1 (2017).
19. E. Vranken, D. Berckmans, *Animal Frontiers*, **7**(1), 32 (2017).
20. T. G. M. Demmers, Q. Tong, L. Rooijakkers, E. Koenders, *Papers Presented at the 7ᵗʰ European Conference on Precision Livestock Farming*, ECPLF 2015, p. 525.
21. E. Tullo, A. Finzi, M. Guarino, *Science of the Total Environment*, **650**, Part 2, 2751 (2019).
22. E. Paunova-Hubenova, E. Trichkova-Kashamova, *7th IEEE International Conference "Big Data, Knowledge and Control Systems Engineering"* (BdKCSE'2021), IEEE, 2021, p. 1.
23. H. Ibrahim, N. Mostafa, H. Halawa, M. Elsalamouny, R. Daoud, H. Amer, Y. Adel, A. Shaarawi, A. Khattab, H. ElSayed, *SN Appl. Sci.*, **1**, 223 (2019).
24. E. Trichkova-Kashamova, E. Paunova-Hubenova, *International Conference Automatics and Informatics (ICAI)*, IEEE, 2021, p. 1.
25. S. Fountas, G. Carli, C. G. Sorensen, Z. Tsiropoulos, C. Cavalaris, A. Vatsanidou, … B. Tisserye, *Computers and Electronics in Agriculture,* **115**, 40 (2015).
26. I. Hristoski, O. Kostoska, T. Dimovski, Z. Kotevski, *Conference: 5th International Balkan and Near Eastern Social Sciences Congress Series (IBANESS)*, 2017, p. 375.
27. .M. S. Farooq, S. Riaz, A. Abid, K. Abid, M. A. Naeem, *IEEE Access*, **7**, 156237 (2019).
28. F. Basçiftçi, K. A. Gündüz, *In Proceedings of the 4th International Conference on Computer Science and Engineering (UBMK)*, 2019, p. 58.
29. S. Morrone, C. Dimauro, F. Gambella, M. G. Cappai, *Sensors,* **22**(12), 4319 (2022).
30. V. Ts. Mitev, *Finance: Theory and Practice.*, **26**(6),166 (2022).
31. S. P. Narayan, K. R. Chaudhary, *Indian Journal of Animal Sciences*, **88**(5), 612 (2018).
32. D. Kahan,). FAO 2013 (2008).
33. J. Harwood, R. Heifner, K. Coble, J. Perry, A. Somwaru, *Division Economic Research Service, U.S. Department of Agriculture, Agricultural Economic Report* No. 774 (1999).
34. Deloitte, *Model risk management,* 2017.
35. Z. Win, A. Campbell, S. R. J. Magalhães et al. *J. Trop. Anim. Health Prod.,* **51**, 643 (2019)..
36. N. Scialabba, C. Schader, A. Muller, *Proceedings IAHA Preconference and Workshop*, 12-15, IFOAM 18th Organic World Congress in Istanbul, 2014.
37. P. Garcia-Diaz, T. Prowse, D. Anderson, M. Lurgi, R. Binny, P Cassey, *J. Conservation Science and Practice*, **1** (2). (2019).
38. D. Obućinski, R. Prodanović, D. Pelić, N. Puvača, *J. of Agronomy, Technology and Engineering Management*, **2**(1), 228 (2019).
39. , S. Ishchenko, , K. Skrypniuk, , D. Pyrogov, T. Tkach, *SHS Web of Conferences*, **73**, 0100 (2020).
40. S. Dimitrov, K. Pavlova, *Proceedings of 8th International Conference on Energy Efficiency and Agricultural Engineering (EE&AE)*, 2022, p. 1.
41. O. Flaten, G. Lien, M. Koesling, P. S. Valle, M. Ebbesvik, *J. Livestock Production Science*, **95** (1–2), 11 (2005).
42. A. Woodend, Published by the Department for environment, food and rural affairs*,* (2010).
43. E. Gilbert, L. Meiklejohn *Investment Analysts Journal*, **48**(3), 223 (2019).
44. W. Sharpe, McGraw Hill, London, UK, 1999, p. 316.
45. Al. Janabi, Taylor Francis group, 2019, p. 1.
46. A. M. Malz, John Wiley & Sons, Inc., 2011, p. 722.
47. H. Du Plessis, P. Van Rensburg, *Investment Analysts Journal*, **49**(3), 243 (2020).
48. P. Šimovic, A. Tafro, *J. Mathematics*, **9**, 2038 (2021).

49. P. Guo, Y. Jia, J. Gan, X. Li, *J. Mathematics*, **9**, 2097 (2021).
50. K. Dowd, John Wiley & Sons Inc, Second edn., 2005, p. 390
51. E. Luciano, L. Peccati, D. Cifarelli, *Int Journal of Production Economics*, **81–82**, 375 (2003).
52. B. Zhi, X. Wang, F. Xu, *J. Computers & Operations Research,* **136**, 105481 (2021).
53. E. Khorshidi, V. R. Ghezavati, *SN Appl. Sci.* **1***,* 1671 (2019).
54. A. V. Rutkauskas, V. Stasytytė, *Journal of Business Economics and Management*, **21**(1), 136 (2020).
55. T. Xin-shu, L. Wei, *IEEE International Conference on Control and Automation, ICCA,* 2007, p. 2740.

Effect of surfactants and wetting agents on the electrochemical characteristics of Ni/Zn batteries

L. S. Soserov, A. E. Stoyanova*

Institute of Electrochemistry and Energy Systems, Bulgarian Academy of Sciences, Acad. G. Bonchev Str, 10, 1113 Sofia, Bulgaria

Nickel-zinc batteries are an attractive ecologically acceptable electrochemical system characterized mainly by good gravimetric energy density, high discharge acceptance, low cost and excellent safety. Historically, their unsatisfactory cycling stability largely due to electrode shape change, dendrite formation and zinc electrode corrosion are the major obstacles limiting their wider market penetration. In the present study we are investigating and optimizing some arrangement of the Zn active mass composition used as a negative electrode in these batteries. Through the use of various additives and some wetting agents, the substantial influence that the binders have on the performance of the zinc electrode is demonstrated. The use of surfactants, on one hand, reduces to some extent the resistance of the electrode, but on the other hand, increases its weight loss, consequently demonstrating a reduction of the operating cell life. Work in this direction is continuing using other pre-selected binders and surfactants on electrodes having larger size and/or cells configured with more electrode pairs. The use of gelled and/or membrane electrolytes may also lead as an additional barrier toward Zn dendrite formation and thus enhancing and prolong cell life.

Keywords: Ni/Zn batteries, surfactants, wetting agents

INTRODUCTION

With the progression and development of human society, the accelerated depletion of traditional energy sources and environmental pollution has become a focus of an extensive concern. Thus, the exploration of economic, environment friendly and reliable renewable energy sources is continuing to be a prevailing trend. Sustainable energy transitions require formulation of effective policies promoting and exploring biomass resources, increasing use of renewable and low carbon sources and discouraging the use of fossil fuels and unsustainable natural resources [1, 2].

In parallel, alternatively to this direction, a new look is taken on the development of a new generation of systems for accumulating and storing energy, as well as enhancing the existing ones. Table 1 compares some of the main electrochemical performances of different electrochemical sources we currently use. Among these power sources, lithium-ion batteries were deemed as one of the superior candidates due to their high output voltage and high energy densities [3, 4]. However, lithium-ion batteries are still insufficient for various applications because of the imminent safety problems such as short circuit due to Li dendrite formation and side reactions of $LiPF_6$ and organic carbonates under overcharge or high temperature. It

is very difficult to achieve a fast-charging algorithm, related to the overheating of the system decreasing its safety behavior. High costs and harsh using conditions also put limits to its wide use in many particular applications.

On the other side, nickel-zinc (Ni/Zn) batteries are showing an increased research interest due to their impressive theoretical specific energy density (≈372 Wh kg^{-1}), acceptable output voltage (≈1.8 V), sufficient and inexpensive zinc resources, and low environmental concerns [6]. Manufacturing the nickel-zinc (Ni/Zn) battery is a promising technology for use in hybrid/electric vehicles and new portable devices. It delivers high specific energy (70–85 Wh kg^{-1}) and specific power (140–200 W kg^{-1}), and the operating cell voltage (1.6 V) is by 400 mV higher than that of Ni/Cd and Ni/MH batteries [7-9]. Definitely, they are an excellent choice for all of the stationary applications, where the low weight of Li batteries is losing its advantage. Nickel-zinc batteries play a significant role in consumer electronics applications such as digital cameras, portable lighting apparatus and cellular phones, because of their unique advantages like high output voltage and splendid power density [10]. Last but not least, it should be noted that Ni/Zn batteries can be almost completely recycled in the absence of residual pollutants and emissions, as shown in Figure 1 [11].

* To whom all correspondence should be sent:
E-mail: antonia.stoyanova@iees.bas.bg

Table 1. Comparison of the main characteristics of different types of batteries [5]

Parameter/Battery	Pb-Acid Flooded	PB-Acid TPPL	NiCd Pocket	NiMH	NiZn Prototype	Li-Ion
Nominal Cell Voltage, V	2.11	2.16	1.2	1.2	1.65	3.2-3.8
Gravimetric Energy, $Whkg^{-1}$	30-34	40-44	20-30	50-60	70-85	95-110
Volumetric Energy, WhL^{-1}			35-60	100-120	>135	
Gravimetric Peak Power (15 sec), Wkg^{-1}			20 – 75	>1000	>1000	
Volumetric Peak Power (15 sec), WL^{-1}			30-135	>1000	>1000	
High Current Discharge at low SOC	No	No	Partial	Partial	YES >5C	YES >2C
Operating Temperature, ºC			-30 to +45	-20 to +40	-30 to+60	
Life @ 80% DOD; C/5			>500	800	>500	
Charge/Discharge Factor			>1.4	>1.25	<1.03	
Self-discharge, %/day	Moderate	Moderate	0.3-0.5	3 to 5	0.2-0.3	0.5-1.0
Recharge Time (> 80% SOC), h	8-10	8-10	2.5-3	1-2	0.5-1	1-2
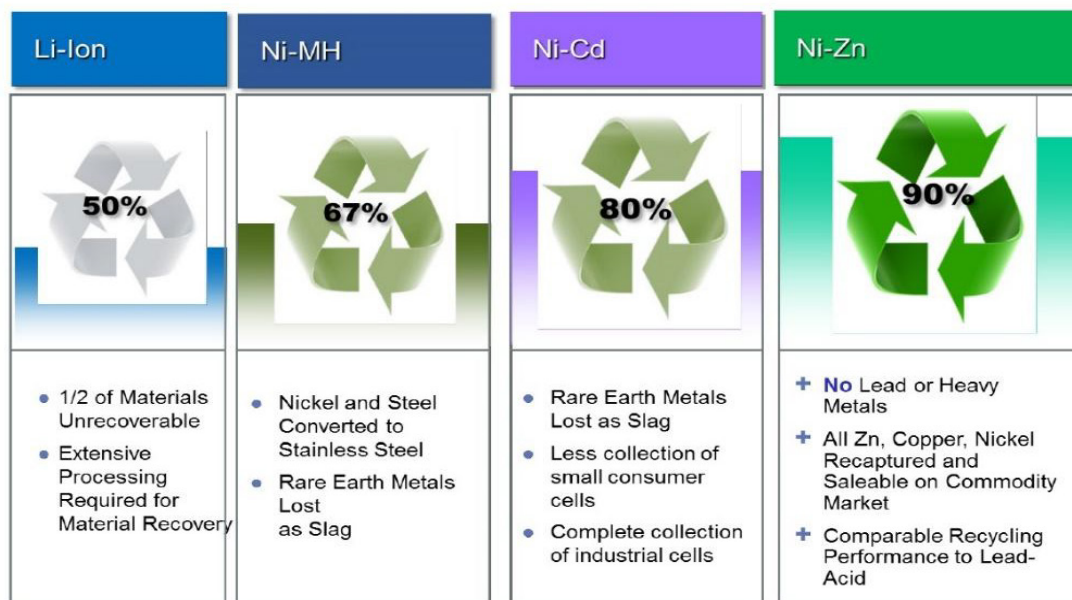
Fig. 1. Recyclability

However, some significant obstacles are still far away from a satisfactory level due mainly to the relative low power density and poor cycling stability of the Ni/Zn batteries due to the shape change, dendrite formation and corrosion of the zinc electrode leading to polarization, passivation and short-circuiting of full cell [8]. So far, many advanced techniques and strategies have been proposed to overcome the issues related to reducing the negative impact of zinc dendrites formation and their surface side reactions, which generally consist of coating the surface of the electrode. The

enhancement approach is mainly focused on structural optimization of the electrode, forming quasi-solid-state devices, applying some specific additives to the Zn electrode, optimization and modification of the electrolyte, use of double or triple layers separators, use of electrode substrate and current collectors increasing H_2 overvoltage, etc. [3, 4, 13-15].

The current collectors used for the two electrodes are playing an important role overcoming some of the existing shortcomings and thus optimizing the performance of the system. The three-dimensional (3D) substrates are the preferred solution and typically they are promoting prolonged life of the zinc electrode. It should be noted that the three-dimensional substrates significantly increase the internal electrochemically active area of the zinc electrodes, resulting in smaller current densities and achieving a longer life of the system.

A rechargeable nickel-zinc battery, based on enhanced and monolithic zinc sponge anodes has been developed showing a good energy density and cycle life [6, 16].

Copper is very widely used as a current-carrier due to its sufficiently good electrical conductivity. On the other hand, it has limited solubility in the alkaline electrolyte, which is enhancing the performance and lifetime of the batteries. Therefore, the use of copper substrate along with a galvanic coating of lead or tin are a favorable option, protecting the copper from dissolution and increasing the overvoltage of the zinc electrode to suppress the hydrogen evolution during overcharge, thus adversely improving the system performance [17].

In short, there is no one-size-fits-all solution; depending on the intended use of the battery, choices (in most cases a compromise) are made in the selection of the current collector.

Briefly recapping what was noted above, the problems associated with the zinc electrode can be summarized as shown below (in no order of importance):

1. Passivation (during discharge);

2. Shape change (during continuous charge/discharge);

3. Dendrite formation shortening the operational life (during charge/discharge);

4. H_2 evolution (during overcharging);

5. Solubility of zinc in the electrolyte (passage of zinc ions through the separator).

Having highlighted these major obstacles, the objective of the present work is to investigate and optimize the microstructure of the Zn electrode active mass by using different additives and wetting agents.

EXPERIMENTAL

1. *Zinc electrode* - The choice of the right binder and its used amount is very important during making of a good pasted Zn electrode. Most of the developed recipes indicated CMC (carboxymethyl cellulose) [18, 19] or HEC (hydroxyethyl cellulose) [20] as a good workable binder and indeed they are excellent binders, however being water soluble, over the time degrading into the electrolyte and the electrode integrity slowly goes down. In this study we are focusing on the use of a combination of CMC with an additional binder having increased stability in alkaline electrolyte. Polytetrafluoroethylene (PTFE) is a good choice, where the applied amount is critical – at higher amounts, the electrode resistance substantially increases, generating a lot of heat during charge and the output performance and life correspondingly goes down [21].

The basic recipe used is shown below:
1. 78 wt. % ZnO;
2. 10 wt. % metallic Zn powder;
3. 5 wt. % graphite flakes, mesh 325.99%;
4. 2 wt. % carboxymethyl cellulose (CMC);
5. 5 % PTFE (60 wt. % dispersion in H_2O).

The main component in the above shown recipe is ZnO. We used nanosized ZnO with particle size of 50 nm, offered by Ever Zinc. Pure 10 wt. % metallic Zn powder (Valerus) was also added to the active masses.

The experiments aiming to determine an optimal amount of PTFE, as well as of some surfactants, are summarized in Table 2.

Table 2. Zinc active mass variations

Binder	Surfactants			
	Without	Triton X-100	Dispex	Dispex + Triton X-100
2 wt. % CMC + 5 % PTFE	✓	✓	✓	✓
2 wt. % CMC + 8 % PTFE	✓	X	X	✓
5 - 12 % PTFE	✓	✓	✓	✓
2 wt. % CMC + 12 % PTFE	✓	X	X	✓

Fig. 2. Pasted Zn electrode

The Zn electrodes were prepared by applying the above-described paste compositions into Cu foam substrates with 45 × 65 mm dimensions, where the average active mass weight was 6-6.5 g as shown in Fig. 2.

2. *Nickel electrode* - As a Ni electrode during all of the experiments, we used commercial sintered Ni electrode with rated capacity of 115 mAhg^{-1} (Institute of Non-Ferrous Metals, Poznan, Poland) with dimensions of 85 × 40 mm as shown in Fig. 3.

Fig. 3. Sintered Ni electrode

3. *Electrolyte* - As an electrolyte alkaline solution of 30% KOH was used, in some of the experiments we applied gelling agents: PVA (135 000) + KOH; PVA (195 000) + KOH + TEAOH.

4. As a *Separator* "Viledon separator" with item number 700/18F was used.

5. *Electrochemical cell* - Exploiting the described electrodes, they were tested in a three-electrode configuration prismatic cell using a Hg/HgO reference electrode (Tianjin Aida Hengsheng Technology Development Co., Ltd.).

As marked above, the alkaline electrolyte in Ni/Zn cells did not directly participate in the electrochemical reaction, but it served only as a medium providing the corresponding ionic transport [25]. That's why typically these batteries were not required to be over flooded with electrolyte in order to reduce the solubility of the Zn electrode into the electrolyte. Most of the experiments were carried out in cells under semidry conditions. The cell assembly was equipped with a Hg/HgO reference electrode where the cell is limited in capacity by nickel electrode (negative/positive ratio >2), thus avoiding H$_2$ evolution, maintaining the Zn electrode to be always partially charged at the end of the charging step.

7. *Electrochemical tests* - In order to be properly activated, the assembled cell went through an initial formation cycle which is graphically shown in Fig. 4 below.

After properly activating the cell, a 2-step charge approach in order to avoid H$_2$ evolution as overcharge was applied. It first charges with constant current (CC) until a cell voltage of 1.9 V is reached, then continues charging, switching to constant voltage (CV) charging until the corresponding current drops to a predetermined level, usually C/40.

RESULTS AND DISCUSSION

Initially, experiments with different amounts of PTFE and surfactants were performed for 48 hours, (Fig. 5), then the cells were disassembled, electrodes were washed, dried and the weight loss was measured. It was found that the optimal amount of PTFE in the active mass should not exceed 5 wt. %. Use of larger amounts of PTFE significantly increased the electrode resistance, although smaller weight loss was measured. On the other side, using water soluble surfactants as ingredients leads to an increased electrode weight.

1. Run @ Room Temperature
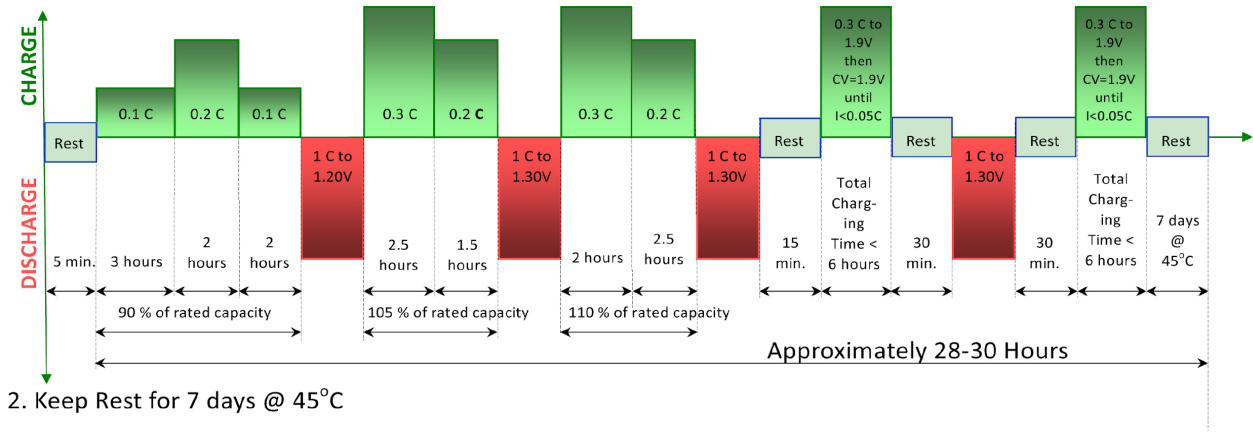
2. Keep Rest for 7 days @ 45°C

3. Cool Down to Room Temperature and Determine the Capacity
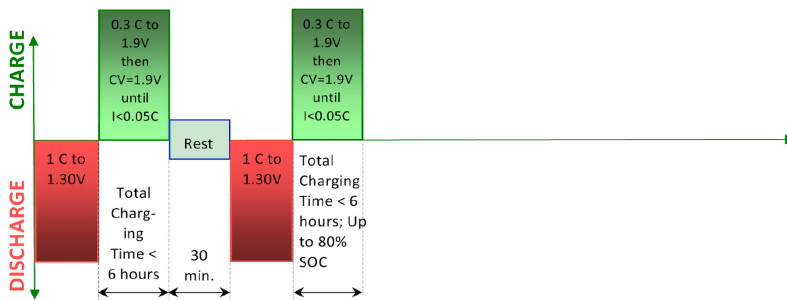
Fig. 4. Initial formation cycles
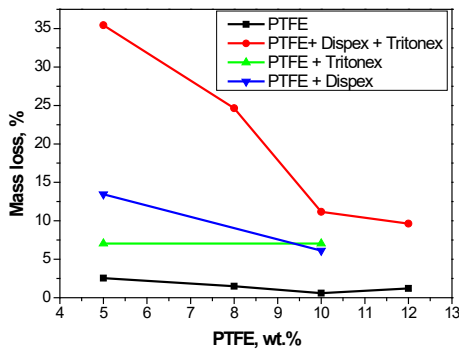
Fig. 5. Electrode weight loss

The anticipated positive impact of using surfactants on cell discharge capacity was not found, as shown on Fig. 6, where cells using 5 wt. % PTFE with and without surfactants are compared.

Apparently, the use of surfactants increases the electrode weight loss, without providing measurable change in surface tension and better electrolyte penetration inside the electrode. For better understanding of such a relationship and comparison of resulting ohmic resistance, the following experiment was performed:
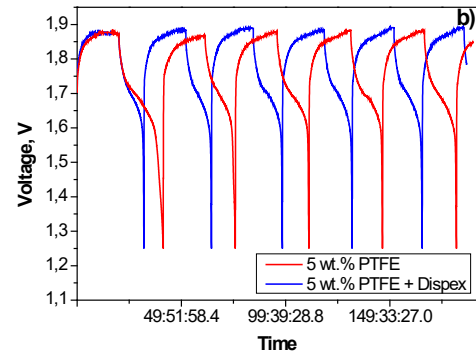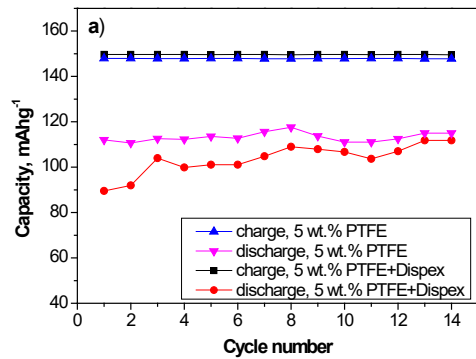
Fig. 6. Discharge capacity (a) and cell voltage profile for cells with and without Dispex surfactant (b)

130

At 50% DOD, short 30 sec. various current pulses were applied. Obtained voltage profiles were analyzed, where the first sharp voltage drop contributed to electrode ohmic resistance, while the second smooth drop represented the summary of all electrochemical overvoltage. The ohmic resistance for electrodes with and without surfactants was determined from the results obtained from 3 consecutive pulses at C/10, C/5 and C/2.

It seems that the use of surfactants reduces the electrode resistance to some degree, although such beneficial tendency was not clearly detected on our small-size electrodes. Probably, it will be better pronounced on larger-size electrodes and/or cells with more electrode pairs. However, as marked above, their use is increasing the electrode weight loss, and the potential beneficial effect will be forfeited with a short life expectancy.

Table 3 below summarizes the tested electrode compositions, while Figures 7 and 8 are showing the obtained discharge curves and, correspondingly, their efficiencies.

Table 3. Tested electrode compositions

Paste Compositions			
Composition 1 (K1)	Composition 2 (K2)	Composition 3 (K3)	Composition 4 (K4)
78 wt. % ZnO nanosized	78 wt. % ZnO nanosized	73 wt. % ZnO nanosized	73 wt. % ZnO nanosized
10 wt. % Zn	10 wt. % Zn	10 wt. % Zn	10 wt. % Zn
5 wt. % graphite	5 wt. % graphite	5 wt. % graphite	5 wt. % graphite
5 % PTFE	5 % PTFE	8 % PTFE	10 % PTFE
2 wt. % CMC, dissolved in H_2O	2 wt. % CMC, dissolved in 5% KOH	2 wt.% CMC, dissolved in H_2O	2 wt. % CMC, dissolved in H_2O
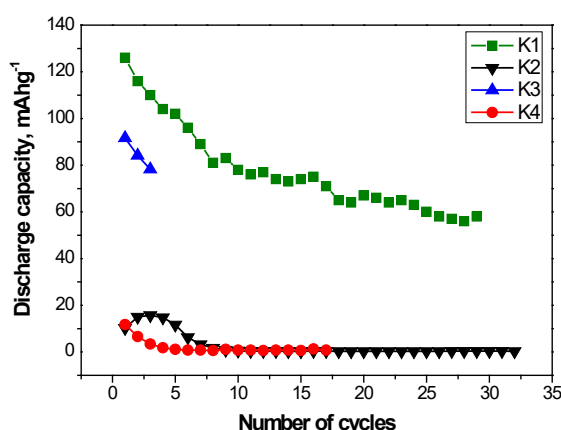
Fig. 7. Discharge capacities for electrodes prepared with the compositions shown in the table above
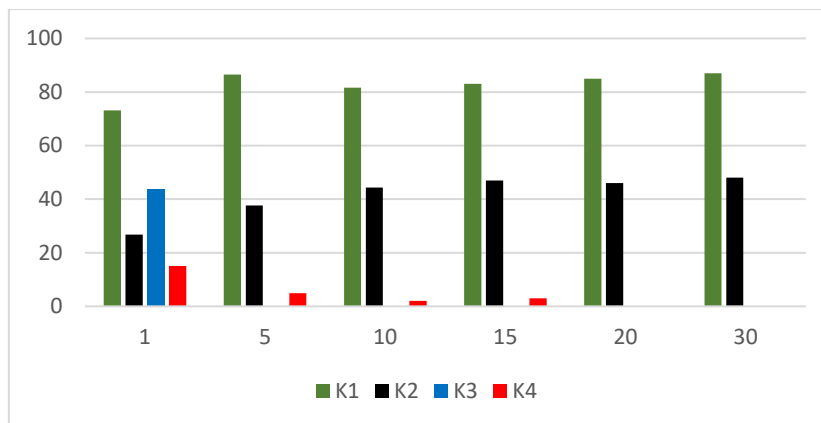
Fig. 8. Current efficiencies at C/10 for K1, K2, K3 and K4 at different charge/discharge cycles: $(I_{discharge}/I_{charge}) \times 100$, %

It was found that the best behavior in respect to current efficiency is exhibited by the paste K1. The obtained result confirms the significant influence of the binder on the working characteristics of the zinc electrode.

The use of surfactants in some cases can lead to negative effects, so their careful selection is necessary.

CONCLUSIONS

It could be concluded that the use of surfactants is reducing the electrode resistance to some degree, although such beneficial tendency was not clearly detected on our small-size electrodes. Probably, it will be better pronounced on larger-size electrodes and/or cells with more electrode pairs. However, as marked above, their use is increasing the electrode weight loss, and the potential beneficial effect will be forfeited with a short life expectancy.

It is necessary to continue the work in this direction with the use of other binders and surfactants. The application of gelled or membrane electrolytes can also result in limiting the formation of Zn dendrites and a corresponding extension of the cell lifetime, which will be investigated in the second part of this work.

REFERENCES

1. K. M. Tan, T. S. Babu, V. K. Ramachandaramurthy, P. Kasinathan, S. G. Solanki, S. K. G. Raveendran, *J. Energy Storage,* **39,** 102591 (2021).
2. M. J. B. Kabeyi, O. A. Olanrewaju, *Front. Energy Res.*, **9,** 743114 (2021).
3. T. K. A Hoang, L. Qin, T. Zhang, M. Zhou, J. Zhou, G. Fang, S. Liang, *Energy Stor. Mater.,* **34,** 545 (2021).
4. J. Zhou, L. Zhang, M. Peng, X. Zhou, Y. Cao, J. Liu, X. Shen, C. Yan, T. Qian, *Adv. Mater.*, **34,** 2200131 (2022).
5. https://en.wikipedia.org/wiki/Comparison_of_commercial_battery_types.
6. L. Panpan, J. Zhaoyu, X. Jin, *Energy Stor. Mater.,* **12,** 232 (2018).
7. Y. Shang, D. Kund, *Batteries Supercaps.,* **5,** e202100394 (2022).
8. R. E. F. Einerhand, W. Visscher, *J. Electrochem. Soc.*, **138,** 7 (1991).
9. F. R. McLarnon, E. J. Cairns, *J. Electrochem. Soc.*, **138,** 645 (1991)
10. Y. Zeng, Y. Meng, Z. Lai, X. Zhang, M. Yu, P. Fang, M. Wu, Y. Tong, X. Lu, *Adv. Mater.,* **44,** 29 (2017).
11. D. Squiller, R. Brody, *NSNTI Nanotech.,* **1,** 690 (2011).
12. M. Gong, Y. Li, H. Zhang, B. Zhang, W. Zhou, J. Feng, H. Wang, Y. Liang, Z. Fan, J. Liub, H. Dai, *Energy Environ. Sci.,* **7,** 2025 (2014).
13. Y. Liu, Y. Liu, Y, X. Wu, *Chem. Rec.*, **22,** e202200088 (2022).
14. K. Zhao, F. Liu, G. Fan, J. Liu, M. Yu, Z. Yan, N. Zhang, F. Cheng, *ACS Appl. Mater. Interfaces,* **13,** 47650 (2021).
15. J. Liu, C. Guan, C. Zhou, Z. Fan, Q. Ke, G. Zhang, C. Liu, J. Wang, *Adv. Mater.*, **28,** 8732 (2016).
16. F. Parker, C. N. Chervin, I. R. Pala, M. Mahler, M. F. Quick, J. Long, D. R. Rolison, *Science,* **356,** 415 (2017).
17. H.Wang T. R. Watkins, S. Simunovic, J. A. Turner, *ACS Nano,* **16,** 17139 (2022).
18. J. Li, N. Zhuang, J. Xie, Y. Zhu, H. Lai, W. Qin, *ACS Appl. Mater. Interfaces*, **11,** 15581 (2019).
19. Y. Li, Q. (Ray) Zeng, I. R. Gentle, D.-W. Wang, *J. Mater. Chem., A,* **5,** 5460 (2017).
20. M. A. Ramlli1, Yu K. X. Yu, Y. W. Siew, M. I. N. Isa, *ASM Sci. J., **Special Issue** 1,* 47 (2018).
21. Y. Nishi, S. Iizuka1, M. C. Faudree, R. Oyama, *Mater. Trans.*, **53,** 940 (2012).
22. C. Zhai, D. Zhao, Y. He, H. Huang, B. Chen, X. Wang, Z. Guo, *Batteries, 8,* 153, (2022).

Dielectric characterization (complex electric modulus) of Na^+-ion conducting PEO/E8/NaIO$_4$ salt-complexed polymer/liquid crystals composite

T. E. Vlakhov, Y. G. Marinov, G. B. Hadjichristov*

Georgi Nadjakov Institute of Solid State Physics, Bulgarian Academy of Sciences, 72 Tzarigradsko Chaussee Blvd., BG-1784 Sofia, Bulgaria

The frequency behavior (in the range 1 Hz – 1 MHz) of the complex electric modulus of flexible films (150 μm-thick) of Na^+-ion conducting composite electrolyte produced from polymer poly(ethylene oxide) (PEO), nematic liquid crystals E8 and the salt NaIO$_4$ (in compositional ratio PEO:E8:NaIO$_4$ = 63:27:10 wt%), was studied by electrochemical impedance spectroscopy. Relaxation characteristics for the polymer/liquid crystal PEO/E8/NaIO$_4$ composite were obtained, relevant to the applications of this ion-conducting dielectric material in flexible organic electronics and dielectric devices.

Keywords: flexible polymer electrolytes, liquid crystals, composites, Na^+-ion conducting polymer electrolytes, electrochemical impedance spectroscopy (EIS).

INTRODUCTION

Ion-transport solid and quasi-solid organic materials and electrolytes from polymers and liquid crystals (LCs) [1–5] are advanced materials that have an important role for the development of today's high-performance electrochemical and ionic devices, e.g., actuators, transducers, transistors, electrochromic devices, electrolyte membranes, as well as energy devices, such as batteries and capacitors, especially for flexible, portable and printed electronics [6–10]. Over the last decade, numerous studies have documented the use of ion transporters based on composites made from polymers and LCs, in particular ionic LCs [11–17]. Also, ion-conductor systems from polymers and nematic LCs (NLCs) have been developed and extensively studied [18–21] due to their important properties for practical use in flexible displays, flexible organic electronics and sensorics, solar-cell organic photovoltaics, as well as for rechargeable flexible mini-batteries and wearing electronics [22–25]. In this direction, the polymer poly(ethylene oxide) (PEO) and its derivatives were widely used as a polymer electrolyte matrix material for production of efficient ion-conducting systems [15, 26–29]. In particular, PEO-based sodium-ion (Na^+) conducting electrolytes were characterized with an easy processability and low cost, good electrochemical stability and compatibility with alkali salts, improved electrical properties and good ionic conductivity, which are vital for electrochemical and ionic devices [25, 30, 31].

Generally, the polymer/NLCs composites have attracted extensive research and application interest due to their unique electrical, dielectric, mechanical, and thermal properties [19, 20, 22, 23]. In addition, the blending of polymers with NLCs to produce ion-conducting electrolytes is considered as an effective method to modify also the properties of the polymers in such composites (e.g., the degree of crystallinity of the polymers), and thereby to enhance their ionic conductivity and other properties through intermolecular interaction between the polymers and NLCs [32]. This will be beneficial for future ionic device applications. Meanwhile, the selection of ion donor is paramount to enhance the ionic conductivity of the system. In this view, Na^+-based salts are found to give an excellent overall performance in terms of conductivity and stability, as the salts that contain Mg^{2+} ions. Furthermore, the use of Na ionic compounds can be an alternative to lithium-based salts (known to affect the environment). Our previous work reported a study of flexible films of Na^+-ion conducting composites from PEO with addition of molecules of the room-temperature NLCs with the commercial name E8 [32, 33]. Such ion-conductive electrolyte system attracted our attention because it exhibits ionic properties that are interesting for molecular electronics and soft-electronics applications. The structural and electrical conductivity investigations revealed an enhanced ionic and alternating-current (AC) conductivity, as well as other significant parameters, such as the amorphous and thermal properties of PEO/E8/NaIO$_4$ electrolyte films [32, 33], which contribute to their high performance, especially for future applications. Also, the effect of the molecules of E8 NLCs included in PEO/E8/NaIO$_4$ composites has been elucidated [32, 33]. Herein, the compositional ratio of the PEO/E8/NaIO$_4$ composite (w/w/w = 63/27/10

* To whom all correspondence should be sent:
E-mail: georgibh@issp.bas.bg

wt.%) was selected to be optimal due to the promising characteristics discussed earlier [32, 33]. Being of interest for the practical application of PEO/E8/NaIO₄ composite soft-solid dielectric materials, the present work is focusing on the study of their dielectric relaxation and ion conductivity relaxation in terms of (di)electric modulus, as depending on temperature. PEO/E8/NaIO₄ samples were characterized by means of electrochemical impedance spectroscopy in the frequency range 1 Hz – 1 MHz, in a room-temperature interval below their glass-transition temperature.

EXPERIMENTAL

Self-supported flexible films of the Na⁺-ion conducting polymer/LC PEO/E8/NaIO₄ composite were prepared with the aid of standard solution cast technique. Details to materials, preparation, and experimental procedures using complex electrical impedance spectroscopy (EIS), as well as the morphological features and structural properties of the PEO/E8/NaIO₄ polymer-salt complexed composite material are given elsewhere [32]. The room-temperature NLC material E8 (commercial name, Merck) is a multi-component mixture of four cyanobiphenyl compounds: pentyl-cyanobiphenyl (5CB) and cyano-alkoxy-biphenyls (nOCB; n = 3; 5; 8), as well as pentyl-cyanoterphenyl (5CT). The weight percentage of these compounds in E8 is: 5CB (46 wt.%): 3OCB (16 wt.%), 5OCB (12 wt.%); 8OCB (16 wt.%); 5CT 5OCB (11 wt.%). The compositional ratio in the PEO/E8 blend was PEO:E8 = 70:30 (wt.%). The salt sodium metaperiodate (NaIO₄) was included in the polymer blend at a concentration of 10 wt.%. The frequency spectra of the complex electrical impedance of the films were measured by electrical impedance-meter Bio-Logic SP–200. The PEO/E8/NaIO₄ films were placed between two blocking electrodes of copper (area = 0.75 cm²). The amplitude of the alternating-current (AC) voltage applied transversally to the films was 100 mV (sine function). The impedance spectra were recorded in the frequency range 1 Hz – 1 MHz. The measured impedance data has been transformed into electric modulus by using origin software. The temperature of the samples was maintained by a thermostat Mettler FP82 interfaced with a computer. The temperature accuracy was ± 0.1 °C. The impedimetric characteristics of the samples were obtained in the temperature range from 23 °C to 40 °C. This temperature interval is below the glass-transition temperature (42.5 °C) of PEO/E8/NaIO₄, as well as below the melting point (57.3 °C) for this composite [34]. The same applies

for the phase-transition temperature from nematic to isotropic state for E8 LC (72 °C) [35].

RESULTS AND DISCUSSION

The experimental data for the complex electrical impedance $Z^* = Z' + i\,Z''$ obtained by EIS technique [36, 37] consist of both real (Z') and imaginary (Z'') parts of Z^* simultaneously measured as a function of the frequency f of the AC electric field applied on the sample. Fig. 1 shows the variation of frequency spectra of Z' and Z'' impedances for a sample of the considered PEO/E8/NaIO₄ composite electrolyte film at various temperatures.
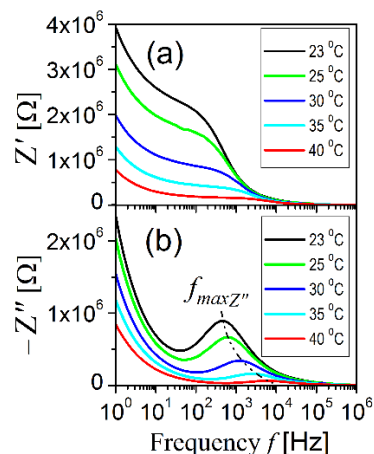
Fig. 1. Frequency-dependent real Z' (a) and imaginary Z'' (b) parts of complex electrical impedance of PEO/E8/NaIO₄ composite film at various temperatures.

The local maximum seen in $Z''(f)$ spectra (Fig. 1b) at frequency $f_{maxZ''}$ is related to the main dielectric relaxation in this dielectric material and is an indicator of its dipolar character. The shift of this maximum towards higher f is related to the increase of $f_{maxZ''}$ of the PEO/E8/NaIO₄ composite at elevating temperature. On the low-frequency side, the increase of the values of both Z' and Z'', seen at $f < 10$ Hz in our case, results from the well-known electrode polarization effect at the interface between the electrode and the sample. At low frequencies, this effect masks both electrical and dielectric properties of the studied dielectric material, in particular, the dielectric relaxation processes.

The ion conductivity relaxation in PEO/E8/NaIO₄ can be characterized with frequency spectra of complex (di)electric modulus (M^*) [38, 39]. By frequency spectra of M^* one can characterize the dielectric behavior and the conductivity relaxation of ion-conducting dielectric material. One advantage of modulus formalism is that in this way one can "unmask" the polarization effect from the bulk relaxation phenomenon at the interface between the electrode and dielectric sample (the above-mentioned effect from the electrode

interfacial polarization at low frequency), and thereby to observe the relaxation processes in a wide range of materials [38, 39].

Electric modulus M^* is defined as $M^* = 1/\varepsilon^*$, where ε^* is the complex dielectric permittivity function. The real (M') and imaginary (M'') parts of M^* are defined through the real (ε') and imaginary (ε'') parts of ε^* by expressions [38, 39]:

$$M' = \frac{\varepsilon'}{\varepsilon'^2 + \varepsilon''^2} \quad \text{and}$$

$$M'' = \frac{\varepsilon''}{\varepsilon'^2 + \varepsilon''^2} \quad (1)$$

The complex impedance (Z^*) data can be transformed into complex electric modulus data, by using expressions [36]:

$$M' = -\frac{2\pi f \, \varepsilon_0 A}{l} Z'' \quad \text{and}$$

$$M'' = \frac{2\pi f \, \varepsilon_0 A}{l} Z' \quad (2)$$

where ε_0 is the vacuum permittivity. In our case, $l = 150$ μm was the thickness of the film and $A = 0.75$ cm² was the contact area of the copper electrodes.

Fig. 2 presents the plots of the variation of the values of M' and M'' as a function of frequency at several temperatures, as calculated for the studied PEO/E8/NaIO₄ films by Eqs. (2). At low frequency, the modulus values approach zero at all temperature values indicating the effect of the electrode polarization phenomena. The lower values of the modulus result from enhanced capacitance. The relatively high value of capacitance is ascribed to the effective double layer charges building up at the interfacial region close to the blocking electrodes of the studied PEO/E8/NaIO₄ films. It is noticed in Fig. 2 (a) that the M' value continuously increases with the increase of frequency f in the range 1 Hz – 1 MHz and tends to saturate for higher frequencies. Such frequency-dependent behavior also takes place in the $M''(f)$ spectra (Fig. 2 b). In these plots, however, a peak is present, observed at a relatively high frequency $f_{max} \geq 100$ kHz (Fig. 2 b). This peak corresponds to a relaxation process and it is assigned to conductivity relaxation mechanism [38, 39]. The most probable conductivity relaxation time τ can be expressed as $\tau = 1/2\pi f_{max}$ [38, 39]. τ can be considered as the average time needed for the ions to transfer from a site to another site during the conduction process (in our case – ion hopping between ion coordination sites). The conductivity relaxation phenomenon is related to the lack of restoring force governing the mobility of charge carriers under the influence of an electric field [40]. This is attributed

to conduction due to the short-range mobility of charge carriers.

As seen from Fig. 2 (b), on increasing temperature of the PEO/E8/NaIO₄ composite, the M'' peak at f_R shifts to higher frequencies. This signifies the faster movement of the mobile carriers of charge, in our case – the conducting ions (Na⁺). The shifting of the peak in the M'' plots to higher frequency indicates that the relaxation time of the ions decreases as the temperature is raised. Such behavior is consistent with the enhanced polymer segmental motion at elevating temperature [41, 42]. Thus, the observed frequency shift of the M'' peak is directly related to the increase of ionic mobility and the increase of ionic conductivity, reported for the same PEO/E8/NaIO₄ composite on increasing temperature in the same range (23 – 40 °C) examined here [32]. The observed broadening of the relaxation peak in the $M''(f)$ spectra (Fig. 2 b) and its asymmetry are related to the spread of relaxation time. Such a broad nature of the peak can be interpreted as a consequence of the distribution of relaxation times τ and is an indication of the non-Debye type of relaxation behavior for the studied PEO/E8/NaIO₄ ion-conducting dielectric material.

Conductivity relaxation process that is characterized with a high relaxation frequency f_{max} at room temperature is a valuable property. This means that the dielectric material, in our case PEO/E8/NaIO₄ composite, is characterized with a fast ion migration up to this value of the frequency f_{max}.
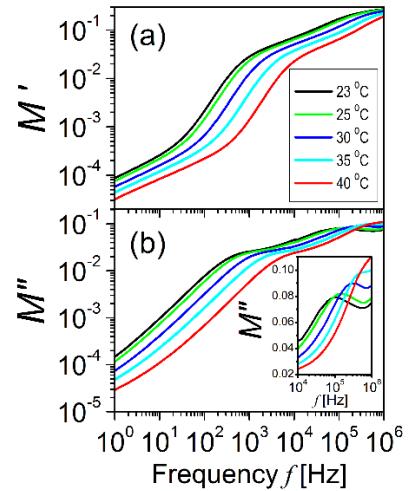
Fig. 2. Frequency spectra of: (a) real part (M'); (b) imaginary part (M'') of the complex electric modulus calculated for the studied PEO/E8/NaIO₄ composite film at various temperatures. Inset in (b): expanded view (10^4 – 10^6 Hz frequency range) for M'' in a linear scale.

Actually, of importance are two facts: (i) the relaxation frequency f_{max} of the ion conductivity of the studied electrolyte system is high (close to the

MHz range), and (ii) f_{max} becomes even higher with increasing temperature, i.e., under the same condition when both ion conductivity and dielectric properties of this composite are also improved [32]. Fig. 3 presents the cross-frequency (f_{cross}) characteristics of the electric modulus, i.e., the frequency at which M' is equal to M'', i.e., at f_{cross} Z' = Z''. It is noted that by increasing temperature, f_{cross} is increased (Fig. 3), like the frequency $f_{maxZ''}$ (Fig. 1

b). In both cases, this implies a dipolar character of the molecular interaction (dipole–dipole interaction) and a typical effect due to dipole relaxation as a result of heating of the PEO/E8/NaIO$_4$ polymer-based composite [41, 43]. By heating, a softening of the polymer PEO occurs, and thereby, the segmental motion of the polymer chains is enhanced. This leads to an increased relaxation frequency of PEO/E8/NaIO$_4$ flexible polymer/NLCs composite.
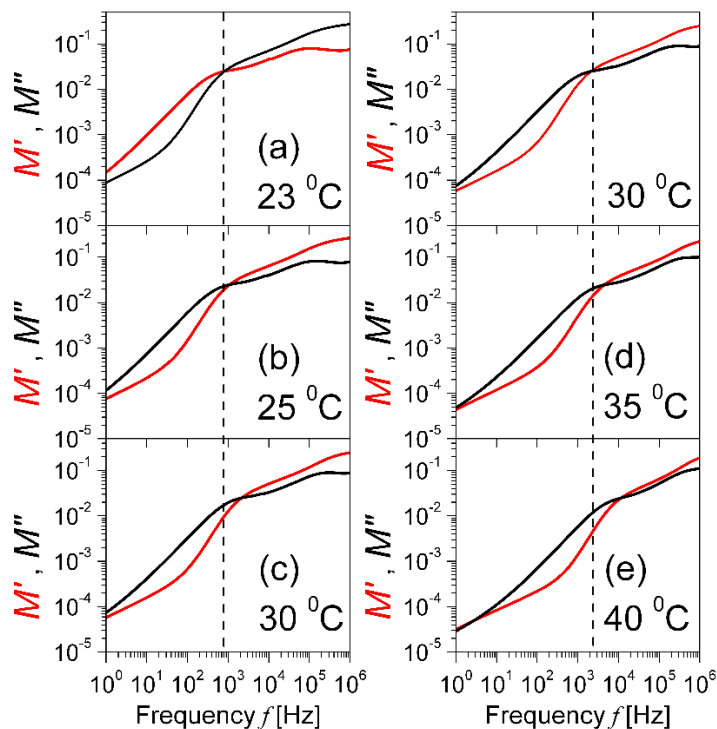
Fig. 3. The pairs of M' (red lines) and M'' (black lines) frequency spectra for PEO/E8/NaIO$_4$ composite at various temperatures (data from Fig. 2).
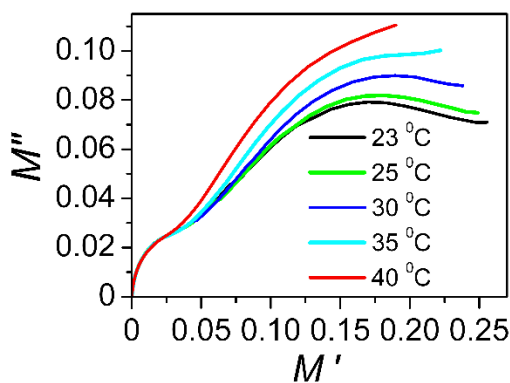
Fig. 4. M'' *vs* M' plots for the studied PEO/E8/NaIO$_4$ composite film.

Further, Argand (M'' *vs.* M') plots could be also used to characterize the mechanism of the relaxation dynamics. In our case, these plots do not exhibit a single semicircle (corresponding to a single relaxation) (Fig. 4) and this feature is due to the presence of two components in the composite –E8 LC and PEO. The results shown in Fig. 4 suggest

that the almost non-dependent on temperature semicircle-like behaviors with a smaller diameter can be attributed to E8 LC, whereas the semicircular behaviors with a larger diameter correspond to the contribution of the polymer (PEO). The semicircles present for the Argand curves (above 35 °C they tend to form incomplete circles) reveal that the relaxation dynamics is due to conductivity relaxation. As such, the Argand curves calculated for PEO/E8/NaIO$_4$ significantly differ from the shapes (distorted arcs) typical for the relaxation mechanism corresponding to viscoelastic relaxation processes (or polymer molecular relaxation) found in multi-phase polymer-based systems and electrolytes [44, 45]. Commonly, a presence of a sharp peak in the M'' frequency spectrum accounts for the conductivity relaxation, whereas the viscoelastic relaxations typical for polymers are associated with a broad distribution of relaxation times [46]. Both types of relaxation in the studied PEO/E8/NaIO$_4$ composite are related to the

segmental motion of the main chain of the polymer (PEO), and the ion conductivity relaxation time τ decreases by increasing temperature in the same way as the viscosity. In our case, the results obtained by the M^* representations in Figs. 2 and 4 show that the conductivity relaxation as a factor determining the relaxation dynamics and ion transport properties of the studied PEO/E8/NaIO$_4$ composites is more important than the viscosity of the host polymer PEO.

CONCLUSIONS

The complex electric modulus of films of PEO/E8/NaIO$_4$ polymer/NLCs composite electrolyte system was studied to characterize the dielectric relaxation and ion conductivity relaxation in this flexible Na$^+$-ion conductor, examined by complex electrical impedance spectroscopy. The relaxation features (peaks) that occur in the imaginary parts of both electrical impedance (Z'') and electric modulus (M'') indicate the presence of orientation dipoles in PEO/E8/NaIO$_4$, which support the fast ion conduction. From frequency-domain electric modulus study the ion conductivity relaxation in PEO/E8/NaIO$_4$ can be deduced that has an important role for the ion transport. The ion conductivity relaxation is strongly influenced by the contribution of the polymer segmental relaxation in this polymer/NLCs composite system. The variation of the complex electric modulus with temperature and the increase of the relaxation frequency with the temperature, are ascribed to the enhanced polymer chain flexibility and corresponding increased ion mobility with temperature. The frequency spectra of the imaginary modulus $M''(f)$ used as an indicator of ion conductivity relaxation in PEO/E8/NaIO$_4$ composite, indicate that a quick response with a high ionic mobility can be achieved by this ion electrolyte. The results reported here show that the examined ion-conducting dielectric material is promising for ion electrolyte applications in flexible organic electronics and for use in dielectric devices. Moreover, the polymer/NLCs system considered here makes possible the employment of the unique properties of NLCs upon electro-magnetic fields (work in progress).

REFERENCES

1. T. Kato, *Angew. Chem. Int. Ed.*, **49**, 7847 (2010).
2. V. K. Thakur, G. Ding, J. Ma, P. S. Lee, X. Lu, *Adv. Mater.*, **24**, 4071 (2012).
3. B. R. Wiesenauer, D. L. Gin, *Polym. J.*, **44**, 461 (2012).
4. J. Sakuda, E. Hosono, M. Yoshio, T. Ichikawa, T. Matsumoto, H. Ohno, H. Zhou, T. Kato, *Adv. Funct. Mater.*, **25**, 1206 (2015).
5. T. Kato, M. Yoshio, T. Ichikawa, B. Soberats, H. Ohno, M. Funahashi, *Nat. Rev. Mater.*, **2**, 17001 (2017).
6. A. J. Duncan, D. J. Leo, T. E. Long, *Macromolecules*, **41**, 7765 (2008).
7. S. H. Kim, K. Hong, W. Xie, K. H. Lee, S. Zhang, T. P. Lodge, C. D. Frisbie, *Adv. Mater.*, **25**, 1822 (2013).
8. X. Lu, M. Yu, G. Wang, Y. Tong, Y. Li, *Energy Environ. Sci.*, **7**, 2160 (2014).
9. I. Osada, H. De Vries, B. Scrosati, S. Passerini, *Angew. Chem. Int. Ed.*, **55**, 500 (2016).
10. H. Kokubo, R. Sano, K. Murai, S. Ishii, M. Watanabe, *Eur. Polym. J.*, **106**, 266 (2018).
11. M. Yoshio, T. Kato, in: Handbook of Liquid Crystals, J. W. Goodby, P. J. Collings, T. Kato, C. Tschierske, H. Gleeson, P. Raynes (eds.), Wiley-VCH, Weinheim, 2014, p. 727.
12. R. Sasi, S. Sarojam, S. J. Devaki, *ACS Sustainable Chem. Eng.*, **4**, 3535 (2016).
13. R. Sasi, B. Chandrasekhar, N. Kalaiselvi, S. J. Devaki, *Adv. Sustainable Syst.*, **1**, 1600031 (2017).
14. S. Wang, X. Liu, A. Wang, Z. Wang, J. Chen, Q. Zeng, X. Wang, L. Zhang, *Polym. Chem.*, **9**, 4674 (2018).
15. M. Zhang, A. Zhang, Q. Li, F. Li, S. Wang, S. Li, *J. Polym. Environ.*, **27**, 2369 (2019).
16. X. Chen, Y. Xie, Y. Ling, J. Zhao, Y. Xu, Y. Tong, S. Li, Y. Wang, *Mater. Design*, **192**, 108760 (2020).
17. Q. Zeng, Y. Lua, P. Chen, Z. Li, X. Wen, W. Wen, Y. Liu, S. Zhang, H. Zhao, H. Zhou, Z. X. Wang, L. Zhang, *J. Energy Chem.*, **67**, 157 (2022).
18. A. Z. S. B. Zulkifli, M. A. B. Kamarudin, A. B. Mainal, S. B. M. Said, *Adv. Mater. Res.*, **895**, 142 (2014).
19. S. M. Said, A. Z. S. Zulkifli, M. A. Kamarudin, A. Mainal, B. Subramanian, N. S. Mohamed, *Europ. Polym. J.*, **66**, 266 (2015).
20. S. M. Said, S. R. Sahamir, M. F. M. Sabri, M. A. Kamarudin, K. Hayashi, A. Z. S. Zulkifli, T. Nakajo, M. Kubouchi, Y. Miyazaki, *Molec. Cryst. Liq. Cryst.*, **642**, 9 (2017).
21. M. A. Kamarudin, A. A. Khan, S. M. Said, M. M. Qasim, T. D. Wilkinson, *Liq. Cryst.*, **45**, 112 (2018).
22. S. C. Kim, M. Song, T. I. Ryu, M. J. Lee, S.-H. Jin, Y.-S. Gal, H.-K. Kim, G.-D. Lee, Y. S. Kang, *Macromolec. Chem. Phys.*, **210**, 1844 (2009).

23. M. A. Karim, M. Song, J. S. Park, Y. H. Kim, M. J. Lee, J. W. Lee, C. W. Lee, Y. R. Cho, Y. S. Gal, J. H. Lee, S. H. Jin, *Dye Pigments*, **86**, 259 (2010).
24. M. A. A. Kamarudin, A. A. Khan, M. M. Qasim, T. D. Wilkinson, *Proc. SPIE,* **9940**, 994010 (2016).
25. H. K. Koduru, Y. G. Marinov, G. B. Hadjichristov, N. Scaramuzza, *Solid State Ionics*, **335**, 86 (2019).
26. J. Li, K. Kamata, M. Komura, T. Yamada, H. Yoshida, T. Iyoda, *Macromolecules*, **40**, 8125 (2007).
27. Y. Tong, L. Chen, X. He, Y. Chen, *Electrochim. Acta*, **118**, 33 (2014).
28. S. Wang, Q. Zeng, A. Wang, X. Liu, J. Chen, Z. Wang, L. Zhang, *J. Mater. Chem. A*, **7**, 1069 (2019).
29. J. D. Hwang, P. Y. Chen, S. W. Ding, C. W. Ong, *Crystals*, **9**, 627 (2019).
30. H. K. Koduru, L. Marino, F. Scarpelli, A. G. Petrov, Y. G. Marinov, G. B. Hadjichristov, M. T. Iliev, N. Scaramuzza, *Curr. Appl. Phys.*, **17**, 1518 (2017).
31. G. B. Hadjichristov, Tz. E. Ivanov, Y. G. Marinov, H. K. Koduru, N. Scaramuzza, *Phys. Status Solidi (A): Appl. Mater. Sci.*, **216**, 1800739 (2019).
32. G. B. Hadjichristov, Y. G. Marinov, Tz. E. Ivanov, H. K. Koduru, N. Scaramuzza, in: Liquid and Single Crystals: Properties, Manufacturing and Uses, J. Goosen (ed.), Nova Science Publ., New York, 2020, p. 1.
33. G. Hadjichristov, Y. Marinov, A. Petrov, H. Koduru, N. Scaramuzza, *J. Phys. Conf. Ser.,* **1186**, 012020 (2019).
34. H. K. Koduru, Y. G. Marinov, F. Scarpelli, G. B. Hadjichristov, A. G. Petrov, N. Godbert, N. Scaramuzza, *J. Non-Crystal. Solids*, **499**, 107 (2018).
35. B. Bahadur, R. K. Sarna, V. G. Bhide, *Mol. Cryst. Liq. Cryst.*, **72**, 139 (1982).
36. V. F. Lvovich, Impedance Spectroscopy: Applications to Electrochemical and Dielectric Phenomena, John Wiley & Sons, Inc., Hoboken, 2012.
37. E. Barsoukov, J. R. Macdonald, Impedance Spectroscopy: Theory, Experiment, and Applications, Wiley, Hoboken, 2005.
38. P. B. Macedo, C. T. Moynihan, R. Bose, *Phys. Chem. Glasses*, **13**, 171 (1972).
39. A. K Jonscher, *J. Phys. D: Appl. Phys.*, **32,** R57 (1999).
40. I. M. Hodge, K. L. Ngai, C. T. Moynihan, *J. Non-Cryst. Solids*, **351**, 104 (2005).
41. C. H. Chan, H. W. Kammer, *Polymers*, **12**, 1009 (2020).
42. G. Polizos, E. Tuncer, V. Tomer, I. Sauers, C. A. Randall, E. Manias, in: Nanoscale Spectroscopy with Applications, S. M. Musa (ed.), CRC Press, Boca Raton, 2013, p. 93.
43. C. H. Chan, H. W. Kammer, *Pure Appl. Chem.*, **90**, 939 (2018).
44. A. S. Ayesh, *Chin. J. Polym. Sci.*, **28**, 537 (2010).
45. S. B. Aziz, W. O. Karim, M. A. Brza, R. T. Abdulwahid, S. R. Saeed, S. Al-Zangana, M. F. Z. Kadir, *Int. J. Mol. Sci.*, **20**, 5265 (2019).
46. K. Mohomed, T. G. Gerasimov, F. Moussy, J. P. Harmon, *Polymer*, **46**, 3847 (2005).

SNCR in biomass combustion facilities: from theories to existing models

N. M. Petrov[1*], M. R. Mladenović[1], N. R. Rudonja[2]

[1]*University of Belgrade, Vinča Institute of Nuclear Sciences, National Institute of the Republic Serbia, Laboratory of Thermal Engineering and Energy, Mihaila Petrovića Alasa Str. 12-14, 11351 Belgrade, Serbia*
[2]*University of Belgrade, Faculty of Mechanical Engineering, Kraljice Marije Str. 16, 11120 Belgrade, Serbia*

With the significant use of biomass for energy purposes, as the only CO_2-neutral carbon-based renewable energy source, besides several well-known advantages, certain disadvantages appear. One of them is the possible increased emission of nitrogen oxides, NOx, which is especially pronounced with the usage of agricultural biomass. Given the available resources of this biomass and increasingly stringent legal norms regarding NOx emissions, this problem needs special attention, which is the topic of this paper. The paper presents: mechanisms of NOx formation and conversion of nitrogen from fuel during combustion, a brief overview of available methods for denitrification, both conventional and newer ones that have not yet come to industrial-scale application. NOx emissions from biomass combustion are mainly caused by fuel-bound nitrogen, which is especially present in biomass with a high content of bound nitrogen such as agricultural biomass. Therefore, the focus is on selective non-catalytic reduction, SNCR, as a secondary measure of denitrification. Theoretical bases of SNCR, presentation of SNCR reagents, main pathways of chemical reduction reactions for different reagents, and reaction kinetics are given. Also, the general bases for setting numerical SNCR reduction models and reviewing existing ones, as well as experimental results from the available literature, are presented. Finally, examples of industrial applications of SNCR reactors and general recommendations for the application of this denitrification measure are introduced.

Keywords: SNCR, biomass combustion, NOx

INTRODUCTION

After the industrial revolution and the damages caused by the use of fossil fuels, the humanity is facing various challenges associated with sustainable development, the transition to green energy sources, as well as reducing greenhouse gas emissions and planning the formation of self-sustaining cities. When choosing an energy source, one of the main conditions is that it is possible to respond to consumer demands throughout the year. From the point of view of sustainable development, the residues from agriculture are especially significant. In order to work on the introduction of biomass in the energy sector, it is necessary to observe the shortcomings that come with it in time. An inseparable problem related to the biomass combustion is the emission of nitrogen oxides NOx (nitrogen monoxide (NO) almost 90%, and nitrogen dioxide (NO_2) <10%), which have extremely negative effects on human health and the environment in general [1, 2]. Due to combustion conditions, the predominant influence on the mechanisms of NOx formation, which are thermal, prompt and fuel-N, has the last one, which refers to the oxidation of nitrogen bound in the fuel [3]. Since fuel-N mechanism mostly depends on the fuel composition, and not optimal combustion conditions

it is not possible to reduce NOx emissions without secondary denitrification measures [4]. Various technologies have already been developed and many are still being researched. Neither of them can be singled out as the best so the selection should be made according to techno-economic analysis which should provide the highest efficiency with the lowest cost. Selective non-catalytic reduction (SNCR) is considered as a possible solution to all of the previously mentioned problems. One of the advantages of SNCR is that it can be easily combined with other denitrification measures. For a tecnology to be well understood, a comperhensive approach is needed, from the initial theory to the implementation in reality. This paper presents a concise guide through SNCR denitrification method, and refers to the NOx formation during biomass combustion, comparision of SNCR with the other methods, influential parameters based on theoretical and experimental studies, detailed chemical mechanisms, numerical modeling, as well as the challenges associated with them.

METHODS

SNCR-associated studies that meet the inclusion criteria are observed. The first requirement concerns the type of fuel – biomass with high nitrogen content. This refers to flue gas from the combustion

---

of biomass or synthetic gas, which should correspond to the composition of flue gases in biomass. Alongside that, thermal and prompt mechanisms of NOx formation are neglected. They are not significantly expressed in biomass because of the relatively low combustion temperature due to the low melting temperature of biomass ash [5]. By observing the temperature range of biomass combustion, it was decided to consider ammonia and urea as reducing agents. A selection of concepts and ideas that are important for a comprehensive understanding and analysis of SNCR has been made. Based on them, previous research has been classified into sections that can be considered necessary steps for the introduction of SNCR measure into the energy and industrial sector. To make the review comprehensive, not only the latest studies were included.

RESULTS AND DISCUSSION

Firstly, it is necessary to understand the conversion of nitrogen during biomass combustion and NOx formation, which is explained in the first section. After that, it is significant to consider comparing SNCR technology with other denitrification measures that are available and under development. Afterward, it is possible to dedicate to the fundamental theoretical knowledge and the most influential parameters of the SNCR. That also includes conclusions obtained from experimental research. The following sections refer to detailed chemical mechanisms and numerical modeling of the reduction process. For each section, the fundamental principles established so far, current issues, as well as the next steps needed for further development of the SNCR, are observed. Finally, the emission of nitrogen oxides from real-scale biomass combustion systems is presented, with and without SNCR measure, which shows the reduction in reality. That together provides the necessary prior knowledge for monitoring the application of SNCR in plants, predicting NOx emissions, along with compliance with existing legislation.

Conversion of nitrogen from fuel (fuel-N) during biomass combustion (N paths)

To solve the NOx emission problem, first, it is necessary to understand the process of NOx formation during biomass combustion. Depending on the fraction of volatiles and char (whose fraction in the fuel can go up to 30% [6, 7]), significant deviations in the process can occur. Besides the fraction of volatiles and char, important parameters are also temperature, time of the combustion process, and size of the particles that are burned. In

addition to the previous parameters, the influence and presence of H_2O, ash, and various compounds that appear in the fuel composition are considered. Nitrogen conversion during combustion is differentiated by combustion phases, although in reality, these phases overlap [8, 9]. Fig. 1. shows a schematic diagram of the nitrogen conversion pathway in biomass combustion, from the main forms in the fuel (mostly proteins) [10, 11], to the combustion chemical species and nitrogen remaining in the ash.
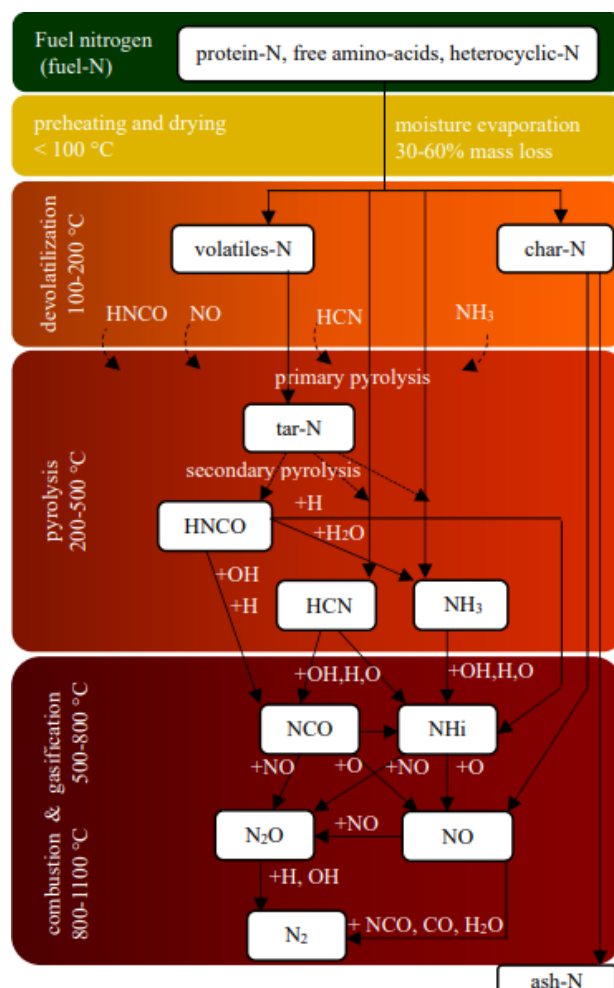
Fig. 1. Conversion of fuel-N (biomass combustion)

NOx formation is not uniform during biomass particle combustion. Two peaks occur, one due to the volatile-N [4] and the other due to the char. Amongst the chemical species that can be found during biomass combustion, it is important to single out NH_3 and HCN, which have a crucial role in the formation of NOx [12, 13]. The majority of them are formed during the tar cracking in the secondary pyrolysis [10]. The ratio of these precursors depends on the operating conditions of the process and the type of combustion - a difference can be noticed when observing the combustion of individual biomass particles compared to the combustion in the

real system. It was found that when the initial nitrogen content increases, both the HCN / NH$_3$ ratio and the temperature decrease [14]. The content of HNCO should also be considered; even though it is present in a smaller amount, it still contributes to the formation of NOx [15, 16].

The process of NOx reduction is highly affected by the char structure [17] and the presence of ash which can have a catalytic effect on NOx reduction. This is especially important in agricultural residues with a high content of CaO / alkali oxides [5]. Out of all nitrogen conversion pathways, volatiles have a dominant influence, and the possibility of predicting NOx formation from them is particularly significant [18–20].

Comparison of deNOx measures

This section aims to give an objective comparison of the available measures that correspond to the temperature range of biomass combustion. According to various authors, denitrification methods can be classified as pre-combustion, combustion-control, and post-combustion methods (flue gas treatment). Combustion-control (primary measures) refers to a modification of the combustion process or operating conditions on existing furnaces without the use of additional pollution abatement equipment behind the main combustion zone. Modifications of the biomass combustion process refer to air and fuel staging, flue gas recirculation, and low-NOx burner. Strategies for modification of operating conditions that can be applied during biomass combustion are reduction of oxygen concentrations in the combustion zone and improving mixing conditions [21–23]. Pre-combustion and combustion control methods at agricultural biomass combustion often do not provide reduction below emission standards so post-combustion methods are necessary. In Table 1 a comparison of measures is given. Further research of deNOx and optimization of described methods, to overcome the NOx emission problem is required. Application of these methods in commercial use and increasing their efficiency, while solving cost and methods disadvantages, is key for biomass to be used as a renewable energy source and fossil fuel replacement.

SNCR in brief

Selective non-catalytic reduction (SNCR) is based on a chemical reduction of NOx, which occurs when it is injected into a stream of hot flue gas. In the reaction of the agent with flue gas, NOx are being converted into N$_2$ and H$_2$O vapor (and CO if urea is used). NOx reduction is achieved due to high temperatures, at which the agent tends to react with NOx rather than with other components from flue gas, hence the name selective non-catalytic reduction. The absence of catalysts and all problems related to it is a great advantage of this deNOx method. In principle, the reduction process takes place due to chain reactions maintained by free radicals, which are provided by reduction agents. It has already been mentioned that during nitrogen conversion during combustion, the formed NOx can be partially reduced to N$_2$, which can be seen in Fig. 1. The goal is to increase the concentration of free radical-producing compounds that are essential for NOx reduction, within a temperature range that provides selectivity so that the reduction is not replaced by further NOx formation. Ammonium and urea as reducing agents are effective at high temperatures due to their decomposition to NH$_2$ which is further explained in the section *Detailed chemical mechanism*.

1. Comparison of reducing agents.

Ammonia and urea are known as reducing agents for biomass. Some studies consider the possibility of other agents, i.e. methane [24], hydrazine hydrate, urea-spiked hydrazine [25], and cyanuric acid–RapDeNOx, but they are considered less effective for NOx reduction during biomass combustion. Also, the use of methane is not suitable because it increases the CO emission. Advantage of using ammonia is lower cost, compared to urea. On the other hand, urea is environmentally and health friendly, and its storage is easier. If urea is used, there is a possible increase in the harmful N$_2$O emissions [26].

2. Understanding of SNCR based on theoretical and experimental studies.

It is important to consider the most influential parameters for SNCR and the possibility of the appearance of by-products, such as N$_2$O, ammonia slip, ammonium sulfate salts, as well as the increase in CO emissions. The efficiency of the method is significantly influenced by the type of agent used, the amount and composition of the additive, the temperature, the residence time, the molar fraction of agent/NO, as well as the oxygen concentration in the flue gases [27].

The temperature range in which the SNCR method can be applied depends on the used reducing agent. For ammonia, the recommended temperature range is 1123-1273 K, and for urea is 1023-1323 K

Table 1. Review of denitrification methods alongside with their main advantages and disadvantages

	Combustion control	SCR	SNCR	Wet scrubbing	Electron beam	Electrochemical method	Non-thermal plasma
Efficiency [%]	<80[1] [23]	60-90 [5]	30-70 [5]	96[2] [27]	82[3] [28]	60[4] [29]	14-96[4] [27]
Temp. range [°C]	Optimal for combustion	150-590 [5]	800-1100 [5]	Ambient temp. [27]	90[3] [28]	400[4] [29]	200[4] [27]
Advantages	Mature technology, Modification of the combustion process/ operating conditions on existing furnaces, without the use of additional pollution abatement equipment behind the main combustion zone	High efficiency, Good selectivity, Cost effectiveness, Relatively simple system, Mature technology	No waste generation, Simple solution, Easy implementation on existing combustion systems, Lower cost, Can be combined with other deNOx methods, Mature technology	Simultaneous deNOx and deSOx , PM and acid gases control, No high temperatures , No extraneous chemicals, Easy regeneration, Low cost of equipment and additives, Mature technology	Simultaneous deNOx and deSOx, No waste generation, By-product can be used for fertilizer production	Reductant is not required,	Simple system and operation, No waste generated, By-product are useful, Low cost of equipment
Disadvantages	Low efficiency, They are not enough for flue gas cleaning	High cost of catalyst, Lifespan and disposal of catalyst, Storage of reducing agents, High cost and corrosion of equipment, Ammonia slip	Less reduction ration, Downstream equipment cleaning is necessary, High operating temperatures, Ammonia slip	Slow removal rate, Low efficiency, Liquid waste	High energy consumption, Prevention of radiation problems, Complex equipment, Not tested in real-scale systems	Still not developed and implemented in real-scale systems	Low efficiency, High energy consumption and cost, Operating pressure is low
Reference	[21,22,30]	[27,31–33]	[5,26,27,34]	[35,36]	[27,28]	[27,29]	[37,38]

[1]depends on inlet NOx concentracion, for industrial appliences high efficiency is not achiavable so secondary measures are neccesary

[2] for temperature 70°C with urea solution, lab experiment

[3]for simultanious NOx and SOx reduction in lab experiment for liquid fuels

[4]lab experiments

Higher temperatures during the SNCR cause the decomposition of the reducing agent which leads to a decrease in the NOx reduction. If temperatures are below the recommended, NH_2 radicals do not react with NOx since the rate of reaction is slower. Also, during the reduction, the opposite effect from expected may occur if NH_2 radicals react with oxygen, which would result in the further NOx formation [5].

Residence time has a very significant impact on the NOx reduction when the SNCR method is applied. The time required depends on the available temperature range. The maximum reduction is achieved by complete mixing of the reducing agent with the flue gases at the optimum temperature. The required residence time also depends on the flue gases velocity, their composition, as well as the construction of the furnace. The order of magnitude of the residence time for SNCR chemistry is a few seconds.

The implemented injection method affects the mixing effect. A normalized stoichiometric ratio (NSR) is an indicator of the injected optimal flow of the reducing agent. By optimizing the NSR, the maximum reduction is achieved, and the possibility of a part of the agent not reacting (emission into the atmosphere) is avoided (environmental impact and technology efficiency are minimized). To properly implement SNCR, it is necessary to take into account the choice of reducing agent injection site and the achievement of good mixing conditions. The effect of mixing is particularly significant at higher temperatures, at the upper limit of the SNCR range [28]. To overcome obstacles of nonuniform

distribution and poor mixing in industrial plants, injection is performed at several levels and in several places along the cross-section of the furnace (this is especially necessary for larger industrial furnaces, due to frequent temperature fluctuations in height and cross-section of the furnace) [31]).

The use of additives, i.e. enhancers can significantly contribute to NOx reduction. In addition to the direct influence on the reduction efficiency, it can also lower the necessary temperature range for the SNCR application. The influence of additives is achieved due to the radicals they provide. This initiates chemical NOx reduction reactions. Additives can reduce harmful flue gas components. To be properly applied, it is necessary to observe the temperature range in which the additives have the desired effect. At temperatures below the optimum, additional compounds may be formed which are undesirable. Besides, it can occur that part of the additive does not participate in the process and as a result is emitted into the atmosphere. On the other hand, at higher temperatures, very fast reactions not related to NOx may happen. Additives of interest to SNCR are CO, H_2, CH_4, various combinations of hydrocarbons, alcohol additives (CH_3OH, C_2H_5OH), and sodium compounds ($NaOH$, Na_2CO_3) [29]. The presence of HCl can cause a decrease in the temperature range needed for SNCR, but its presence is only favorable at temperatures below 1173 K, because otherwise, it can cause an increase in NO formation [30].

3. Major challenges for SNCR application.

The most important challenge for SNCR implementation is to place the reducing agent where it is most effective in the furnace. The variations in operating conditions and furnace loads must be considered, meaning it must be injected in an appropriate temperature range, given that the temperature of flue gases varies both by cross-section and the furnace height. Viewed by cross-section, a higher amount of reducing agent must find its way to the furnace center where more NOx can be found and compared to the cooler walls. Otherwise, NO in the center meets insufficient ammonia for reduction and excess NH_3 near the walls slips through (ammonia slip) affecting furnace's downstream equipment. Also, the flue gas temperature varies by height caused by changes in the furnace load or calorific value of the fuel (which is particularly important for biomass use). This may also result in increased deposits thickness on the heating surfaces, etc. At low-load operation optimum SNCR temperature region shifts within the lower part of the furnace, and *vice versa*. To overcome uneven temperature distribution and imbalances from the furnace load changes, it is necessary to predict more reducing agent injection points by furnace's cross-section and levels. The presence of water has a positive effect on reducing NOx emissions and direct injection into the flue gas stream can be performed. On the contrary, an increase in the H_2O concentration can lead to an increase in the NO content due to the higher conversion of NO to NO_2. Oxygen concentration has a significant effect on the possibility of NOx reduction. When increasing the concentration of O_2 from 4% to 21%, at a temperature of 800°C there is a decrease in the NOx reduction, because at high oxygen concentrations more ammonia is oxidized, which consequently leads to greater NO formation [31]. Simultaneous regulation of the emission of carbon monoxide, carbon dioxide, hydrocarbon compounds, and nitrogen oxides presents a great challenge. In SNCR carbon monoxide affects the NO reduction regime by shifting the temperature range for reduction to lower temperatures. In addition, there is a narrowing of the range in which it is possible to achieve a NO reduction, because of the increased amount of radical levels, the reverse process is created. Therefore, there is an increase in NOx emission in the mixture CO_2/O_2, while for the mixture H_2O/O_2 there is a decrease. At lower CO concentrations, there is no disturbance in NO reduction [32]. Since both CO and NOx are very unfavorable for the environment and health, it presents a great obstacle to reduce both of them at the same time. Nitrogen suboxide emission**,** N_2O, is expected to be low. According to [24], for 1000 ppm NOx inlet concentration, due to the SNCR, the amount of nitrogen suboxide formed was 51 ppm when using ammonia, while for urea it was 157 ppm. The N_2O formation is mostly influenced by temperature, the amount of reducing agent injected, as well as the NOx and CO concentration in flue gases. The formed N_2O does not have to be emitted completely, there is a possibility of its reduction to N_2. There is a possibility of combining SNCR with other measures. When stricter NOx reduction is required, a hybrid SNCR-SCR system can be applied (SCR in the duct). When ammonia as a reducing agent is used, ammonia slip from SNCR is purposely generated to feed SCR catalyst. Reduction of NOx to 90% with reduced SCR catalyst volume is possible with a hybrid system application [33].

4. Detailed chemical mechanism.

SNCR with ammonia as a agent [34] can often be found in the literature as thermal deNOx, while SNCR in combination with urea appears as NOxOUT [35]. When ammonia is used as an agent, its decomposition occurs, which generates NH_2

radicals that enter into a chemical reaction with NO, after which N_2 and H_2O are formed as products, while urea $(NH_2)_2$ is first decomposed into HNCO and NH_3. Afterward, in the case of urea, HNCO reacts with H and OH radicals, resulting in the formation of NH_2 and NCO, and only then, the radicals react with NO. Thermal decomposition of urea in real conditions does not occur instantaneously, so it is necessary to include the chemistry of this procedure in the chemical model of SNCR with urea. The selectivity of the process is determined as the ratio of reduced moles of NOx and spent moles of reducing agent. The selectivity reaches a maximum when its value equal to one, while negative values of the selectivity indicate the reverse process from reduction [36]. Since the first appearance of this technology, a large number of studies have been presented, to explain the chemistry of reduction, as well as the conditions under which it happens. Table 2 shows the selected representative mechanisms, as well as the specifics that characterize them.

The importance of numerical simulations is emphasized as a guide for system design, due to the cost of experimental tests. To be able to numerically simulate SNCR, it is necessary to select the chemical equations that will represent SNCR. Otherwise, an overly large system of equations emerges which with conservation equations requires extensive resources besides other complications that arise. The selection of representative equations for SNCR chemistry is the key to making numerical modeling possible. There are several ways to perform this procedure. One is the systematic tabulation of chemical responses from canonical problems from combustion. These are solved with incorporated detailed chemistry for various parameterized initial conditions. The second approach is to implement very simplified chemistry, i.e. a global reaction scheme. That implies limiting the reactions and species which will appear in the numerical simulation [37]. The second approach has proven to be very good for predicting process behavior. It is important to choose enough equations to simulate the SNCR reduction. In addition, not all chemical reactions contribute equally, so the global scheme, i.e. the skeletal reduction mechanism, can be distinguished from the detailed mechanism [38].

5. Numerical simulation and industrial application.

The reduction zone is characterized by a behavior very similar to plug flow behavior, preceded by a reducing agent injection zone in which conditions are different. Modeling droplets of reducing agent solution (mostly urea solution) during injection should be considered in real systems. This refers to the size and distribution of droplets. The injection is performed by spraying an agent which changes from a liquid to a gaseous phase and mixes with the flue gas, due to the temperature necessary for SNCR. So this is a multi-component problem. At temperatures higher than 673 K, the formation of a solid urea membrane around the droplet can be expected, in which water remains trapped in the initial moments of spraying [36, 43]. Also, it is necessary to pay attention to the very intense turbulent mixing in the injection zone.

NOx emission from application in plants that use biomass as fuel with and without SNCR implemented is presented [2]. Authors showed that the emission of NOx with implemented SNCR for mixed fuel in vibrating grate boilers is in the range of 0.343-0.384 kg/t, while without SNCR is almost three times higher.

Table 2. Detailed chemical models for SNCR

Author	Year	Reducing agent	Reactions	Species	Notes
Miller and Bowman [39]	1989	NH_3	234	103	Thermal, prompt, fuel-N mechanisms, NNH
Coda-Zabetta and Hupa [40]	2008	NH_3	371	60	Reaction subsets for oxidation of H_2, CO, Light hydrocarbons and CH_3OH alongside nitrogen pollutants
Javed *et al.* [41]	2008	Urea	170	30	Effect of CO and H_2 addition
Klippenstein *et al.*[42]	2011	NH_3	207	34	NNH mechanism for NO formation

CONCLUSION

The introduction of biomass, especially agricultural residues, into the energy sector represents a significant step forward in sustainable development. It is crucial to overcome accompanying problems and obstacles. Here, the SNCR is considered as a solution for one of the negative effects of biomass combustion - NOx emissions. The NOx emission contributes to further damage to the ozone layer and is harmful to human health and the entire ecosystem. This paper presents the concise view of the SNCR, from the initial theory, to the possibility of implementation in a real-scale systems. It is necessary to further expand the knowledge about this measure, especially to overcome the lack of data on the application of SNCR in the energy sector. In addition, there is a need for further research on the numerical simulation of the SNCR process, especially when urea is used as a reducing agent. Overcoming these limitations is the aim of the future research, so the optimal level of knowledge can be accomplished.

NOMENCLATURE

SCR - selective catalytic reduction;
SNCR - selective non-catalytic reduction;
NOx - nitrogen oxides ($NO + NO_2$).

REFERENCES

1. A. De Marco, C. Proietti, A. Anav, L. Ciancarella, I. D'Elia, S. Fares, M. F. Fornasier, L. Fusaro, M. Gualtieri, F. Manes, A. Marchetto, M. Mircea, E. Paoletti, A. Piersanti, M. Rogora, L. Salvati, E. Salvatori, A. Screpanti, G. Vialetto, M. Vitale, C. Leonardi, *Environment International,* **125**, 320 (2019).
2. S. Lin, H. Tian, Y. Hao, B. Wu, S. Liu, L. Luo, X. Bai, W. Liu, S. Zhao, J. Hao, Z. Guo, Y. Lv, *Science of The Total Environment,* **767**, 144 (2021).
3. K. Skalska, J. S. Miller, S. Ledakowicz, *Science of The Total Environment*, **408**, 3976 (2010).
4. G. Katsaros, P. Sommersacher, S. Retschitzegger, N. Kienzl, S. A. Tassou, D.S. Pandey, *Fuel,* **286**, 119310 (2021).
5. M. Mladenović, M. Paprika, A. Marinković, *Renewable and Sustainable Energy Reviews,* **82**, 3350 (2018).
6. I. A. Shah, X. Gou, Q. Zhang, J. Wu, E. Wang, Y. Liu, *Journal of Clean Production,* **199**, 400 (2018).
7. O. Karlström, H. Wu, P. Glarborg, *Fuel,* **235**, 1260 (2019).
8. A. A. Khan, W. de Jong, P. J. Jansens, H. Spliethoff, *Fuel Processing Technology,* **90**, 21 (2009).
9. J. Koppejan, Sj. van Loo, The Handbook of Biomass Combustion and Co-firing. Routledge, 2007.
10. A. Anca-Couce, P. Sommersacher, N. Evic, R. Mehrabian, R. Scharler, *Fuel,* **222**, 529 (2018).
11. J. Giuntoli, Delft University of Technology, Mechanical, Maritime and Materials Engineering, 2010.
12. E. Houshfar, Ø. Skreiberg, D. Todorović, A. Skreiberg, T. Løvås, A. Jovović, L. Sørum, *Fuel,* **98**, 29 (2012).
13. H. Zhan, X. Zhuang, Y. Song, G. Chang, Z. Wang, X. Yin, X. Wang, C. Wu, *Journal of Clean Production,* **236**, 117706 (2019).
14. G. Archan, R. Scharler, L. Pölzer, M. Buchmayr, P. Sommersacher, C. Hochenauer, J. Gruber, A.Anca-Couce, *Fuel,* **302**, 121073 (2021).
15. P. Glarborg, J. A. Miller, B. Ruscic, S. J. Klippenstein, *Progress in Energy and Combustion Science,* **67**, 31 (2018).
16. D. Wang, S. Hui, C. Liu, H. Zhuang, *Fuel,* **180**, 34 (2016).
17. N. Li, Y. Wang, S. Cui, D. Sun, *Fuel,* **287**, 119564 (2021).
18. E. Houshfar, Ø. Skreiberg, T. Løvås, D. Todorović, L. Sørum, *Energy & Fuels,* **25**, 4643 (2011).
19. S. Feldmeier, E. Wopienka, M. Schwarz, C. Schön, C. Pfeifer, *Energy & Fuels,* **33**, 11724 (2019).
20. S. Ozgen, S. Cernuschi, S. Caserini, *Renewable and Sustainable Energy Reviews,* **135**, 110113 (2021).
21. T. Nussbaumer, *Energy & Fuels,* **17**, 1510 (2003).
22. M. Mladenovic, D. Dakic, S. Nemoda, M. Paprika, M. Komatina, B. Repic, A. Eric, *Hemijska Industrija* **70**, 287 (2016).
23. E. Houshfar, R. A. Khalil, T. Løvås, Ø. Skreiberg, *Energy & Fuels,* **26**, 3003 (2012).
24. P.-M. Park, Y.-K. Park, J.-I. Dong, *Atmosphere (Basel)* **12**, 1175 (2021).
25. H. Chen, D. Z. Chen, S. Fan, L. Hong, D. Wang, *Chemosphere,* **161**, 2088 (2016).
26. S. Mahmoudi, J. Baeyens, J. P. K. Seville, *Biomass Bioenergy,* **34**, 1393 (2010).
27. F. Gholami, M. Tomas, Z. Gholami, M. Vakili, *Science of The Total Environment,* **714**, 136712 (2020).
28. A. A. Basfar, O. I. Fageeha, N. Kunnummal, S, Al-Ghamdi, A. G. Chmielewski, J. Licki, A. Pawelec, B. Tymiński, Z. Zimek, *Fuel,* **87**, 1446 (2008).
29. J. Shao, Y. Tao, K. K. Hansen, *Electrochemistry Communications,* **72**, 36 (2016).
30. E. Houshfar, T. Løvås, Ø. Skreiberg, *Energies (Basel),* **5**, 270 (2012).
31. M. Fu, C, Li, P. Lu, L. Qu, M. Zhang, Y. Zhou, M. Yu, Y. Fang, *Catalysis Science & Technology,* **4**, 14 (2014).
32. Y. Zhang, L. Zhao, J. Duan, S. Bi, *Separation and Purification Technology,* **234**, 116081 (2020).
33. F. Gao, X. Tang, H. Yi, S. Zhao, C. Li, J. Li, Y. Shi, X. Meng, *Catalysts,* **7**, 199 (2017).

34. M. Tayyeb Javed, N. Irfan, B. M. Gibbs, *Journal of Environmental Management,* **83**, 251 (2007).

35. H. M. A. Sharif, N. Mahmood, S. Wang, I. Hussain, Y. N. Hou, L. H. Yang, X. Zhao, B. Yang, *Chemosphere,* **273**, 129695 (2021).

36. S. Yang, X. Pan, Z. Han, D. Zhao, B. Liu, D. Zheng, Z. Yan, *Chemical Engineering Journal,* **331**, 8 (2018).

37. B. Guo, T. Luan, *Bulgarian Chemical Communications,* **48**, 166 (2016).

38. R. Gholami, C. E. Stere, A. Goguet, C. Hardacre, *Philosophical Transactions of the Royal Society A:* *Mathematical, Physical and Engineering Sciences,* **376**, 20170054 (2018).

39. J. A. Miller, C. T. Bowman, *Progress in Energy and Combustion Science,* **15**, 287 (1989).

40. E. Coda Zabetta, M. Hupa, *Combustion and Flame,* **152**, 14 (2008).

41. M. T. Javed, W. Nimmo, B. M. Gibbs, *Chemosphere,* **70**, 1059 (2008).

42. S. J. Klippenstein, L. B. Harding, P. Glarborg, J. A. Miller, *Combustion Flame,* **158**, 774 (2011).

43. L. Liang, S. Hui, S. Pan, T. Shang, C. Liu, D. Wang, *Fuel,* **120**, 38 (2014).

High sensitivity calorimetric sensor for flow measurements

G. Golan*, M. Azoulay

Ariel University, Kiryat Hamada Ariel 40700, Israel

Industrial mass flow controllers (MFC) are limited to high-sensitivity measurements. Two methods for mass fluid flow detection and measurement are presented in this work. The flow sensor consists of a temperature sensor and a reference thermistor to accurately detect laminar flows with high sensitivity. The thermistor is self-regulated maintaining a positive temperature coefficient (PTC) due to the utilization of resistive Joule heating. This, in turn, ensures constant power dissipation to the fluid. Measurement of transient fluid flow is achieved through variations in the enthalpy advection to the fluid. The relationship between the enthalpy advection and the fluid flow is found to be in agreement with the first-order model for high sensitivity response to temperatures. Finally, we have shown superior sensitivity of the measured flow in comparison with that of the available commercial MFC devices.

Keywords: Thermal response test, ground thermal properties, borehole heat exchangers

INTRODUCTION

Positive temperature coefficient (PTC) semiconductors are prepared from oxide materials such as $BaTiO_3$, through ceramic technology or films. Depending on the material composition the thermal resistance can be changed linearly or non-linearly with respect to the surface contact with a substance flow, liquid, or gas. Linear PTC thermistors are used for a wide range of temperature sensing applications and non-linear PTC thermistors are typically used for low-range temperature sensors [1, 2], anemometers [3, 4], liquid level detectors [5] and heating elements [6]. Another intrinsic characteristic of a PTC thermistor is the Joule heating effect. When a current flows in the PTC resistive thermistor it gets hot, and the generated heat results in an internal temperature increase. Due to the variable thermal resistance of PTCs and in order to maintain constant temperature at the PTC, its current varies in accordance with the thermal load of the flowing fluid. This phenomenon is called self-regulated heating. PTC thermistors are widely used as analogue thermal switches in electro-mechanical appliances and as controllers in the food, chemical, medical, and automotive industries. The main challenge in applying PTC thermistors as flow sensors lies in the non-linear dependence of their thermal resistance and in correlating their physical dimensions to the liquid or gaseous flow. The self-regulated heating phenomenon is widely used in flow level detection, anemometry and voltage and current limiters heavy duty electrical appliances.

These PTC-based self-regulated heaters provide high sensitivity at a relatively low cost and complexity, compared to the discrete solutions.

Since the signal from a thermistor depends on the fluid temperature a second PTC is positioned next to the sensor, outside the flow (liquid or gas) to measure the fluid temperature. In our study we investigated the convection of fluid mixtures in order to determine their flow rates. For this purpose, we assumed uniform concentration of each fluid at the probe surface and in the continuous phase far from the probe [7]. The aim of this work was to design a method for measuring a wide range of fluid flows based on heat advection from the PTCs to the fluid, develop a mathematical model for determining the flow rate and carry out analysis of other various methods for signal conditioning to increase measurement efficacy.

HEAT TRANSFER

Application of the first law of thermodynamics to an infinitesimal Newtonian fluid of uniform composition with constant properties, may be used to measure fluid velocity [8]:

$$P_{diss} = I_t^2 R_t = h(v)A_s(T - T_\infty) \qquad (1)$$

where:

P_{diss} - Power dissipated by Joule heating, W;

I_t – Current through the thermistor, A;

R_t – Thermistor's resistance, Ω;

$h(v)$ – Heat transfer coefficient, W/m^2K;

A_s – Surface area, m^2;

T – temperature at the solid fluid interface, K;

T_∞ – Fluid temperature far from the probe, K;

The relation suggested by King [8] for the fluid velocity is given by:

$$hA_s = a + bv^n \qquad (2)$$

---

* To whom all correspondence should be sent:
E-mail: gadygolan@gmail.com

where a and b are constants given by the dimensionless Reynolds and Prandtl numbers. These constants depend on the fluid and system properties and the power n of the fluid in Eq. (2) typically equals to 0.5 for a laminar fluid flow. PTC thermistors resistance increases with the increase of temperature and is described by an exponential relation Eq. (3). The relationship between thermal resistance and temperature in turn, yields a model of the PTC temperature, relative to the heat dissipated by Joule heating to the fluid, as shown in Eq. (5).

$$R(T) = R_0 e^{b(T-T_0)} \tag{3}$$

$$h \sim v^{0.5} \tag{4}$$

$$R(v) = R_0 e^{-\frac{b^2}{2}v^2 - T_0 + T_f} \tag{5}$$

where:
$R(v)$ - PTC resistance, Ω;
R_0 – PTC reference resistance, Ω;
b – PTC temperature coefficient;
v – Fluid velocity, m/s;
T_0 – PTC reference temperature, K.

The PTC resistance is highly dependent on variation of the fluid velocity due to the forced convection. For precise measurements of the fluid velocity, the fluid temperature is determined at a reference point of the PTC in the exponential resistance zone. Calibration of the fluid velocity/temperature relationship in the exponential resistance regime of the PTC, is the basis for all measurements. It is important to set the reference point of the thermistor in the exponential regime in order to maintain high sensitivity and set reference points at the limits of the working conditions.

Constant power configuration

In Fig. 1, the control volume of the proposed model is presented. A reference thermistor T_{s1} measures the fluid temperature while a PTC heated thermistor T_{s2} detects the thermal load of the fluid, trying to maintain a constant temperature [9]. The relation between the two signals can be observed using a Whitson balanced bridge, shown in Fig. 2, in order to digitize its open-circuit voltage. An instrumentation amplifier can be used to match the signal obtained from the bridge and the analog-to-digital converter (ADC), to increase its efficiency [10]. On one hand, the current flow through T_{s1} needs to be minimal in order to avoid temperature reading error due to the Joule heating, and on the other hand, T_{s2} draws increased currents in order to maintain a constant temperature difference between the fluid and the probe. These constraints prevent a

proper balanced bridge operation; therefore a second PTC could not be applied as T_{s1} reference temperature sensor. A second resistive negative temperature coefficient (NTC) thermistor can be applied and satisfy the above constraints. NTC temperature reading can be calculated using the well-known Steinhart-Hart equation [11].
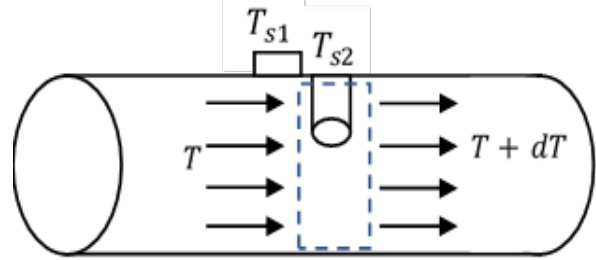
Fig. 1. Schematic structure of the flow sensor

$$\frac{T_{s1}}{T_{s2}} = \frac{R_1}{R_2} \tag{6}$$

Following Eq. (6) for a balanced bridge, the relation between the PTC and NTC for fluid temperature (T_{s1}/T_{s2}), equals the relation between R_1 and R_2, where R_1 is used to limit the NTC current and reduce self-heating errors, and R_2 can be selected with low values to enable high power dissipation in the probe. That results in a highly resistive NTC thermistor compared to the PTC.
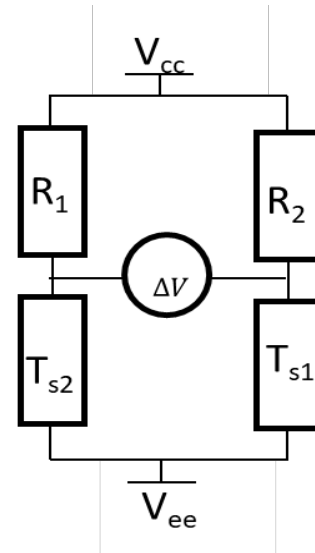
Fig. 1. Resistors bridge for accurate sensor reading

The proposed procedure is suggested for the measurements of Eq. (4) constants:

- Measurement of the PTC resistance temperature curve, and the I-V curve.
- Measurement of the PTC Curie temperature and the corresponding resistance.

- Measurement of the PTC zero velocities temperature and corresponding resistance.
- Determination of the constants according to both reference fitting points.
- Measurement of the NTC resistance with constant fluid temperature.
- Balancing the bridge using either the NTC or replacing it with a constant resistor of the value calculated above.

The main drawback of the proposed model is the lack of temperature compensation in case the fluid temperature varies, and high-power consumption.

Transient response

Another proposed approach for measuring the fluid velocity is by means of the rate of enthalpy advection over the cross-section of the PTC thermistor. As the PTC self-regulates the power dissipated to the fluid, the transient step response of the PTC to the heating signal is proportional to the thermistor and fluid mechanical properties, heat capacity, and mass transfer coefficients. Starting from the energy balance of Eq. (7), a first-order differential equation is obtained Eq. (8):

$$P_{diss} = h(v)A_s(T\text{-}T_\infty) + mc\frac{dT}{dt} \tag{7}$$

where:

m - probe mass, Kg;
c – specific heat, J/K;

$$mc\frac{dT}{dt} + hA_sT = P + hA_sT_\infty \tag{8}$$

The solution of Eq. 8 is in the exponential trend as in Eq. (9):

$$T(t) = K(1\text{-}e^{\frac{t}{\tau}}) \tag{9}$$

where:

$$\tau = \frac{mc_p}{hA_s} \tag{10}$$

$$K = \frac{P+hA_sT_\infty}{hA_s} \tag{11}$$

As obtained from Eq. (9), the time constant and the maximum temperature are both dependent on the fluid velocity, as presented in Eqs. (10, 11). It can be noted that high thermal response can be achieved by reducing the probe thermal mass, by decreasing its dimensions.

MEASUREMENT SYSTEM

In the experiment, a cylindrical stainless probe, a PTC thermistor (TDK Electronics B59010D1135B040) was taken as the enthalpy sensing element. Its diameter is 2 mm and the length exposed to fluid is about 3 mm. The stainless probe NTC (Littlefuse USP7806) was used to measure the fluid temperature. During the measurement the PTC was heated with constant voltage and thus constant power. The heat was then transferred to the flowing fluid – N_2, since the gas density is known, it is more convenient to measure the mass flow rate. As shown in Fig. 2 a Wheatstone bridge was used in the flow measurements to obtain the electrical resistance change in time and the temperature change with time. The sensors were inserted in a T shape connector as shown in Fig. 3 and thermal epoxy was used for sealing. Using a 15 VDC power supply the maximum power dissipation was measured at 300 mW.

Fig. 2. Assembly of two thermistors in T shape ¼" Swagelok connector

RESULTS AND DISCUSSION

Various flows were applied using a mass flow controller (MFC) and the system response for both constant power and transient conditions were measured. For constant power dissipation, the measurement was taken after verifying that the system had reached thermal equilibrium, resulting in a data acquisition (DAQ) system for display. The results obtained are shown in Fig. 4.
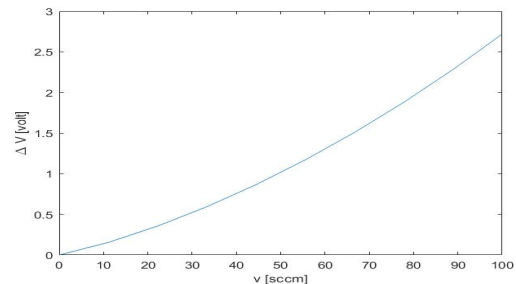
Fig. 3. Voltage difference obtained from the Wheatstone bridge in response to the variation of the fluid velocity

High sensitivity was achieved even for a low flow rate up to the highest resolution of the industrial MFC. Transient response was measured using an operational amplifier (OA) in order to indicate that the balanced bridge has crossed its reference voltage (0.69V) of the full bridge voltage. In Fig. 5. the measured temperature difference between the probe and the fluid is displayed for various flow rates. The expected behavior of the increased response time, while the fluid flow increases, may indicate a high sensitivity at the lower flow rates. When the PTC behaves exponentially poor response is obtained for higher flow rates.

Fig. 5. Thermal constant time as function of flow rate

NOMENCLATURE

A_s – Surface area, m^2;
b – PTC temperature coefficient;
c – Specific heat, J/K;
$h(v)$ – Heat transfer coefficient, W/m^2K;
I_t – Current passing through the thermistor, A;
m - Probe mass, kg;
P_{diss} - Power dissipated by joule heating, W;
R_t – Thermistor's resistance, Ω;
$R(v)$- PTC resistance, Ω;
R_0 – PTC reference resistance, Ω;
T – Temperature at the solid fluid interface, K;
T_∞- Fluid temperature far from the probe, K;
T_0 – PTC reference temperature, K;
v – Fluid velocity, m/s.

Fig. 4. Transient response of PTC for different mass flow rates

The results presented in Fig. 6 indicate the increase of thermal constant time as a function of the flow rate in the sensor.

CONCLUSIONS

Two methods were proposed for measuring the fluid velocity by a thermal flow meter. A PTC was suggested for the measurements due to the exponential response of the fluid's Curie temperature, relative to the velocity. This enables the detection of low velocities. Due to the self-regulation of the PTC, no external current source is needed to maintain the hot wire at constant temperature and thus the circuit implementation is easier in comparison with conventional resistive thermal flow sensors. As the resistive heater method suffers from high power consumption, the self-regulated PTC method is favourable due to transient response for low power working conditions. The results obtained in the experiments show high sensitivity in comparison with an industrial MFC.

REFERENCES

1. T. Dragos, G. George, D. Ilie, D. Alexandru, *Applied Mechanics and Materials,* **880**, 157 (2018).
2. N. K. Vaegae, V. L. N. Komanapalli, B. R. Annepu, *Measurements,* **85**, 54 (2016).
3. M. Y. Kang, J. Kim, H. D. Choi, *Nuclear Engineering and Technology,* **52**, 2620 (2020).
4. G. Golan, Flow velocity measurement method and apperatus, including applications therof for measuring heat flow, and wind velocity and/or direction generation. US Patent 7036367, B2, 2006.
5. M. Horn, L. Umar, H. Ruser, *Proc. of the 19th IEEE Instrumentation and Measurement Technology Conference (IEEE Cat. No. 00CH37276)* (2002).
6. X. Jin, J.-Q. Li, C.-N. Zhang, P.-E. Wu, *Energy Procedia,* **104**, 62 (2016).
7. S. B. Paramane, A. Sharma, *International Journal of Heat and Mass Transfer,* **52**, 3205 (2009).
8. L. V. King, *Philos. Trans. R. Soc. A*, 214 (1914).
9. E.-S. Zanoun, F. Durst, J.-M. Shi, *International Journal of Heat and Mass Transfer,* **52**, 3693 (2009).
10. S. Pan, K. A. A. Makinwa, *Journal of Solid-State Circuits,* **56**, 501 (2021).
11. S. J. Steinhart, S. R. Hart, *Deep Sea Research and Oceanographic Abstracts,* **15**, 497 (1968).

Optimization of the design and operating characteristics of a boiler based on three-dimensional mathematical modeling

B. Ongar[1,2*], Hr. Beloev[3*], A. Georgiev[4], I. Iliev[5], A. Kijo-Kleczkowska[6]

[1] *Satbayev University, Department of Power Engineering, 22a Satpaev str., Almaty, Kazakhstan, 050013*

[2] *Logistics and Transport Academy, Department of Power Engineering, 97 Shevchenko str., Almaty, Republic of Kazakhstan, 050012*

[3]*University of Ruse, Department of Agricultural Machinery, 8 Studentska Str., 7017 Ruse, Bulgaria*

[4]*University of Telecommunications and Post, Department of General Engineering, 1 Akad. Stefan Mladenov Str., 1700 Sofia, Bulgaria*

[5] *University of Ruse, Department of Heat, Hydraulics, and Environmental Engineering, 8 Studentska Str., 7017 Ruse, Bulgaria*

[6]*Czestochowa University of Technology, Department of Thermal Machinery, Dąbrowskiego 69, 42-201 Częstochowa, Poland*

Currently, ANSYS Fluent software is widely used as an alternative engineering tool for describing the physical processes that occur in boiler furnaces and burners. Studies of the fuel preparation and combustion characteristics in the KVTK-100-150-4 boiler using the ANSYS Fluent program were performed. The characteristics of the combustion process in the combustion chamber were calculated. The analysis of methods for reducing the pollutant formation showed the rationality of using staged combustion to reduce NO_x emissions. The performance of the proposed modeling method in MATLAB was demonstrated by using Type I and Type II error functions, followed by higher statistical performance such as error variance and correlation analysis. A comparative analysis was carried out to substantiate the superiority of the proposed modeling technique.

INTRODUCTION

The structure of the carbon soot preparation and burner devices, equipment of the KVTK-100-150-4 boiler of Ekibastuz CHP were studied. Energy characteristics of the Ekibastuz coal were determined and analysis of methods of reduction and generation of harmful substances was performed.

The causes of mechanical deterioration and nitrogen oxides formation in the CHP were determined. The main areas of reducing and preventing the occurrence of nitrogen oxide emissions were considered. Various thermal profiles of thermal preparation of burning fuel using chemical reactors, air-flow and process furnaces, pyrolysis of coal dust with reduction of nitrogen oxides in combustible products, as well as surface and contact heat exchangers were compared.

Preconditions for clean concepts of habitat protection of boiler units to be redesigned and updated were created for the focal phenomena and thermal circuits. Proposals were made to significantly reduce emissions of nitrogen oxides in the CHP with minimal changes of burners and coal preparation systems.

A simulation of Ekibastuz coal and generator gas combustion in the KVTK-100-150-4 boiler unit was performed. The temperature and velocity contours were obtained inside the hearth. Concentrations of nitrogen oxide at the burners' level and at the outlet of the hearth were calculated.

The advanced boiler plant modeling strategy includes experiment-based modeling [1, 2] and first-principle-based modeling. Experimental modeling is utilized for control designing and reflecting the major non-linear dynamics. First-principle-based modeling shows the relationship between engineering principles and physics and true plant parameters, and it can control the algorithm evaluation. For better boiler efficiency, innovative methods have to be developed with advanced optimization approaches. The optimization of boiler operation parameters can be achieved by two broad methodologies, namely (a) traditional method and (b) intelligent method. In the traditional method, the design value, experimental value, historically optimum value and actual data

---

* To whom all correspondence should be sent:
E-mail: b.ongar@satbayev.university
      hbeloev@uni-ruse.bg

are used to optimize the boiler operational parameters. The method has advantages such as real-time updating at good probability, while it has disadvantages such as difficulty in handling multiparameters, high investment of work force and resource, survey and installation errors, equipment aging issues, and limitations in mining strategies. The intelligent method is based on data mining technology and intelligent technologies.

Based on the detailed analysis of the problem carried out in the interim report, the most effective method of preventing the formation of nitrogen oxides is the organization of fuel combustion in a three-stage manner, as shown in Fig. 1.

During the fuel combustion, sulfur dioxide SO_2 is formed, due to the burning of FeS_2 pyrite. Oxide accelerates the synthesis between SO_2 and O_2 [3]:

$$2NO + O_2 \leftrightarrow 2NO_2$$

$$NO_2 + SO_2 \leftrightarrow NO + SO_3$$
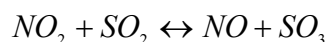
Chemically active NO_2 accelerates the transformation of sulfuric oxide into more toxic sulfuric anhydride.

Fig.1. Three-staged burning

Under the influence of hydrogen and carbon oxides, sulfur dioxide turns into a corrosive active hydrocarbon. Carcinogenic active benz(a)pyrene is formed due to reduction of local coefficient of excess air and increase of C_2H_2 and C_2H_4 concentration. Ultimately, prevention of the

formation of nitrogen oxides requires comprehensive consideration of its secondary results (with the consequences of incomplete combustion): formation of carcinogenic substances and environmentally dangerous CO, increase in consumption of chemical and mechanical incomplete combustion, high-temperature hydrogen sulfide oxidation.

Therefore, it is worth saying that the reduction of harmful gas emissions from the combustion of organic fuel is necessary for habitat protection and resource saving (which leads to the reduction of vegetation and oxygen, which in turn affects the human life due to the harmful radioactive waste of nuclear power plants and lack of energy (which is independently equivalent to global causal conditions such as heat deaths) is an urgent task.

Based on sufficiently effective measures to prevent nitrogen oxides formation, nitrogen is converted into inert matter by pyrolysis until air is introduced, this phenomenon being explained by the preliminary re-compression of active nitrogen in matter.

The thermal profiles of thermal preparation of fuel with a conventional hearth and chemical reactor, with a nitrogen oxide recovery pyrolyzer, with surface heating of dust in the designed boiler, as well as in Fig. 1 with recuperative heating of coal dust in an upgraded boiler were compared and implemented. The coefficient of flue gas recirculation with a temperature of 1200°C up to 900°C used for pyrolysis and drying of coal dust has values from 0.149 to 0.35. According to Bleyer [3], the degree of gasification of bibastuz coal was about 50%. Then, the amount of nitrogen oxides released into the environment decreases by 3.3 times and is about 0.210 g/m^3 for KVTK-100-150-4 boiler. See Fig. 1 for the layout of a nitrous oxide recovery pyrolyzer, i.e., the performance is expected to be even better for the layout of the dual avoidance of nitrous oxides. Heat exchange of two-phase flows is performed according to [5]. The characteristics of the injector for aeration of coal dust of the KVTK-100-150-4 boiler with fuel and gas consumption of 8.194 kg/s and 62 kg/s, operating flow 400°C and mixture heat 900°C were calculated [4].

A numerical study of the process of formation of nitrogen oxides during the combustion of Ekibastuz coal by the dust method was performed using the method of mathematical modeling at various values of oxygen concentration, temperature and process time, taking into account the kinematics of the formation of fuel oxides of nitrogen. Drying and transportation take place with air, and hot flue gases are taken from flue gas channels, at a temperature of
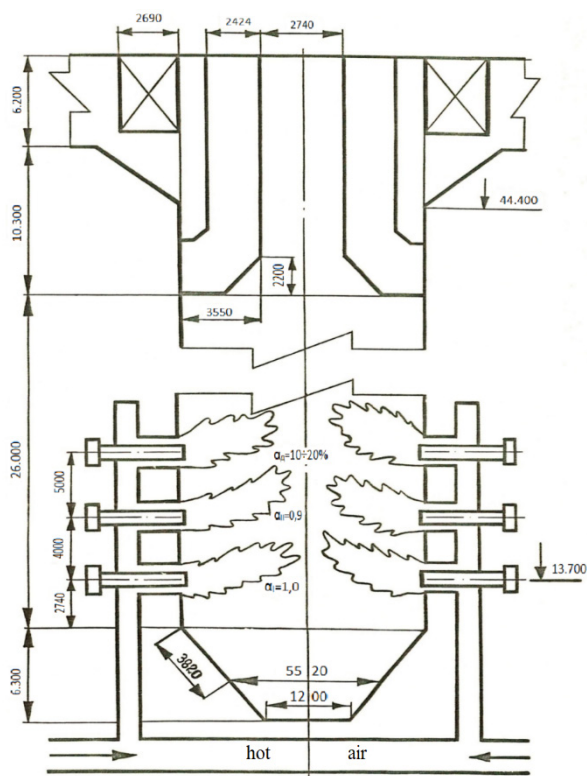
about 400°C. In such an uncomplicated reconfiguration of the air duct and the replacement of the air-drying agent with a gaseous one, the burners remain structurally unchanged. Their stable operation is ensured by maintaining the gas flow rate in the primary channel (not less than 25 m/s [6]) and air flow rates in the secondary channel (not less than 15 m/s) at the same level. The level of emissions of nitrogen oxides and the phenomenon of combustion are regulated by changing the primary and secondary airflow and the consumption of additional primary air.

General characteristics of the KVTK-100-150 boiler

The KV-TK-100-150 boiler has a capacity of 116 MW and operates on crushed stone and brown coal. Boilers of the KBTK-100-150 type are designed to operate in the main mode (when installed for industrial heating), in some cases in peak mode (when installed to cover the peak thermal load at the TPP (Thermal Power Plant). The boiler is single-hull and has a U-shape.

The main technical indicators of the boiler are presented in Table 1. The boiler diagram is shown in Fig. 1.

Table 1. Technical indicators of hot water boiler KVTK-100-150

Technical indicators of hot water boiler	Numerical value
Thermal power, MW	116.3
Water inlet temperature (main/peak mode), ˚C	70/100
Hot water outlet temperature , ˚C	150
Hot water pressure, MPa	2.35
Water flow rate (main/peak mode), t/h	1 236/2 460
Fuel consumption (calculated), t/h	17.8
Width along the column axis, mm	12 300
Depth along the column axis, mm;	18 000
Height of the boiler, mm	*29 680*

Description of the physical model

It is believed that all combustion processes, in particular aerodynamics, chemical reaction, combustion, heat and mass exchange and the formation of nitrogen oxides are interrelated in the ANSYS fluent complex. The gas introduced in the burners has the following components: carbon dioxide CO_2, molecular nitrogen N_2, water vapor H_2O and oxygen O_2. the description of the turbulence characteristics of the flow is carried out by the modified standard turbulence model k [4].

In this work, a model was adopted that considers the main stages of combustion, namely: evaporation of moisture, heating, ignition, combustion of volatile substances and combustion of coke residues. in the

combustion chamber, the coal particle undergoes heat treatment due to thermal radiation (Fig. 1). The calculation was made for ash content of Ekisbastuz coal [5]. The composition of the fuel and lower heating value (LHV) is shown in Table 2.

Table 2. Elemental composition and lower heating value of Ekibastuz coal [4]

Rank	Units	Value
Carbon, C^r	%	44.8
Hydrogen, H^r	%	3.0
Nitrogen, N^r	%	0.8
Oxygen, O^r	%	7.3
Sulfur, S^r	%	0.70
Water, W^r	%	6.5
Ash, A^r	%	36.9
LHV	kJ/kg	16 493

Mathematical modeling of the transformation of the furnace and burner processes of the KVTK-100-150 boiler

At the initial stage of the research, a lattice model of the combustion chamber of the KVTK-100-150 boiler unit was built (Fig. 2), fuel and air inlets were fixed. The mesh model consists of 250,000 cells.
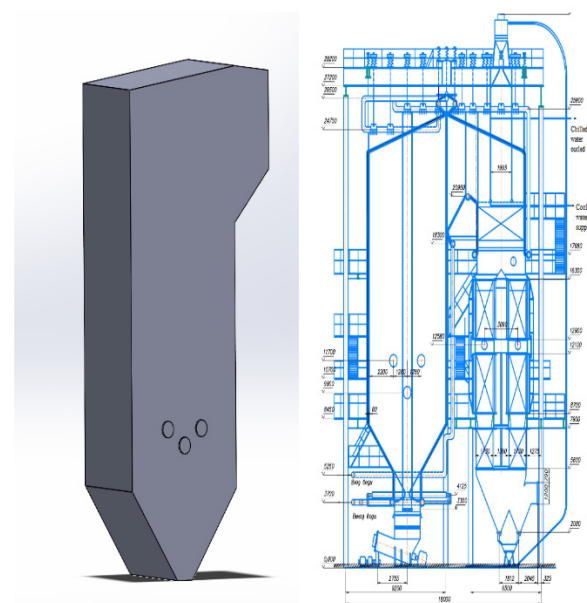
Fig. 2. Calculation model of KVTK-100-150 steam boiler

Boundary conditions were the speed of fuel in burners, temperature values as shown in Table 2 and elemental mass of fuel. The initial temperature of air was 750 K, and the initial temperature of fuel was 450 K. The reason for this is that fuel and air are preheated in boiler units, so their temperatures are assumed to be higher than atmospheric. Six burners in the form of an inverted triangle are located on the surface wall of the KVTK-100-150 boiler shown in Fig. 2.

155

Three-dimensional calculations performed in the ANSYS Fluent program allow obtaining the rate of formation of nitrogen oxides, temperature and concentration distribution in the horizontal and vertical sections of the combustion chamber, as well as tracking the trajectory of coal particles.

Fig. 3 shows the velocity vectors at the burner level of the boiler. The following can be drawn from the pictures - the direction of the velocity vectors is vertical, the main reason for this is that the direction of the gases is toward the outlet of the combustion chamber; there are no vectors showing the vortex.
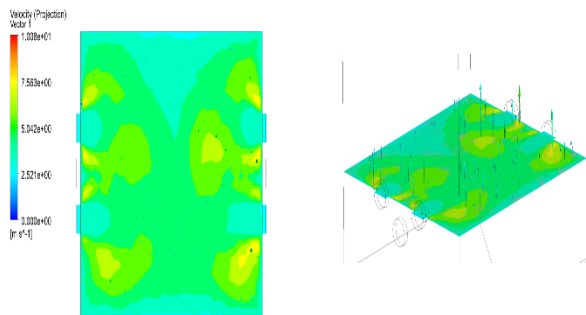
Fig. 3. Velocity vector field at the burner level of the KVTK-100-150 boiler unit (m/s)

Fig.4 shows the distribution of temperatures at the burner level of the boiler. As can be seen in the picture, the high-temperature zone is located at the inlet of the burners, that is, in the part where the coal particles meet the air and burn.

Fig. 5 shows the movement trajectory of solid fuel particles in the KVTK-100-150 boiler. It can be seen from the general trajectories that when the fuel particles leave the two fuel groups, they meet in the geometric center of the furnace and move further vertically.

Turbulence modelling was performed by using the k-ε turbulence model. Input parameters include air and fuel parameters, as well as domain parameters. The initialization procedure checks the correctness of the model and prepares it for calculation (2000 iterations are given in the calculation).

Fig. 6 shows temperature contours (fields) in the vertical section of the boiler. As can be seen in the picture, the main part of the gases burns in the upper part of the boiler furnace. Therefore, their temperature reaches 1770 K.

The main reason for this is the intensity of mixing of gases with air, that is, in a diffusion flame, the combustion of gases is limited only by the order of mixing.

The obtained results show that the selected mathematical model implemented in the ANSYS Fluent program, as a whole, shows similar values with the thermal calculations of

the boiler plant and shows the current picture of the combustion processes. Analysis of the results of mathematical modeling of the KVTK-100-150 boiler unit confirms the presence of slag-increasing zones of the combustion chamber in the pinch zone of the boiler.

High values of the temperature of flue gases leaving the combustion chamber of the KVTK-100-150 steam boiler intensify the process of formation of primary and secondary ash and slag deposits on the heating surfaces. At the same time, the concentration of nitrogen oxides is 443.8 mg/m^3, almost 1.5 times higher than standard indicators. Thus, the conducted calculations confirm the existence of problems in boiler plants.
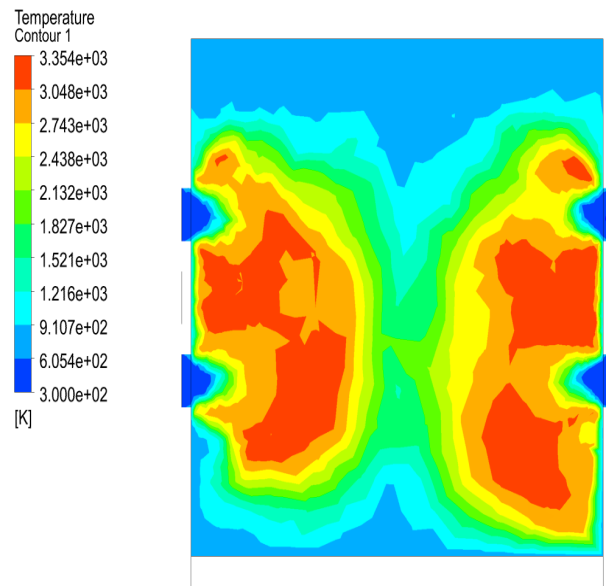
Fig. 4. Field of temperatures (K) at the burner level of the KVTK-100-150 boiler
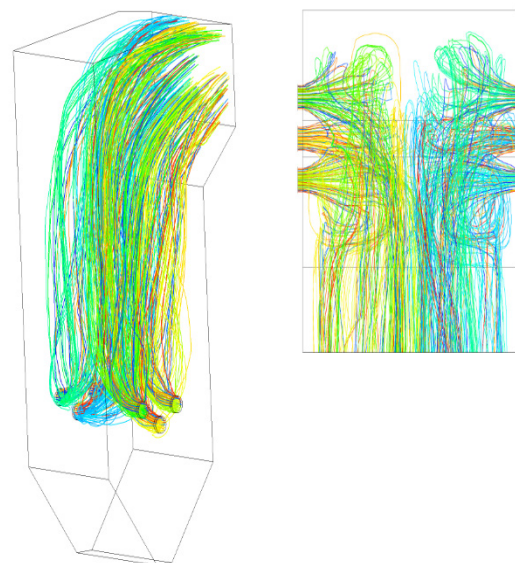
Fig. 5. Distribution of coal particles in the furnace of the KVTK-100-150 boiler unit
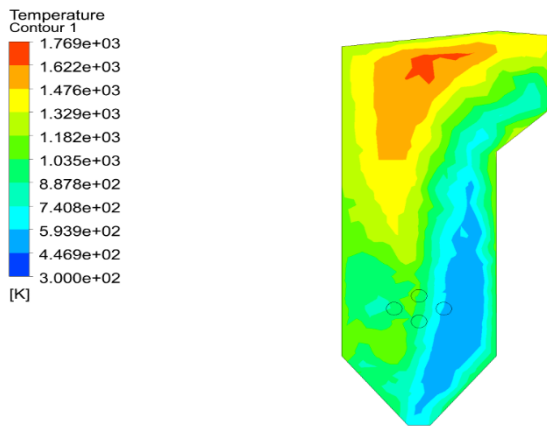
Fig. 6. Temperature field (K) in the vertical section of the KVTK-100-150 boiler

Since the conversion of the KWTK-100-150 boiler from solid fuel to generator gas is envisaged, it is necessary to calculate the generator gas. Generator gas can be obtained from a variety of solid fuels. This paper is based on the literature on the composition of generator gas, which is produced from the Ekibastuz coal. The composition and LHV of the generator gas is shown in Table 3. In this simulation, a three-dimensional simulation of the gas generator was performed.

Table 3. Elemental composition and lower heating value of generator gas

Rank	Units	Value
Hydrogen, H_2	%	30.0
Nitrogen, N_2	%	50.4
Oxygen, O_2	%	7.3
Sulphur, S	%	0.70
Carbon monoxide, CO	%	30.0
Carbon dioxide, CO_2	%	5.0
Methane, CH_4	%	2.0
Hydrogen sulphide, H_2S	%	0.2
Total	%	125.6
LHV	kJ/kg	6 400

To ignite the gas generator, it is necessary to provide its composition in the ANSYS Fluent program. The composition of the gas generator will depend on the composition of coal. The elementary composition and LHV of generator gas is shown in Table 3. Since the LHV of the generator gas is 5 times less than that of coal, its maximum temperature will be much lower. Therefore, in addition to these calculations, work was carried out to determine the maximum temperatures. The results are shown in Fig. 7. It was found that the adiabatic combustion temperature of Ekibastuz coal and generator gas has the following values: 3000 K and 1800 K, respectively [7-12].
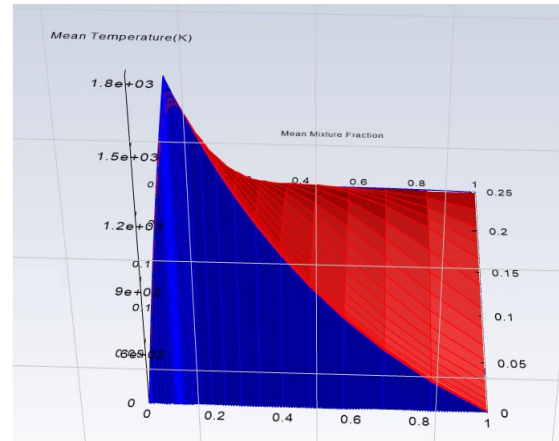
a) Maximum temperature level for generator gas
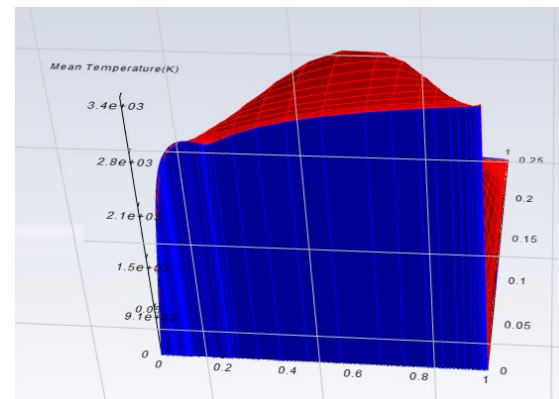
b) Maximum temperature level for Ekibastuz coal

Fig. 7. Comparison of the maximum temperature level for the Ekibastuz coal and generator gas

Analysis of the results obtained by modeling

Nitrogen concentrations and temperature levels at the furnace outlet are shown graphically in Fig. 8. From the results obtained, we can conclude that the generation of nitrogen oxide occurs through two mechanisms: first, the high temperature inside the furnace – that is, thermal NO_x formation mechanism, and the second is the fuel NO_x formation mechanism. In the case of Ekibastuz coal combustion, whose LHV (LHV=16 493 kJ/kg) is 2.57 times higher than that of generator gas (LHV=6 400 kJ/kg) it is obvious that the mass fraction of NOx is much higher. At the same time, the values given in Table 1 clearly indicate that the fuel contains nitrogen (N^r= 0.8%), which of course affects the formation of fuel nitric oxide.

In order to study the distribution of temperature levels, temperature and velocity contours at heights of 9.2, 11.2, 13.2, 15.2 meters of the boiler furnace, were considered. The results are shown in Fig. 8.
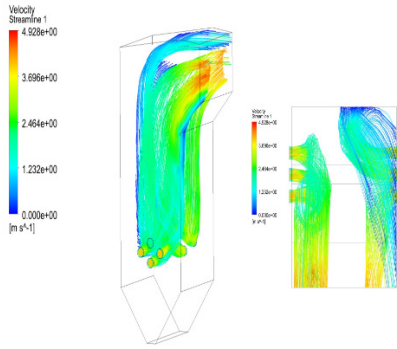
Fig. 8. Temperature and speed values in the vertical section of the KWTK-100-150 boiler

a)

b)

c)

d)
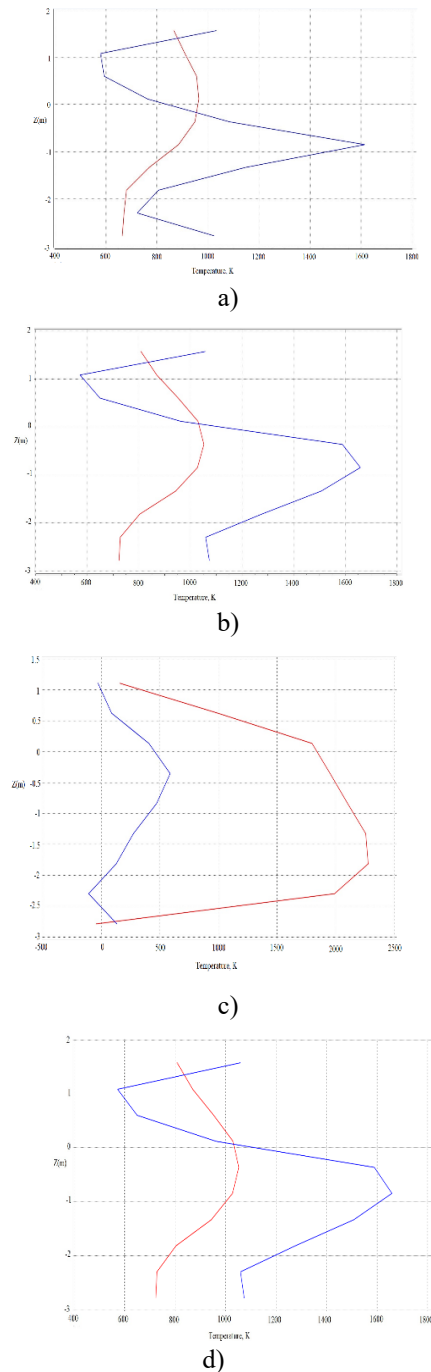
Fig. 9. Temperature distribution by altitude, K (red line for generator gas; blue line for coal)

Fig. 9 shows the temperature distribution for Ekibastuz coal and generator gas in the vertical section of the KWTK-100-150 boiler. As it can be seen, the temperature of coal has a low value at altitudes between 9.2 and 11.2. The main reason for this is the length of the combustion time of a coal particle relative to the gas. However, in the upper radiation part of the boiler, it is clear that the temperature of coal is much higher when compared with generator gas. It is clear that when switching the boiler to gas, it is necessary to take into account the location of the screen pipes and the modes of water circulation.

It is obvious that a decrease in the concentration of the oxidizing agent leads to a decrease in temperature in the combustion zone, due to the lack of oxygen to initiate the combustion reaction. At minimum values of oxygen concentration in the combustion zone, the highest temperatures were between 1500K and 1600K.

The decrease in the concentration of oxygen leads to insufficient combustion of fuel, which, in turn, reduces the temperature in the combustion zone. It was noted that an increase in the oxygen concentration from 16% to 18% leads to a sharp increase in the concentration of nitrogen oxides.

The same character has the dependence of the concentration of soot on the oxygen concentration in combustion chamber. A sharp increase in the concentration of soot at 18% indicates that there is no sufficiently complete burning out of pulverized coal.

"Rebening-process" - three-stage combustion. Suppression of nitrogen oxides to molecular nitrogen.

However, as was previously shown in the works, this method to reduce emissions of nitrogen oxides has a fundamental disadvantage. The resulting reduction zones in the form of carbon monoxide and hydrogen contribute to significant corrosion of metals, as well as the occurrence of carcinogenic substances.

The paper [8] notes the feasibility of less costly measures to suppress the formation of nitrogen oxides through the appropriate organization of combustion processes.

The above results clearly demonstrate the fairly high efficiency of the proposed method of initial gasification of Ekibastuz coal in the mechanism for suppressing the formation of nitrogen oxides without increasing the yield of products of incomplete combustion of fuel.

The essence of the proposed phase shift method with the reduction of nitrogen oxide to molecular nitrogen, due to the carbon of the fuel and the phase

shift of the air supply, consists in preliminary gasification of coal particles with a temporary delay in supplying air to the gasification products before entering the combustion zone in the flue volume itself [8].

This technique allows, in our opinion, to ensure the reduction of nitrogen oxide emissions to the level of modern requirements without increased emission of carcinogenic substances, high-temperature corrosion of metals, chemical and mechanical underburning, and with the lowest capital and operating costs.

CONCLUSIONS

The performed mathematical modeling of combustion in a boiler allowed us to draw the following conclusions:

- the NOx emission is significantly affected by the temperature of the fuel and air. The study of combustion and mixing processes made possible to determine the optimal combination of fuel consumption with an oxidizer in terms of the formation of nitrogen oxides;

- the process of flame stabilization and the formation of harmful substances is largely affected by the excess air, which is determined in inverse proportion to the concentration (consumption) of fuel;

- the results obtained by the mathematical modeling of combustion processes make it possible to explain the processes under study in more detail than when conducting experiments alone, since real combustion processes are rather transient.

The results of the simulation of burning Ekibastuz coal and generator gas in the KWTK-100-150 boiler led to the following conclusions:

- owing to the high heating value of Ekibastuz coal, at the same fuel consumption, the temperature level inside the furnace is much higher.

- the temperature distribution directly depends on the combustion rate of the coal particle. That is, the temperature of coal particles above the level of the burners is much higher.

The error deviation has been evaluated, and it is noted that the error is decreased with definite parameters. The obtained results prove the efficiency of the proposed modeling technique. The proposed boiler plant model has advantages such as flexibility, accuracy, and the ability without the knowledge of experts. However, the proposed model has not been experimented for its accuracy under external disturbance. In such cases, the precision shall be uncertain, which should be compensated for in the future.

REFERENCES

1. K. J. Astrom, R. D. Bell, *Automatica,* **36** 363 (2000).
2. I. Kocaarslan, E. Cam, *Energy Convers. Manage.,* **48,** 787 (2007).
3. B. Ongar. Dissertation for the degree of Doctor of Philosophy (PhD), Almaty, AUPET, 2018.
4. M. Kljajic, D. Gvozdenac, S. Vukmirovic, *Energy,* **45**, 304 (2012).
5. J. Yang, V. I. Golovitchev, P. R. Lurbe, J. J. L. Sánchez, *International Journal of Chemical Engineering,* **6**, 10 (2012).
6. X. Liu, R. C. Bansal, *Appl. Energy,* **130**, 658 2014).
7. A. Mergalimova, B. Ongar, A. Georgiev, K. Kalieva, R. Abitaeva, P. Bissenbayev, *Energy*, **224**, 120088 (2021).
8. B. Ongar, I. Iliev, G. Smagulova, A. Mergalimova. *Journal of Engineering Science and Technology Review*, 171 (2020).
9. L.-Ch. Bao, B.-G. Sun, Q.-H. Luo, Y. L. Gao, X. Wang, F. Liu, Ch. Li, *International Journal of Hydrogen Energy,* **45**(39), 20491 (2020).
10 X. J. Liu, X. B. Kong, G. L. Hou, J. H. Wang, *Energy Convers. Manage.* **65,** 518 (2013), 10.1016/j.enconman.2012.07.028.
11. Zh. Kolev, S. Kadirova, *IOP Conf. Series: Materials Science and Engineering,* **595,** 012006, NACOT 2019, 1-8, (SJR rank: 0.192 /2018, https://www.scimagojr.com/journalsearch.php?q=19 700200831&tip=sid), ISSN 1757-899X (online) (2019).
12. Z. Kolev, S. Kadirova. *E3S Web of Conferences,* **180**, 01009 (2020), TE-RE-RD 2020, 1-10, (SJR rank: 0.174, https://doi.org/10.1051/e3sconf/ 202018001009), E-ISSN 2267-1242 (2019).

Investigation of the properties of Ti/TiN/TiCN gradient hard coating deposited on Stavax ESR steel

M. D. Simov[1*], V. S. Rupetsov[1], Ch. O. Pashinski[2,3*]

[1]Plovdiv University "Paisii Hilendarski", Faculty of Physics and Technology, Department of Mechanical Engineering and Transport, 28 Dicho Petrov Str., 4700 Smolyan, Bulgaria

[2]Central Laboratory of Applied Physics, Bulgarian Academy of Sciences, 61 St. Petersburg Blvd., 4000 Plovdiv, Bulgaria

[3]Technical University of Sofia, Plovdiv Branch, Faculty of Mechanical Engineering, Department of Mechanics, 25 Tsanko Diustabanov Str, 4000 Plovdiv, Bulgaria

The application of hard wear-resistant coatings in the industry constantly increases because of the growing requirements for the quality of tools and products. The field of the injection molds is not an exception, there are important problems, e.g., reducing the wear of the forming elements, as well as achieving easier ejection of the finished article. These challenges could be resolved by applying an appropriate coating. In this work, a gradient Ti/TiN/TiCN hard coating was deposited on Stavax ESR steel by physical vapor deposition (PVD) method. Some important properties for its practical application were studied emphasizing on its wear resistance. For investigating the latter, a methodology based on the ball-on-flat test was used, as the wear volume was geometrically calculated on the basis of the measured track width. Data from the conducted studies of the wear resistance as a function of the normal load of the tribosystem are presented. Analysis of the results was performed and conclusions were made with regard to the practical application of the coating.

Keywords: PVD, hard coatings, mold making, wear resistance

INTRODUCTION

The worldwide use of plastic products constantly increases. Polymer products have successfully replaced a lot of the metal ones used in the past. The physico-mechanical properties of the used polymeric materials are constantly improved, and one of the promising tendencies in this direction is the addition of fillers and fibers [1]. The need for growing quantities of plastic products determines additional requirements on the durability of used injection molds [1, 2].

The working surfaces of the tools for the production of polymer parts by the casting under pressure method are subjected to a complex load. On the one hand, the mold is put to cyclic temperature fluctuations during its filling with melt and its subsequently cooling. At the same time, the working surfaces are subjected to both pressure and bending loads because of the filling of the mold. During this part of the process, the glass and mineral fillers in the polymer have a strong abrasive effect. On the other hand, tool opening and article ejecting result in strong friction upon the working surfaces.

The adhesion of the polymer and its shrinkage after cooling further increase this friction and lead to great exertions required to eject the finished article from the injection mold.

In order to increase the life span of the tools for production of polymer parts, it is necessary to undertake activities which simultaneously increase the wear resistance of the upper layer of the working surfaces and reduce the adhesion of the polymer to them. Also, the mold has to possess passable toughness and temperature resistance. The good machinability of its material has a positive economic effect as well.

Based on the mentioned above, it is appropriate to use PVD hard coatings which, in combination with a suitable material for manufacturing the tool, lead to increased wear resistance [1, 3-8]. The coatings with main layer of TiCN are well accepted in the industry. Under certain deposition conditions, they could combine the useful properties of TiC and TiN, which would make them a good choice to achieve the above goal [3, 9-11]. PVD is an economical, flexible and environmentally friendly process which is increasingly used in the industry.

---

* To whom all correspondence should be sent:
E-mail: miro_comp@abv.bg, pashinski@yahoo.com

The modern coating systems allow controlled gradient deposition which finely influence the composition and structure, and thus, the mechanical properties of the coatings. The aim of this work is to create a TiCN-based coating for mold making usage. It has to possess high wear resistance and its other properties have to be acceptable for practical application.

EXPERIMENTAL

Samples of material used for injection molds were prepared and a PVD coating was deposited on them. Then, their tribomechanical properties, which are more important from a practical point of view, were studied, with an emphasis on the wear resistance.

Preparation of the samples

The test samples were made of stainless tool steel which is widely used for the production of active elements for injection molding – Stavax ESR (AISI 420 modified) [1, 12].

The chemical composition of these samples (specified in the certificate of the steel manufacturer) is given in Table 1.

Table 1. Chemical composition of Stavax ESR samples in wt%

C	Si	Mn	Cr	V	P	S
0.40	0.91	0.45	13.4	0.28	0.021	0.0004

Each of the specimens was cuboid-shaped having dimensions 30 × 10 × 10 mm (length × breadth × height), as is shown in Fig. 1.
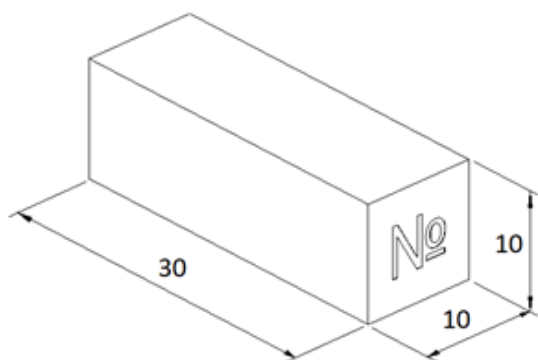
Fig. 1. Sample's appearance

Three groups of samples were prepared, which are listed in Table 2. The choice of the number of samples in each group was based on a preliminary estimation of the amount of upcoming experiments with them.

The heat treatment of the samples was performed in a chamber furnace SNOL-M ("Elprom" –

Balchik). The technological process is depicted in Fig. 2.

Table 2. Groups of the studied samples

Groups	A (1-3)	B (4-8)	C (9-12)
Treatment	unhardened ground	hardened ground	hardened polished
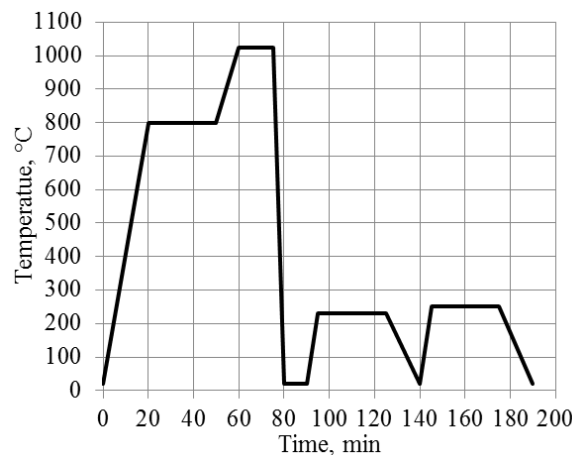
Fig. 2. Graph of the quenching and tempering process

The Ti/TiN/TiCN coating was deposited by cathodic (vacuum) arc deposition (CAD, VAD) in a coating unit π80+ (manufactured by PLATIT, Switzerland) using lateral rotating cathodes (LARC®) technology. Prior to the loading in the working chamber, the samples were mechanically cleaned, then treated in an ultrasonic bath using alkaline solvent Deconex HT 1170, rinsing in DI water and drying in a furnace at 130 °C.

The process started at initial pressure of 1.0×10^{-4} mbar in the chamber. Primarily, the heating was done in an environment of Ar (a flow rate of 6 sccm) up to 430 °C for 60 min. To improve the coating adhesion to the substrate, ion etching in a glow discharge of argon ions (Ar+) at bias voltage of -750 V and bombardment with titanium ions (Ti+) at bias voltage of -1000 V were used. The coating was applied by electric arc evaporation of Ti using a rotating cylindrical cathode in ambience of N_2 and C_2H_2. Initially, an adhesion structure was built which consists of the following layers: Ti, TiN and TiCN with a gradient composition change. Then the base layer with composition $TiC_{0.2}N_{0.8}$ was applied under the following more important parameters of the operating mode: temperature of 380 °C, working pressure of 1.2×10^{-2} mbar, cathode current of 170 A, bias voltage of -40 V. After the deposition, the vacuum chamber was isolated from the pumps and gas flows. When the temperature dropped to 350 °C, for a faster cooling N_2 was let at a flow rate of 200 sccm for 5 min. After the temperature fell to 250 °C, the chamber was opened and unloaded.

161

Test procedures

The bulk hardness of the samples was measured using a durometer TK-2M (ZIP).

The coating thickness was determined by a calo tester (a special construction of the Central Laboratory of Applied Physics, BAS) using a 30-mm ball of bearing steel.

The nanohardness and modulus of elasticity were investigated by a compact platform CPX (MHT/NHT) (CSM Instruments). A Berkovich-type diamond indenter was applied. The data processing was performed using the Oliver-Pharr method (by the software embedded in the equipment). Four load values were used: 10, 20, 50 and 100 mN, with 3 measurements performed with each of them, thereafter the corresponding results were averaged.

A micro scratch tester (MST) module which is a part of the last-mentioned equipment, was used to study the adhesion. A Rockwell diamond indenter with 200 μm top rounding was applied at a sliding distance of 3 mm. A friction coefficient value was also obtained during this test.

The roughness of the samples was measured using a mobile surface measuring instrument Handysurf E-30A (ZEISS).

Methodology for experimental study of the wear resistance

The wear resistance of the samples was assessed employing a stand created at the Faculty of Physics and Technology, PU "Paisii Hilendarski". Its construction is described in detail in [13].

The experimental studies were performed by a ball-on-flat friction method with horizontal orientation of the tested surface. The counter-part was an alumina ceramic (Al₂O₃) ball with a diameter of 3.0 mm fixed in a holder. The sample acted a reciprocating motion with length of 11 mm. The stand worked at a temperature of 20 °C, without lubricant. Loads of 1, 2, 3, 4 and 5 N were applied to the counter-part. The width of the tracks was surveyed using a non-contact PC-based measurement system TESA VISIO-300 (Brown & Sharpe TESA) at 100× magnification (resolution of 0.001 mm). Its average value was calculated by the equation:

$$b_{av} = \frac{1}{n} \sum_{i=1}^{n} b_i \qquad (1)$$

where b_{av} – average width of the track (mm), n – number of selected sections along the track (-), b_i – measured width in each of these sections (mm). On each of the tracks, five evenly longitudinally distributed sections were selected (n=5).

With a calculated average width of the track, the volume of the latter was evaluated. It is assumed that it consists of segment of a sphere (both ends of the trace if concatenated) and segment of a cylinder (main element of the trace – between the ends). The used methodology is described in [13].

The wear intensity was assessed by the equation [4, 13]:

$$I_w = \frac{V}{F \cdot L} \qquad (2)$$

where I_w – wear rate (mm³/Nm), V - wear volume, i.e., volume of the amount of the removed material (of the track) (mm³), F – normal load (N), L - sliding distance which is the distance traveled by the sample relative to the fixed counter-part (m).

RESULTS AND DISCUSSION

Initially, some of the mechanical parameters related to wear resistance were studied.

The hardness of the unhardened samples was 191 HB, while of the hardened ones - 53 HRC.

The measured thickness of the copper-red colored coating was *ca.* 2.00 μm. The calotte section looked clear, with no signs of destruction, suggesting low internal stress in the coating.

The determination of nanohardness was performed using indenter loads of 10, 20, 50 and 100 mN. The obtained curves are presented in Fig. 3.
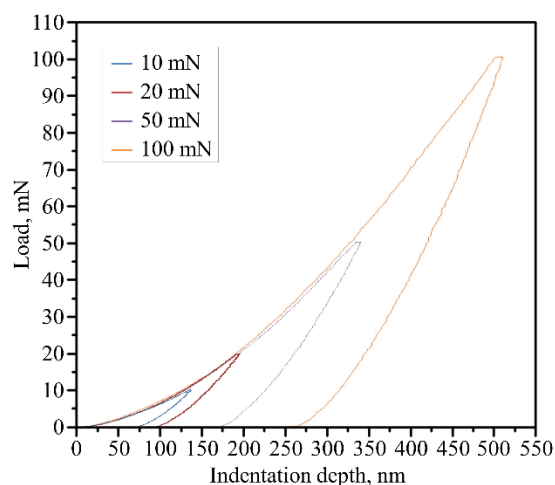
Fig. 3. Load-displacement curves at different loads

It can be seen that the curves have a very good coincidence at different loads (which are also applied at different positions on the sample). This proves that the coating possesses a good uniformity. Moreover, these curves are quite smooth which proves that no cracks appear during the indentation [14].

At a load of 20 mN, an indentation depth of average 193 nm was reached, while a nanohardness of average 35 GPa was measured. At higher loads, the indentation depth exceeded 10% of the coating thickness and the value obtained was already somewhat one integral hardness of the substrate-coating system. At lower loads, smaller nanohardness values were obtained, probably due to indentation size effects (ISEs). Therefore, it could be assumed that the nanohardness of the coating is 35 GPa which is an excellent value for similar coatings [3, 9-11]. It is in accordance with the measured Young's modulus of average 434.0 GPa. Loading and unloading curves enclosed a wide area which suggests that the coating is relatively tough [3].

No adhesion or cohesion disturbances were observed during the scratch test until the maximum stylus load of 30 N was reached. The measured coefficient of friction has a constant value of *ca.* 0.15. In Fig. 4 the end of the trace is displayed, where penetration depth of *ca.* 7.1 μm is marked.
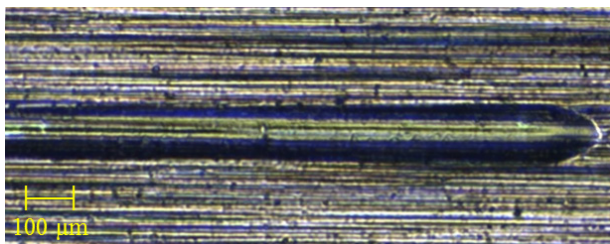
Fig. 4. End of the trace

The sample roughness is pointed out in Table 3. Obviously, it has a higher value after deposition of the coating which is clearly noticeable in the polished samples. Such an increase in the roughness is typical when the initial roughness Ra < 0.4÷0.5 μm [15].

It is known that metal ions tend to accumulate on the surface peaks in the beginning of the coating formation, which phenomenon enhances the roughness. Meanwhile, the intense Ar+ and Ti+ etching disrupts the surface's peaks, which results in roughness reduction. However, these two opposing mechanisms are not highly significant on very smooth surfaces (such as those used), as the peaks are smaller and lower.

Table 3. Data about the test samples

Group of the sample	Roughness of bare sample, Ra (μm)	Roughness with coating, Ra (μm)
A1	0.29	0.30
A2	0.24	0.24
A3	0.25	0.30
B4	0.18	0.22
B5	0.19	0.20
B6	0.18	0.20
B7	0.19	0.20
B8	0.17	0.18
C9	0.04	0.10
C10	0.03	0.10
C11	0.03	0.10
C12	0.04	0.10

The main influence upon the roughness increase have the droplets which are thermally evaporated from the cathode during the VAD process [5]. Despite the modern equipment used, the droplets have a permanent presence in the coating.

The main goal of this work is to investigate the wear resistance which is particularly important in the operation of injection molds.

The experimental studies about the influence of the normal load on the wear intensity of the presented Ti/TiN/TiCN coating were performed at the following constant parameters of the tribosystem: average sliding speed of 10 mm/s; sliding distance of 50 m.

The summarized data about the values of the volume of wear tracks as a function of the normal load $V = f(F)$ are given in Table 4.

Table 4. Wear volume at different loads of the counter-part

Load (N)	Sample group A (×10⁶, mm³)	Sample group B (×10⁶, mm³)	Sample group C (×10⁶, mm³)
1	814.044	596.299	214.064
2	1095.596	805.161	215.896
3	1334.027	1042.121	269.406
4	1397.017	1377.916	286.809
5	1583.903	1468.136	377.097

Based on these data, the diagram in Fig. 5 was built. As expected, the increase in normal load leads to higher values of wear volume for all groups of samples. Unhardened ground samples display the most intensive wear.

The reported data on the values of wear rate as a function of the normal load $I_w = f(F)$ are presented in Table 5.
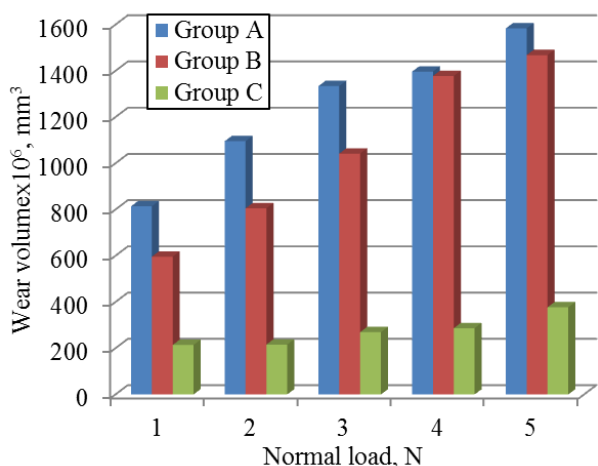
Fig. 5. Wear volume *V* as a function of normal load *F*

Table 5. Wear rate at different loads of the counter-part

Load (N)	Sample group A (×10^6, mm³/Nm)	Sample group B (×10^6, mm³/Nm)	Sample group C (×10^6, mm³/Nm)
1	16.281	11.926	4.281
2	10.956	8.052	2.159
3	8.894	6.947	1.796
4	6.985	6.889	1.434
5	6.675	5.874	1.508

In Fig. 6. a graphical representation of the above data is shown.
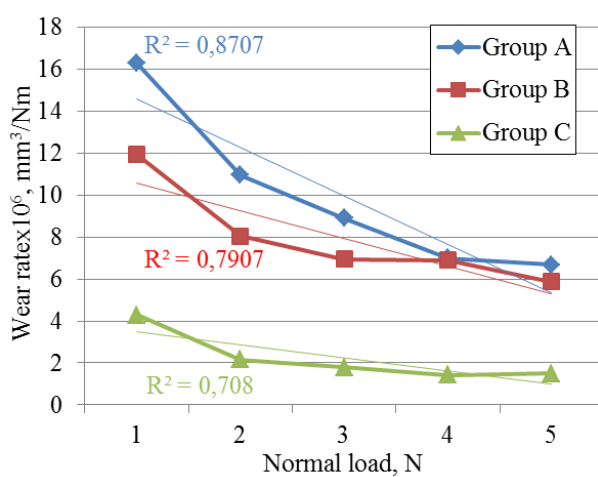
Fig. 6. Wear rate I_w as a function of normal load *F*

It can be seen that the value of the coefficient of determination R^2 is greater than 0.7 which gives a reason to believe that the dependence $I_w = f(F)$ is close to linear, at least in the range of applied normal loads. One can see that for hardened polished samples, the slope of the line is the smallest and the value of the wear rate is almost constant.

CONCLUSIONS

There is a slight increase in the roughness after coating deposition, which is more noticeable in the polished samples. This is probably due to the presence of droplets (non-ionized metal particles) which are specific for the process [15]. However, the coefficient of friction is not high. In addition, it could be assumed that soon after the injection mold activation, some of the droplets will fall away from the coating. If it is necessary, simple methods could be used to remove them before the tool be exploited [16].

To determine the wear, the volume is used as a criterion. The volume of the track increases with load increasing, this is quite expected. The wear rate decreases with load increasing. Such a coating, deposited on Stavax ESR steel, is suitable for elements which are subject to high loads. The attenuation of the wear rate practically takes place according to a linear law.

The roughness of the samples significantly influences the wear intensity of the coating. The coating deposited on a hardened and polished sample has the lowest wear volume compared to these on hardened ground and unhardened ground specimens (Fig. 5). It is advisable to polish the surfaces where it is possible before coating deposition.

The obtained values of wear rate are low, they are close to the lower limit of the results shown in similar studies [3, 9], which further determines the coating as suitable for application on injection molds.

REFERENCES

1. B. Peeters, O. Malek, S. Castagne, B. Lauwers, *Procedia CIRP*, **95**, 909 (2020).
2. E. Velev. *Proc. of TECHSYS 2018, 7th Int. Sc. Conf. on Engineering, Technologies and Systems, Plovdiv*, II-223-6 (2018) (in Bulgarian).
3. H. Shafyei, R. Ashiri, *Ceram. Int.*, **45** (12), 14821 (2019).
4. S. Dishliev, G. Mishev, *Proc. of the 7th Int. Conf. on Tribology (BALKANTRIB'11), Thessaloniki*, 31 (2011).
5. L. Kolaklieva, R. Kakanakov, D. Kovacheva, V. Chitanov, T. Cholakova, C. Bahchedjiev, S. Kolchev, *Coatings*, **11** (11), 1311 (2021), https://doi.org/10.3390/coatings11111311.
6. V. M. Beresnev, A. I. Fedorenko, V. I. Gritsenko, D. L. Perlov. *Fizich. Inzhener. Poverkhn. (Phys. Surf. Eng.)*, **1** (2), 180 (2003) (in Russian).
7. S. Veprek, M. J. G. Veprek-Heijman, *Surf. Coat. Technol.*, **202** (21) 5063 (2008).
8. R. Minchev. *Sci. Works Univ. Food Technol.*, **63** (2), 307 (2016).
9. Y. H. Cheng, T. Browne, B. Heckerman, E. I. Meletis, *Surf. Coat. Technol.*, **205** (16), 4024 (2011).

10. L. Karlsson, L. Hultman, M. P. Johansson, J.-E. Sundgren, H. Ljungcrantz, *Surf. Coat. Technol.*, **126** (1), 1 (2000).
11. D. Xiao, *J. Mater. Eng. Perform.*, **18** (9), 1226 (2009).
12. Uddeholm Stavax® ESR. *Saved from URL: https://www.uddeholm.com/files/PB_Uddeholm_stavax_esr_english.pdf*, edn. 11, 05.2013.
13. V. Rupetsov, Increasing in the wear resistance of parts and tools of the production equipment, Smolyan, Bulgaria, ZEA-Print, 2018, p. 61 (in Bulgarian).
14. C. Mendoza, Z. Gonzalez, E. Gordo, B. Ferrari, Y. Castro, *J. Eur. Ceram. Soc.*, **38** (2), 495 (2018).
15. Zh. Mrochek, A. Vershina, S. Ivashchenko, I. Ivanov, I. Frolov, S. Latushkina, Vacuum-Plasma Coatings, Minsk, Belarus, Tekhnoprint, 2004, p. 77 (in Russian).
16. T. Cselle, A. Lümkemann, M. Jilek, *Journal of HP Tooling*, **2**, 42 (2019).

Study of combustion processes in the combustion chambers of power facilities

A. S. Askarova[1,2], S. A. Bolegenova[1,2], A. G. Georgiev[3], V. Yu. Maximov[1], S. A. Bolegenova[2], M. T. Beketayeva[1,2*], A. M. Mukhtarova[2]

[1]ETP SRI of Al-Farabi Kazakh National University, Al-Farabi Av., 71, 050040 Almaty, Kazakhstan

[2]Al-Farabi Kazakh National University, Department of Thermal Physics and Technical Physics, Al-Farabi Av., 71, 050040 Almaty, Kazakhstan

[3]University of Telecommunications and Post, Department of General Engineering, 1 Akad. Stefan Mladenov Str., 1700 Sofia, Bulgaria

Simulation of the aerodynamic structure of the flow with a reasonable choice of the turbulence model makes it possible to obtain adequate results with sufficient accuracy for practice. In the proposed article, when studying the processes of heat and mass transfer, we focused our attention on the chosen turbulence model and used the results of the aerodynamic structure to explain the flow of mass flows of nitrogen oxides throughout the space of the combustion chamber. As a result of 3D computational calculations, the distributions of turbulence parameters (k and ε), velocity field (total velocity vector and its components) and nitrogen oxides in the volume of the combustion chamber and at its outlet were obtained. These results will make it possible to effectively control the processes of fuel combustion in real power plants and solve urgent problems of thermal power engineering and ecology.

Keywords: combustion chambers, solid fuel, 3D modeling, flow aerodynamics, nitrogen oxides, turbulence model

INTRODUCTION

All scenarios for the development of energy in the world must meet environmental goals, which in turn provides for a rapid reduction in the use of coal. This approach significantly complicates the development of coal energy in the world in the coming decades. However, the 2021 International Energy Agency (IEA) Coal Report notes that coal consumption could show even higher rates in subsequent years. Global demand for coal will rise to a record 8 billion tons and remain at that level until 2024. This is due to the recovery from the COVID pandemic, which turned out to be very energy-intensive. Gas, wind and sun are not enough to meet the frenzied demand for electricity and there are few technologies that could help replace fossil fuels in the coming years. The main growth in coal consumption came from China, India and the United States. In Europe, the problem was exacerbated by the weather (in recent months it was calm and cool there), the shortage of natural gas and the protracted repairs at nuclear power plants in France. Thus, the world again began to burn coal, despite the protests of environmentalists [1].

According to the WEO, there are two aspects to phasing out coal in the energy sector: 1) stopping the construction of new power plants and 2) managing the reduction of emissions from existing assets. Advanced economies are seeing a faster phase-out of coal in the energy and industrial sectors.

Demand will collectively decline by about 40% by 2030. This is due to climate policy and the rapid growth of renewable energy. Ensuring reductions in emissions from the existing fleet of coal-fired power plants is a major challenge for public policy. Given the dependence of a number of countries and regions on coal, the closure or conversion of coal mines and power plants can have serious economic and social consequences. Therefore, the use of coal, on the contrary, is expanding in many emerging market and developing countries [2]. In Kazakhstan, 95% of the mined coal is produced by enterprises of the Karaganda and Ekibastuz coal basins. Thus, the main energy fuel is coal from the Ekibastuz and Karaganda deposits. If we compare the quality of Kazakh coals with the requirements of the world market, then our coals turn out to be far from competitive. The main disadvantages of thermal coals include high costs for the transportation of coal, a large amount of combustion waste, high ash content and rapid wear of boiler units. The problem of depreciation of stations exists in all post-Soviet countries, in the Republic of Kazakhstan it is especially in the cities of Karaganda, Pavlodar, Kokshetau and in a number of cities in the southern regions. According to official statistics, the average wear and tear of the main equipment at thermal power plants in Kazakhstan is estimated at more than 55%. This, in turn, is one of the main reasons for the deterioration of the environmental situation in the regions of the Republic of Kazakhstan. Kazakhstan has developed a Green Energy Doctrine. According

* To whom all correspondence should be sent:
E-mail: beketayeva.m@gmail.com

to the concept of the energy industry, the structure of new energy capacities in 2035 will be as follows: 6.5 GW of renewable energy facilities, over 5 GW of gas generation, over 2 GW of hydroelectric power plants, 1.5 GW of coal generation, as well as 2.4 GW of nuclear generation. It is an important tool for reducing and replacing greenhouse gas emissions, as well as the gradual replacement of generation depending on fossil fuels [3, 4].

Currently, the methods used to reduce emissions of harmful substances (oxides of nitrogen, carbon and sulfur) from industrial facilities at the moment still do not meet environmental requirements and do not give the desired result. In this regard, it is important to comprehensively study the emerging problems and conduct detailed scientific research. This problem is solved with the help of modern information technologies using 3D modeling methods [2, 5-11].

3D *modeling technique*

In the context of tightening environmental requirements and economic feasibility, detailed studies using computer technologies are required for modeling (development) of new and modernization of existing thermal power plants in order to introduce environmentally friendly coal technologies [12-14]. With the help of three-dimensional modeling of the processes occurring inside the combustion chambers of power facilities, it is possible to study in detail the influence of design and operating parameters, as a result of which it is possible to find specific ways to improve the economic and environmental component of the operation of facilities, while significantly reducing the amount of experimental research.

Works using CFD methods are widely used in studies of the combustion of various fuels in many foreign countries. In particular, German scientists in their studies [15-18] use European coals as fuel, the ash content *A* of which does not exceed 8% compared to Kazakhstani (A ~ 40%). Therefore, the CFD methods in this work have been developed and adapted for researching precisely the combustion processes of high-ash Kazakh coals.

To conduct computational experiments on 3D modeling of heat and mass transfer processes in the combustion chamber, the FLOREAN software package [19–21] was used as a basis, which is based on solving conservative equations for the gas-fuel mixture using the control volume method.

The computer software package consists of a sub-model of the balance of momentum, energy, matter components, k-ε turbulence model, SIMPLE pressure correction method, six-stream thermal radiation model. This software package has been used to calculate flows in the combustion chambers of many thermal power plants both abroad [22–27] and in Kazakhstan. This software package was adapted to the task of burning high-ash Kazakh coal in the combustion chamber of the CHPP of the Republic of Kazakhstan.

As is known, the system of conservation and transport equations does not have an analytical solution and can only be solved numerically. For a numerical solution, the entire computational domain is divided by a difference grid into discrete volumes; the continuous field of variables is replaced by discrete values at the grid nodes. The derivatives included in the differential equations are replaced by their approximate expressions in terms of the differences in the values of the functions at the grid nodes. For each cell of the computational domain, physical conservation laws and differential transfer equations are used, which are integrated over the volume of each cell. The starting point for each balance value lies in the center of each control volume, since the value of the values for the control volume is stored at the center point. The stationary control volume corresponds to the justified Euler approach for flows, and the change in the transport quantity is described in a unit volume, and the values of the transport quantity are determined at each point of the considered area separately. As it is known the control volume method is flow-oriented.

In fact, there are no universal measures to judge the convergence of computational experiments. However, for most practical computational problems, convergence criteria can be established. In the FLOREAN program, the task of convergence and accuracy of calculations and simulation of combustion processes is carried out in the A1-Flamme subprogram, which is based on the following stages of calculation: beginning of iterations; model inclusion; control of calculations using relaxation factors; convergence issues.

3D *modeling of aerodynamics and turbulence*

The mixing of air and fuel during combustion, along with the efficient transfer and distribution of heat, can affect the overall performance of the combustion system. The tasks of stable combustion of fuel and transfer of generated heat to the system are determined by the aerodynamics of the burner system and the aerodynamics of the technological system as a whole. Therefore, understanding and optimizing the aerodynamics of the system is very important for the efficient operation of the entire boiler unit.

Aerodynamic issues can be assessed using analytical, physical and computational (CFD) simulation capabilities to evaluate and optimize the combustion process in an industrial plant. The aerodynamics of the flow is usually adjusted in such a way that conditions favor combustion at a given location in the flow. This may take the form of a recirculation zone formed by swirl, contour expansion, or a combination of both. In practice, the recirculation zone holds the flame root, creating a significant reverse flow, drawing hot flame products to the nozzle without introducing foreign objects into the flame. However, this flow requires careful design of the flow conditions, flow rate, burner position and geometry.

There are many techniques for changing combustion aerodynamics in relation to the requirements for using different types of fuel, obtaining different temperatures in different conditions, and using different heat transfer modes. A change in one variable can have serious consequences for the stability of the flame and the entire combustion process. There are also various criteria that can be used to optimize the industrial combustion process. Small improvements in combustion aerodynamics or heat transfer efficiency can result in direct fuel savings or result in an overall reduction in process air pollutant emissions.

The main scientific challenge is the need for a better understanding of turbulence and its effects on the transfer of momentum, heat and mass in engineering applications, including aerodynamics, industrial flows and combustion systems. While significant advances in direct numerical modeling (DNS) of turbulence and turbulent combustion, as well as the development of large eddy simulations (LES) for engineering flows, have provided valuable insights into the physics of many turbulent flows and have led to rapid improvements in turbulence and combustion modeling in industry, nonetheless, serious turbulence modeling problems remain.

It is relevant to study the nature of turbulent flows inside the combustion chamber. Velocity fluctuations characterize turbulent flows. They contribute to the mixing of transported characteristics such as momentum, energy and concentration of the components, and also cause fluctuations in these characteristics. Since these pulsations can be small scales, but have a high frequency, their calculation directly in practical technical calculations is a very difficult task. Currently, there is not a single universal model that describes the entire spectrum of turbulent flows. In practice, semi-empirical relationships are used that describe the effect of turbulence parameters on the main characteristics. In this case, the instantaneous (exact) constitutive equations can be averaged over time, represented as an ensemble average, which leads to modified systems of equations that require less computational effort to solve. However, the modified equations contain additional unknown variables.

In this article, the standard k-ε turbulence model was used to describe turbulent flow. This model is a simple two-parameter turbulence model that solves two transport equations that define the turbulent velocity and the length scale. Turbulent energy k and dissipation ε were obtained from the equations:

$$\frac{\partial(\rho k)}{\partial t} + \frac{\partial}{\partial x_i}(\rho u_i k) = \frac{\partial}{\partial x_i}((\mu + \frac{\mu_t}{\sigma_k})\frac{\partial k}{\partial x_i}) + G_k + G_b - \rho\varepsilon \quad (1)$$

$$\frac{\partial(\rho\varepsilon)}{\partial t} + \frac{\partial}{\partial x_i}(\rho u_i \varepsilon) = \frac{\partial}{\partial x_i}|(\mu + \frac{\mu_t}{\sigma_\varepsilon})\frac{\partial\varepsilon}{\partial x_i}| + G_{1\varepsilon}\frac{\varepsilon}{k}(G_k + \quad (2)$$

$$+(1-C_\mu)G_b - C_{2\varepsilon}\rho\frac{\varepsilon^2}{k}$$

Constants k-ε of the turbulence model are: $C_{1\varepsilon}$, $C_{2\varepsilon}$, C_μ, $\sigma_к$, σ_ε which have the following values: $C_{1\varepsilon}$ = 1.44, $C_{2\varepsilon}$ = 1.92, C_μ = 0.09, σ_k = 1.0, σ_ε = 1.3.

Stability, economy and reasonable accuracy for a wide range of turbulent flows make the k-ε turbulence model the most useful in industrial applications. The constant coefficients for this model are obtained empirically and therefore it is semi-empirical. It should be noted that the simulation of flows in the presence of turbulence, which are based on the solutions of equations for turbulent characteristics (the kinetic energy of turbulence and its dissipation), makes it possible to obtain the desired accuracy of the solution, while eliminating inexpedient machine costs associated with obtaining it.

The basis of the computational experiment

As an object of study for conducting a computer experiment in this paper, we chose the combustion chamber of an actually operating Kazakhstani CHP boiler, the dimensions of which are shown in Table 1. A boiler of this brand can be operated using brown and hard coal, peat, anthracite fine and lean coal. However, due to the fact that the power facility is located closer to the local Karaganda coal deposit, low-grade Karaganda coal with an ash content of more than A ~ 35% is mainly burned here.

On the side walls of the combustion chamber, the boiler has two axial-vane vortex burners located opposite each other. Technical parameters of the combustion chamber of the boiler and data on the coal burned are presented in Tables 2 and 3.

Table 1. Main geometrical parameters

Name	Value
Combustion chamber height (*Z), m*	16.75
Combustion chamber width (*X), m*	6
Depth of combustion chamber (*Y), m*	6.6
Front and back wall area, *m²*	90.675
Right side wall area, *m²*	92.4
Left side wall area, *m²*	110.55
Ceiling wall area, *m²*	27.72
Bottom wall area, *m²*	7.26
Cross-sectional area of the air mixture channel in the burner, *m²*	0.12
Cross-sectional area of the secondary air duct in the burner, *m²*	0.25

Table 2. Technical parameters

Name	Value
Number of burners on the boiler, *pcs*	4
Fuel capacity of one burner, *t/h*	3.2
Primary air flow per boiler, *Nm³/h*	31797
Secondary air flow per boiler, *Nm³/h*	46459
Hot air temperature, *°C*	290
The coefficient of excess air in the furnace	1.2
Estimated fuel consumption for the boiler, *t/h*	12.49
Cold air temperature, *°C*	30
Inlet pressure, *mbar*	$1.013 \cdot 10^3$
Hydrodynamic resistance of the air mixture channel of the burner, *mm w.st.*	67.1
Air mixture temperature, *°C*	140
Wall temperature, *°C*	430.15

Table 3. Characteristics of Karaganda coal

Name	Value
Grinding fineness (R_{90}), *%*	20
Density of coal, *kg/m³*	1350
Heat of combustion of coal, kJ/kg	$3.4162 \cdot 10^4$
Heat of combustion of coke, kJ/kg	$3.2814 \cdot 10^4$
A^c, %	35.10
V^T, %	22.00
W^P, %	10.60
C, %	79.57
H_2, %	6.63
O_2, %	9.65
S_2, %	1.92
N_2, %	2.23

To carry out computational experiments, the geometry of the investigated boiler was constructed according to its real scheme, and its finite-difference grid was compiled for numerical modeling of the processes of solid fuel combustion in the boiler combustion chamber. The finite difference grid has steps along the X, Y, Z axes: 59×32×67, which is 126 496 control volumes (Fig. 1). On Fig. 1 the location of the burners, the areas of the belt of burners, the outlet zone, and the areas of additional air supply can be seen. The choice of such a fine mesh makes it possible to provide an adequate picture of the combustion process of pulverized coal at any point in the combustion chamber.
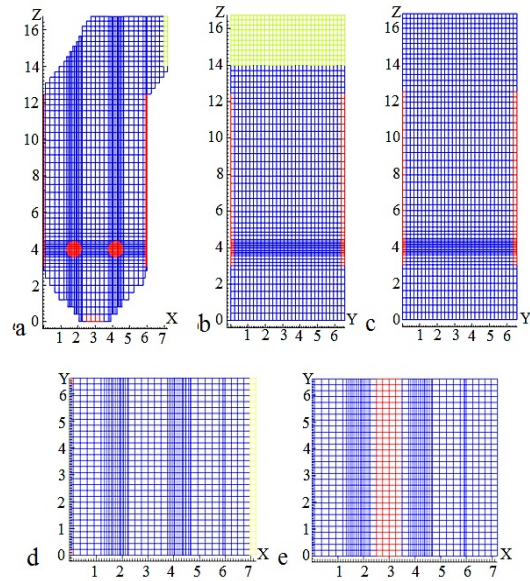
Fig. 1. Grid breakdown of the combustion chamber into control volumes (a - front side, b - right side, c - left side, d - ceiling, e - bottom)

For the mathematical description of pressure and velocity, the effective method of the SIMPLE algorithm was used in this work. Here the problems of discretization of the momentum and continuity equations are solved. SIMPLE uses corrections for the relationship between velocity and pressure to obtain mass-conserved pressure fields. Once the pressure fields are obtained, the momentum equations can then be solved to obtain preliminary velocity fields. Pressure correction and velocity corrections were calculated using the continuity equation.

In this article, when studying the processes of heat and mass transfer, we focused our attention on the chosen model of turbulence and used the results of the aerodynamic structure to explain the flow of mass flows of nitrogen oxides throughout the space of the combustion chamber.

RESULTS AND DISCUSSION

Using the modern 3D modeling method, the flow aerodynamics (full velocity vector *V*) (Fig. 2), turbulent characteristics (turbulence kinetic energy *TE*, dissipation energy *ED*) (Figs. 3, 4) and the concentration of nitrogen oxides *NO* (Fig. 5) were calculated throughout the volume of the combustion chamber and at its outlet.

Analysis of Fig. 2 shows that in the volume of the combustion chamber, as the flow of the air mixture and combustion products moves towards the exit, the speed monotonically decreases, with the exception

169

of the exit area of the boiler combustion chamber, where its surge is observed. This is due to the fact that here the geometry of the combustion chamber changes, and the flow, due to a change in its direction, becomes unsteady, forming an additional vortex, while increasing the turbulence of the flow, which leads to a change in velocity in this region of the combustion space. The full velocity vector is obtained by: $\vec{V} = \sqrt{U^2 + V^2 + W^2}$.

Fig. 2a shows the three-dimensional distribution of the full velocity vector over the depth of the combustion chamber (Y=3.19m) in its central region. In the figure, you can see how the flows collide in the center of the furnace, here the speed is highest (~ 11 m/s). Countercurrent flows blown from the burners, heading at maximum speed to the center of the furnace space, collide. And here, splitting into several vortices, they descend into the region of the cold funnel, forming vortex currents. The other part goes up to the exit from the combustion chamber. This nature of vorticity arises as a result of turbulence due to the interaction of the air mixture with the oxidizer. Above Z=8m in height, towards the exit from the furnace space, there is a gradual smoothing of the currents, the speed of which lies in the range of 4-8 m/s.

The following Fig. 2b shows the field of the full velocity vector in the area of the reversing chamber (Z=12.65m) and in the section at the exit (X=7m) from the boiler combustion chamber. As the turbulent flow moves towards the exit from the combustion chamber, the vortex nature of the flow weakens, then it intensifies in the region of the rotary section of the boiler, and an almost uniform velocity profile is observed at the exit from the chamber.

It is noticeable that in the section of the turning area of the chamber, the maximum values of velocity (~ 9 m/s) are concentrated in the central part and in the near-wall area, which can be explained to some extent by the asymmetry of the furnace geometry in this area. At the exit from the furnace space, the velocity is almost equalized, no mixing of flows is observed and its average value is ~ 4 m/s.

The presence of a swirling flow in the combustion chamber causes characteristic distributions of the main aerodynamic parameters (velocity components, turbulent and dissipative kinetic energy of turbulence) throughout the volume of the chamber. The results are shown in Figs. 3 and 4.

In the vortex region with the greatest changes in the velocity fields, that is, where the processes of physical and chemical transformations occur intensively during the combustion of pulverized coal, there are also maximum

disturbances of turbulent flows and their turbulent characteristics. This is evidenced by the maxima in the distribution of the turbulent characteristics of the process, such as the kinetic energy of turbulence *TE* and its dissipation *ED*.
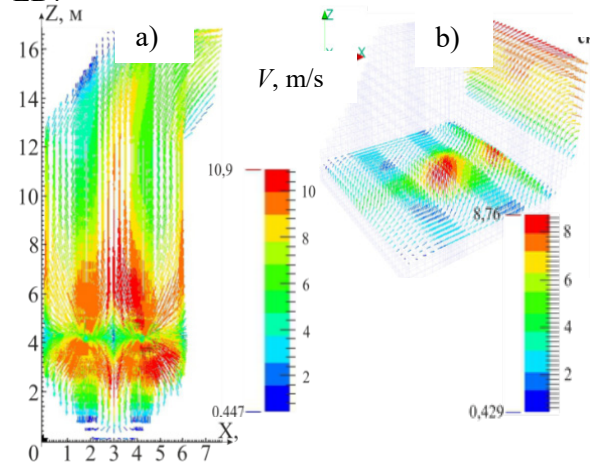
Fig. 2. Distribution of the total velocity vector V in a) longitudinal central section along the depth of the furnace (Y=3.19m); b) turning area (Z=12.65m) and at the outlet of the furnace (X=7m)

From the analysis of three-dimensional distributions of turbulent characteristics presented in Figs. 3 and 4, it can be seen that the active mixing of the fuel and oxidizer flows coming from counter burners leads to the fact that the flow in this area is highly turbulent, and the kinetic energy of turbulence and its dissipation reach maximum values here.

The kinetic energy of turbulence and the energy of dissipation reach their maximum values in the region of the belt of burners and in the lower region of the combustion chamber. These areas are a zone of collision of dusty coal flows, which is caused by unsteady perturbations of the swirling flow with sharp jumps of turbulent fluctuations. The kinetic energy of turbulence in the longitudinal central section along the depth of the furnace (Y=3.19m) has its maximum value equal to 10 m²/s² (Fig. 3a), and the dissipation energy is ~ 84 m²/s³ (Fig. 4a). Towards the exit, the average value of both parameters decreases to ~ 0.8 (Figs. 3b, 4b).

Next, let's consider the influence of the aerodynamic structure on the formation and distribution of harmful emissions such as nitrogen oxides in the combustion chamber (Fig. 5). When coal is burned, the fuel *NO* formation model takes into account coal pyrolysis, homogeneous combustion of hydrocarbons, and heterogeneous combustion of coke, considering the influence of the mineral content (in particular, ash content) of the fuel, as well as correlations at high temperatures.
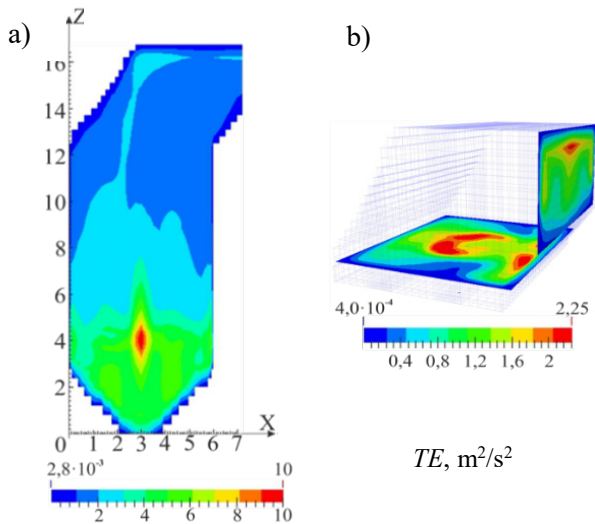
Fig. 3. Distribution of the kinetic energy of turbulence *TE* in a) longitudinal central section along the depth of the furnace (Y=3.19m); b) turning area (Z=12.65m) and at the outlet of the furnace (X=7m)
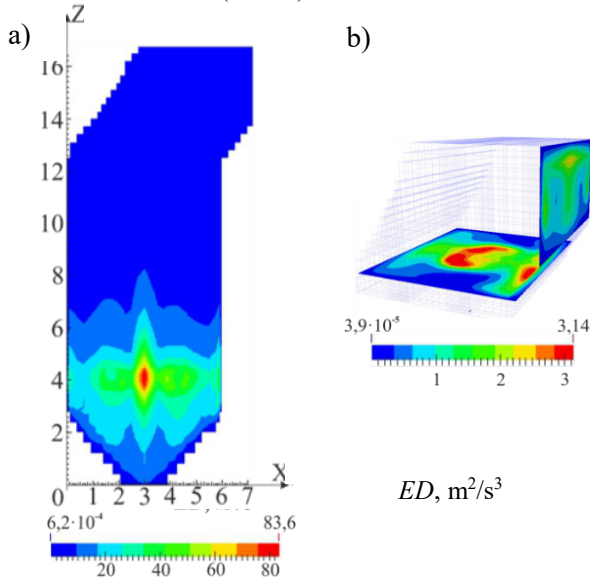
Fig. 4. Distribution of the dissipation energy *ED* in a) longitudinal central section along the depth of the furnace (Y=3.19m); b) turning area (Z=12.65m) and at the outlet of the furnace (X=7m)

Analysis of Fig. 5 of the distribution of concentrations of nitrogen oxides *NO* in the area of the location of the burner devices and at the outlet of the combustion chamber indicates the influence of flow aerodynamics on the processes of formation of concentration fields of nitrogen oxides *NO*. Intensive mixing of fuel and oxidizer, created by turbulent flows of air mixture injected from the burners, provides favorable conditions in this zone for the formation of nitrogen oxides *NO*. Thus, the concentrations of nitric oxide *NO* reach their maximum values of 5206.2 mg/Nm^3 (Fig. 5a).
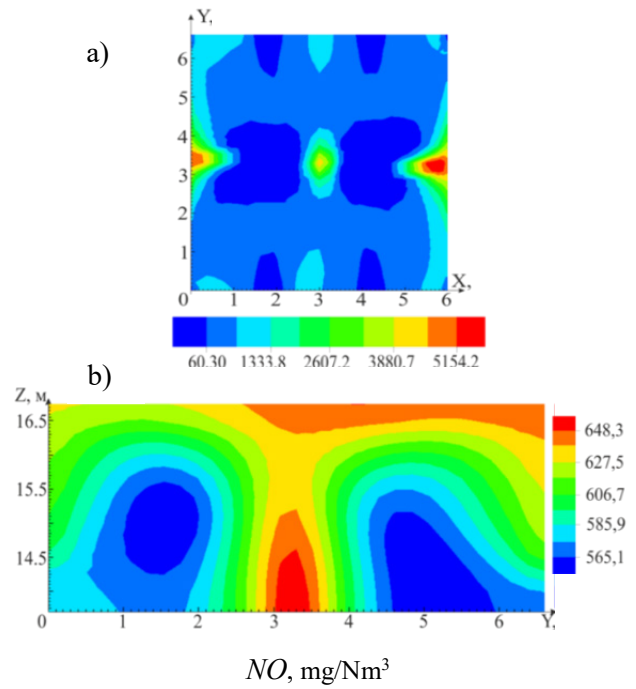
Fig. 5. Distribution of the concentration of nitrogen oxides *NO* in a) zone of the furnace burner belt (Z=3.98m); b) at the exit from the furnace (X=7.14m)

As we move towards the exit from the furnace, the chemical reactions of nitrogen oxidation decay, which is explained by afterburning and the described behavior of the aerodynamics of turbulent flows. This leads to a decrease in *NO* concentrations in the upper regions of the furnace space. The maximum concentration of nitric oxide *NO* at the outlet of the furnace (X=7.14 m) is 649.2 mg/Nm^3 (Fig. 5b). The average value of the concentration of nitric oxide *NO* at the outlet of the furnace is 613.1 mg/Nm^3, which corresponds to the MPC (640 mg/Nm^3) for coal-fired CHPPs of the Republic of Kazakhstan.

The aerodynamic characteristics obtained during the computational experiment reflect the real technological process observed in the combustion chambers. These results indicate that in the central region of the combustion chamber there is a sharp change in aerodynamic characteristics (velocity, kinetic energy of turbulent pulsations and dissipation energy) associated with the formation of a vortex flow, which weakens as the pulverized coal flow and combustion products move to the exit.

The conducted studies testify to the complexity of heat and mass transfer processes occurring during the combustion of pulverized coal fuel in the combustion chambers of industrial boiler plants. An analysis of the results obtained shows that such a detailed study of the aerodynamic pattern that takes place in the combustion chamber of the boilers of operating TPPs is possible only by numerical

simulation methods and by conducting computational experiments.

CONCLUSIONS

The presence of a volumetric vortex flow in the central region of the combustion chamber has a positive effect on the combustion process of pulverized coal fuel (heat exchange and mass transfer), since, due to the turbulent nature of the flow, intensive mixing of the fuel components with the oxidizer occurs here, which means that more complete burnout of coal dust is ensured.

The justified choice of the turbulence model made it possible to obtain with sufficient accuracy the aerodynamics of the flow and the distribution of nitrogen oxides over the entire space of the combustion chamber. The results obtained will make it possible to effectively control the processes of fuel combustion in real power plants and solve urgent problems of thermal power engineering and ecology.

REFERENCES

1. EAD, https://eadaily.com/ru/news/2021/12/17/ ugol-prikazal-zelenoy-energetike-podozhdat-mechty-i-realnost-razoshlis.
2. World Energy Outlook, www.iea.org/weo.
3. StanRadar, https://stanradar.com/news/full/ 49339-energetika-kazahstana-na-poroge-krizisa.html.
4. KazInform, https://www.inform.kz/ru/ kazahstan-zanimaet-20-mesto-v-mire-po-vybrosam-uglekislogo-gaza_a3945128.
5. R. Leithner, Sh. Ospanova, A. Yergalyeva, *Proc. of the CSCC 2016, 20th Int. Conf.*, **76**, 06001-1–06001-5 (2016).
6. S. Bolegenova, N. Askarov, A. Nugymanova, *Energies*, **14**, 1236 (2021).
7. A. Bekmukhamet, Z. Gabitova, M. Beketayeva, *IERI Procedia,* **10**, 252 (2014).
8. M. Beketayeva, A. Askarova, V. Maximov, *High Temperature*, **56**, 738 (2018).
9. S. Bolegenova, A. Bekmukhamet, V. Maximov, *Procedia Eng.,* **42**, 1150 (2012).
10. E. Karpenko, A. Ustimenko, I. Loktionova, *Thermal Eng. J.,* **51**, 488 (2004).
11. P. Safarik, A. Nugymanova, S. Bolegenova, *Chemical Engineering Technology,* **44**, 1970 (2021).
12. Z. Zheng, W. Yang, Y. Cai, *Energy,* **190**, 116 (2020).
13. V. Maximov, V. Messerle, A. Nugymanova. *J. Physics: Conference Series,* **1261**, 12 (2019).
14. P. Safarik, M. Beketayeva, S. Bolegenova. *J. Acta Polytechnica,* **59**, 98 (2019).
15. W. Linzer H. Walter, B. Epple, R. Leithner, Simulation von Krafrwerken und wärmetechnischen Anlagen, Springer, 2009.
16. K. Görner. Technische Verbrennungssysteme — Grundlagen, Modelbildung, Simulation, Springer-Verlag, Berlin–Heidelberg, 1991.
17. A. Hoppe, S. Vockrodt, H. Müller, R. Leithner. *Proc. of the 9th Conference on Boiler Technology*, 565 (2012).
18. H. Müller, R. Leithner. *Proc. of the 2nd M.I.T. Conference on Computational Fluid and Solid Mechanics*, 172 (2003).
19. H. Müller, Numerische Berechnung drei-dimensionaler turbulenter Strömungen in Dampferzeugern mit Wärmeübergang und chemischen Reaktionen am Beispiel des SNCR–Verfahrens und der Kohleverbrennung, Fortschritt–Berichte, VDI-Verlag, 1992.
20. R. Leithner, S. Vockrodt, A. Schiller. *Proc. of the 19th German Conf. on Flames*, 1492 (1999).
21. R. Leithner, Numerical Simulation, Computational Braunschweig, 2006.
22. R. Leithner, *Trans. Soc. Mining, Metallurgy and Exploration,* **18**, 135 (2005).
23. R. Leithner,, *Int. J. of Energy Technology and Policy,* **5**, 340 (2007).
24. A. Schiller, H. Müller. *Proc. of the 6th int. Conf. on Combustion and Heat Technics*, 45 (1994).
25. H. Müller, Numerische Simulation von Feuerungen, CFD Vorlesung, TU Braunschweig, 1997.
26. A. A. Genbach, D. Yu. Bondartsev, I. K. Iliev, A. G. Georgiev, *Energy,* **199** (15), 117458 (2020). https://doi.org/10.1016/j.energy.2020. 117458.
27. M. Beketayeva, A. Georgiev, S. Bolegenova, *Energy* **258**, 124826 (2022). http://dx.doi.org/10.1016/j.energy.2022.124826.

BULGARIAN CHEMICAL COMMUNICATIONS

Instructions about Preparation of Manuscripts

General remarks: Manuscripts are submitted in English by e-mail or by mail (in duplicate). The text must be typed double-spaced, on A4 format paper using Times New Roman font size 12, normal character spacing. The manuscript should not exceed 15 pages (about 3500 words), including photographs, tables, drawings, formulae, etc. Authors are requested to use margins of 3 cm on all sides. For mail submission hard copies, made by a clearly legible duplication process, are requested. Manuscripts should be subdivided into labelled sections, e.g. **Introduction, Experimental, Results and Discussion**, *etc*.

The title page comprises headline, author's names and affiliations, abstract and key words.

Attention is drawn to the following:

a) **The title** of the manuscript should reflect concisely the purpose and findings of the work. Abbreviations, symbols, chemical formulas, refer-ences and footnotes should be avoided. If indis-pensable, abbreviations and formulas should be given in parentheses immediately after the respective full form.

b) **The author**'s first and middle name initials, and family name in full should be given, followed by the address (or addresses) of the contributing laboratory (laboratories). **The affiliation** of the author(s) should be listed in detail (no abbreviations!). The author to whom correspondence and/or inquiries should be sent should be indicated by asterisk (*).

The abstract should be self-explanatory and intelligible without any references to the text and containing not more than 250 words. It should be followed by key words (not more than six).

References should be numbered sequentially in the order, in which they are cited in the text. The numbers in the text should be enclosed in brackets [2], [5, 6], [9–12], etc., set on the text line. Refer-ences, typed with double spacing, are to be listed in numerical order on a separate sheet. All references are to be given in Latin letters. The names of the authors are given without inversion. Titles of journals must be abbreviated according to Chemical Abstracts and given in italics, the volume is typed in bold, the initial page is given and the year in parentheses. Attention is drawn to the following conventions:

a) The names of all authors of a certain publications should be given. The use of "*et al*." in the list of references is not acceptable.

b) Only the initials of the first and middle names should be given.

In the manuscripts, the reference to author(s) of cited works should be made without giving initials, e.g. "Bush and Smith [7] pioneered...". If the refer-ence carries the names of three or more authors it should be quoted as "Bush *et al*. [7]", if Bush is the first author, or as "Bush and co-workers [7]", if Bush is the senior author.

Footnotes should be reduced to a minimum. Each footnote should be typed double-spaced at the bottom of the page, on which its subject is first mentioned.

Tables are numbered with Arabic numerals on the left-hand top. Each table should be referred to in the text. Column headings should be as short as possible but they must define units unambiguously. The units are to be separated from the preceding symbols by a comma or brackets.

Note: The following format should be used when figures, equations, *etc*. are referred to the text (followed by the respective numbers): Fig., Eqns., Table, Scheme.

Schemes and figures. Each manuscript (hard copy) should contain or be accompanied by the respective illustrative material as well as by the respective figure captions in a separate file (sheet). As far as presentation of units is concerned, SI units are to be used. However, some non-SI units are also acceptable, such as °C, ml, l, etc.

The author(s) name(s), the title of the manuscript, the number of drawings, photographs, diagrams, etc., should be written in black pencil on the back of the illustrative material (hard copies) in accordance with the list enclosed. Avoid using more than 6 (12 for reviews, respectively) figures in the manuscript. Since most of the illustrative materials are to be presented as 8-cm wide pictures, attention should be paid that all axis titles, numerals, legend(s) and texts are legible.

The authors are asked to submit **the final text** (after the manuscript has been accepted for publication) in electronic form either by e-mail or mail on a 3.5'' diskette (CD) using a PC Word-processor. The main text, list of references, tables and figure captions should be saved in separate files (as *.rtf or *.doc) with clearly identifiable file names. It is essential that the name and version of the word-processing program and the format of the text files is clearly indicated. It is recommended that the pictures are presented in *.tif, *.jpg, *.cdr or *.bmp format, the equations are written using "Equation Editor" and chemical reaction schemes are written using ISIS Draw or ChemDraw programme.

The authors are required to submit the final text with a list of three individuals and their e-mail addresses that can be considered by the Editors as potential reviewers. Please, note that the reviewers should be outside the authors' own institution or organization. The Editorial Board of the journal is not obliged to accept these proposals.

EXAMPLES FOR PRESENTATION OF REFERENCES

REFERENCES

1. D. S. Newsome, *Catal. Rev.–Sci. Eng.*, **21**, 275 (1980).
2. C.-H. Lin, C.-Y. Hsu, *J. Chem. Soc. Chem. Commun.*, 1479 (1992).
3. R. G. Parr, W. Yang, Density Functional Theory of Atoms and Molecules, Oxford Univ. Press, New York, 1989.
4. V. Ponec, G. C. Bond, Catalysis by Metals and Alloys (Stud. Surf. Sci. Catal., vol. 95), Elsevier, Amsterdam, 1995.
5. G. Kadinov, S. Todorova, A. Palazov, in: New Frontiers in Catalysis (Proc. 10th Int. Congr. Catal., Budapest, 1992), L. Guczi, F. Solymosi, P. Tetenyi (eds.), Akademiai Kiado, Budapest, 1993, Part C, p. 2817.
6. G. L. C. Maire, F. Garin, in: Catalysis. Science and Technology, J. R. Anderson, M. Boudart (eds), vol. 6, Springer-Verlag, Berlin, 1984, p. 161.
7. D. Pocknell, *GB Patent* 2 207 355 (1949).
8. G. Angelov, PhD Thesis, UCTM, Sofia, 2001.
9. JCPDS International Center for Diffraction Data, Power Diffraction File, Swarthmore, PA, 1991.
10. CA **127**, 184 762q (1998).
11. P. Hou, H. Wise, *J. Catal.*, in press.
12. M. Sinev, private communication.
13. http://www.chemweb.com/alchem/articles/1051611477211.html.

Texts with references which do not match these requirements will not be considered for publication!!!

CONTENTS